Riassunto

La fisica dei sistemi a forte correlazione elettronica, quali gli isolanti di Mott (MI) e di Charge Transfer (CTI), rappresenta tutt'oggi uno dei problemi di frontiera della fisica della materia condensata. Tra questi sistemi i cuprati (composti a base di ossido di rame) suscitano ampio interesse nell'ambito della comunità scientifica, dato che sono alla base di molti materiali superconduttivi, e tra questi i superconduttori ad alta temperatura critica. In questo contesto risulta importante il ruolo che ha, nella struttura elettronica dei composti superconduttivi e di CT, la formazione di uno stato legato, noto come singoletto di Zhang-Rice.

Questo lavoro di tesi riporta i risultati sperimentali sulle dinamiche di non-equilibrio indotte dalla foto-eccitazione del singoletto di Zhang-Rice (ZR) nel $CuGeO_3$. Particolare attenzione è rivolta all'osservazione dei processi di natura puramente elettronica, i.e. eccitazione e dinamica delle transizioni d-d, e ai meccanismi di eccitazione di vibrazioni reticolari coerenti (coherent phonons).

La tecnica sperimentale di pump-probe, con impulsi laser ultra-brevi, rappresenta uno strumento ideale per lo studio delle complesse dinamiche di non-equilibrio di sistemi foto-eccitati, potendo indagare questi processi su scale temporali di alcune centinaia di ps con risoluzione dell'ordine di qualche fs.

A questo scopo, è stato progettato e realizzato un apparato sperimentale originale per l'acquisizione di misure in trasmissione, che utilizza un impulso laser

super-continuo come probe della durata di circa 80 fs. L'uso del super-continuo, che copre un intervallo spettrale compreso fra 400 nm e 900 nm, permette l'acquisizione simultanea della variazione in trasmittività, foto-indotta dall'impulso di pompa, in una vasta regione spettrale, facilitando, inoltre, l'identificazione di differenti processi di rilassamento dello stato eccitato, evidenziandone la dipendenza spettrale, e soprattutto rendendo possibile la misura nel dominio temporale di eventuali fononi coerenti, spesso osservabili solo in corrispondenza di particolari regioni spettrali.

I principali risultati emersi dalle misure effettuate riguardano l'analisi delle dinamiche di rilassamento del sistema e l'osservazione di modulazioni periodiche della trasmittività, indotte dall'eccitazione di fononi coerenti.

A seguito della foto-eccitazione del singoletto di Zhang-Rice (ZR), il sistema si rilassa secondo un processo modellizzato come un decadimento multi-esponenziale. L'analisi del fenomeno ha portato all'individuazione di almeno sei dinamiche distinte, di cui la più rapida è attribuibile alla diseccitazione del singoletto di ZR, poiché ha un tempo caratteristico ($\tau < 15$ fs) comparabile con la vita media di tale eccitone nel germanato di rame ($\tau \approx 13$ fs) [1,2]. Purtroppo una comprensione dettagliata delle strutture spettrali osservate e delle correlazioni fra le dinamiche individuate richiede simulazioni numeriche di alto livello, e pertanto non è ancora disponibile.

Il rilevamento di fononi coerenti eccitati, direttamente e non, dall'impulso di pompa è il risultato più significativo di questo lavoro. In particolare, per la prima volta, accanto ad un fonone Raman A_g eccitato direttamente dall'impulso laser attraverso il ben noto meccanismo Displacive Excitation of Coherent Phonons (DECP), è stato osservato un modo coerente infra-rosso B_{1u}, la cui eccitazione è conseguenza della formazione del singoletto di ZR. Infatti, cambiando l'energia di eccitazione del sistema o la polarizzazione dell'impulso di pompa, il singoletto di ZR non è più eccitato e il fonone non viene osservato. Inoltre, presentando un tempo di attivazione pari a ≈ 1.25 ps, esso non può essere direttamente indotto dall'impulso di pompa. Purtroppo, data la risoluzione temporale del nostro apparato sperimentale ($\approx$ 80 fs), non è possibile determinare se l'eccitazione di tale fonone sia dovuta ad un accoppiamento diretto con il sistema elettronico o piuttosto all'accoppiamento con

un altro fonone coerente preesistente, di frequenza più alta. Per questo motivo è in progetto un esperimento analogo con impulsi di ≈ 10 fs.

In conclusione, con questo lavoro è stato dimostrato, per la prima volta, che fononi infrarossi coerenti possono essere eccitati in un solido a seguito della foto-eccitazione del singoletto di Zhang-Rice. Inoltre, si è dimostrato come la tecnica di pump-probe con il super-continuo permetta di misurare il tempo di letargia e di defasamento e la costante di decadimento di fononi coerenti non direttamente indotti dall'impulso di pompa.

Bibliografia:

[1] S.Pagliara, F.Parmigiani, P.Galinetto, A.Recolevschi and G.Samoggia, Phys. Rev. B **66**, 024518 (2002)

[2] D.Nardi, Thesis, università degli studi di Brescia, 2005/2006

Chapter 1

Introduction

This thesis reports about an experiment aimed to observe and measure the perturbation induced by a selective ultrashort pulse of coherent light on the electronic structure and the lattice vibrations of a charge transfer insulator such as the $CuGeO_3$. In particular, it will be shown that the photo-excitation of Zhang-Rice singlet states is followed by the creation of a coherent IR phonon with symmetry B_{1u} and a lethargy time of ≈ 1 ps. This interesting finding allows measuring the main temporal parameters of such a lattice coherent oscillations. In addition, using a super-continuum pump in the ≈ 400 nm - ≈ 900 nm spectral range, the dynamic of the electronic structure has been detected.

It is well known that very short light pulses can induce excitation processes in condensed matter that could result into phenomena observable on the macroscopic scale. In particular, the dynamical oscillations of the dielectric function, which measure can be related to the dynamics of the relaxation of the electronic structure as well to a generation of coherent phonon states, can be observed when the equilibrium conditions are perturbed by a sudden and intense coherent light pulse.

From a formal point of view the evolution of a system, excited by an intense electromagnetic field oscillating at very high frequency, can be described by averaging the statistical operator over the period of perturbation. In this frame it is also possible to describe the electron redistribution between the ground and the excited states. The electric fields and the elastic displacements appearing as a result of such a redistribution lead to vibration of the lattice, characterized by the coherent amplitudes of atomic displacements and that can be described by using the phonon density matrix formalism. These lattice vibrations are also known as coherent phonons and they can be excited in semiconductors or insulators by a shockwave generated by ultra-short laser pulses.

The direct observation of coherent phonon oscillations is possible by using, for example, stroboscopic double-pulse optical techniques. In most of the cases reported in the literature these time-resolved measurements are based on a powerful and sudden pulse of energy, used to perturb the equilibrium condition of the solid, while a weak probe pulse, properly delayed in time, is used to probe the out-of-equilibrium properties of the system under investigation. An interesting example of application is represented by the studies of the collapse of the band-gap in semiconductors [1-4] and the generation of coherent phonons in solids [5-8].

The limits of this method are both technical and conceptual. In fact, a non-selective excitation will produce a complex and multiform mechanism of interacting excited states which is difficult to control, while the use of a single frequency for the probe beam will reduce, significantly, the statistic of the measurements.

For the present experiment this technique, also known as pump-probe, has been modified and upgraded in order to perform energy selected excitations, while the detection of the electronic response to such an excitation has been achieved on a wide spectral range by using a super-continuum pulse, generated through the non-linear interaction between a ≈ 80 fs pulse, at ≈ 800 nm, produced by a conventional Titanium:Sapphire laser amplifier, and a 1 mm thick CaF_2 crystal. The amount of data acquired using the super-continuum is wide and very complex, therefore a Singular Value Decomposition (SVD) and the Decay Associated Spectra (DAS) methods have been used to analyze the dynamical optical response in the ≈ 400-900 nm spectral region.

These powerful methods evidenced some spectral regions where the optical response function was oscillating versus time. The Fast Fourier Transform of the time response function allowed the identification of the coherent phonons.

From a more fundamental point of view, the originality of the present experiment resides on the fact that, instead of looking at the band-gap collapse of a semiconductor, by photo-exciting the charges from the valence band to the conduction band, it is considered the possibility of observing the collapse of the gap in a charge-transfer insulator, i.e. the $CuGeO_3$, by using short pulses at ≈ 3.2 eV in order to photo-induced Zhang-Rice singlet excitons. The electric fields and the elastic displacements resulting from the selectively forced charge perturbation lead to a redistribution of the d-d "forbidden" transitions and to coherent lattice vibrations. This charge distribution perturbation, that insists for more than 800 ps, is of very complex analysis and offers a quite vast scenario for the theories in this field. However, among the very complex phenomena involved it merges quite clear the possibility of studying in the temporal domain phonons coupled to some specific electronic excitations.

For the first time it is demonstrated that IR-coherent phonons can be excited in a solid by photo-induced charge transfer processes associated with the formation of ZR excitons. In addition, the present experiment allows to measure the lethargy, the coherence and de-phasing times of these phonons, opening a quite new scenario on the dynamics of the lattice vibration modes in solids.

The thesis is organized as follow.

Chapter 2 reports a guideline to describe the electronic properties of strongly correlated materials, with particular attention to the case of the copper germanate. Chapter 3 is devoted to the description of the main electronic and phononic effects induced by the photo-excitation processes through the gap in a charge transfer insulator; in this chapter also the photo-excitation of the ZR-singlet is discussed. Chapter 4 presents the structure and the main properties of the $CuGeO_3$. The experimental set-up developed for the time-resolved optical measurements is described in chapter 5, with the procedures for its characterization. In chapter 6 the explanation of the Singular Value Decomposition (SVD), Decay Associated Spectra (DAS) and Fast Fourier Transform (FFT) techniques is given. The results from the

time-resolved transmittivity variation measurements are reported in chapter 7, while their discussion is left to chapter 8. In the closing chapter the main results are summarized with their interpretation.

Bibliography:

[1] L.Huang, J.P.Callan, E.N.Glezer and E.Mazur, Phys. Rev. Lett. **80,** 185 (1998)

[2] Y.Siegal, E.N.Glezer and E.Mazur, Phys. Rev. B **49,** 16403 (1994)

[3] E.N.Glezer, Y.Siegal, L.Huang and E.Mazur, Phys. Rev. B **51,** 6959 (1995)

[4] E.N.Glezer, Y.Siegal, L.Huang and E.Mazur, Phys. Rev. B **51,** 9589 (1995)

[5] G.A.Garrett, T.F.Albrecht, J.F.Whitaker and R.Merlin, Phys. Rev. Lett. **77**, 3661 (1996)

[6] A.I.Lobad and A.J.Taylor, Phys. Rev. B **64,** 180301 (2001)

[7] I.Bozovic *et al.*, Phys. Rev.B **69,** 132503 (2004)

[8] L.Perfetti *et al.*, Phys. Rev. Lett. **97,** 067402 (2006)

Chapter 2

Charge transfer processes and the Zhang-Rice singlet in cuprates

Among the strongly correlated systems the charge transfer insulators based on copper oxides represent a rather interesting case because of the formation of the Zhang-Rice singlet state. In this chapter a guideline to describe the electronic properties of strongly correlated materials is reported, with particular attention to the case of the copper germanate.

2.1 Strongly correlated systems

The electronic structure of strongly correlated systems is dominated by many body effects and it cannot be described within the independent-electron (Hartree-Fock) approximation. A possible approach to the solution of the problem was first given by N. Mott [2], who proposed a phenomenological model starting from the application of the tight-binding picture to a chain of hydrogen-like atoms. In the frame of the independent-electron approximation, a chain of hydrogen-like atoms has

one electron per unit cell and the system has a metallic character, independently from the interatomic distances, originating from electron-hopping processes between neighbouring atoms. However, looking in more details at the electron-hopping mechanism, it is clear that it involves many-body interactions and a proper description is not as simple as the independent-electron picture suggests. In particular, increasing the atom-to-atom distance the energy requested to hop the electrons will increase till a distance where an array of neutral atoms is obtained. This result is a consequence of the fact that this process is characterized by an on-site Coulomb repulsion between hopping electrons sharing the same atomic site. Since the electron hopping requires a definite energy U, known as Hubbard Coulomb repulsion energy, in narrow-band strongly electron-correlated compounds the charge fluctuations are suppressed. Therefore, depending on U and on the bandwidth, the system can be a metal or an insulator. In practice, the macroscopic properties of these materials can be controlled, to some extents, by changing the interatomic distance or by electrons/holes "doping" and a phase diagram, describing this phase transition also known as metal-insulator Mott transition, can be drown.

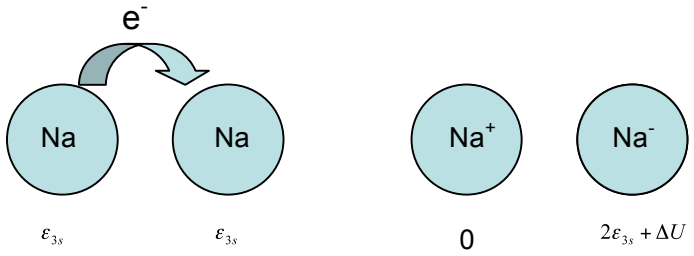


Fig. 2.1: *Electron hopping process*.

The hamiltonian to describe these processes was proposed first by Hubbard [1] and is give by

$$H = -\sum_{\langle i,j\rangle,s} t_{ij}\left(c^{+}_{s,i}c_{s,j} + c^{+}_{s,j}c_{s,i}\right) + U\sum_{i} c^{+}_{s,i}c_{s,i}c^{+}_{\bar{s},i}c_{\bar{s},i} \qquad (2.1)$$

where t_{ij} is the matrix element describing the electron hopping between nearest neighbour Hubbard sites $\langle i, j\rangle$, $c^{+}_{s,i}, c_{s,i}$ are the creation and destruction operators for an electron in the site i with spin s. The first term, in the Hamiltonian, describes the kinetic energy of the electrons, the second is the Coulomb repulsion between electrons sharing the same orbital. Since, for $U = 0$ no electron correlations are

present, and the solutions of H are simple crystal bands, the relevant limit is set by the condition $U >> t$. Under this condition, double occupancy is no more favourable and in the ground state there is one electron at each site, so the system is insulating even if the filling is only one half. Moreover, the localization of an odd number of electrons per unit cell causes the existence of strongly localized spin magnetic moments.

For $t = 0$, i.e. in the atomic limit, the ground state has a huge degeneracy (for N electrons and L sites, $N \leq L$, there are $C_N^L \cdot 2^N$ different ground states). When a small hopping term $t << U$ is switched on, these states are mixed and the sharp atomic level is broadened into a set of completely filled or empty Hubbard sub-bands. For example, in 3*d*-transition metal compounds, the correlation effects split the partially filled *d*-band into a set of Hubbard sub-bands, which are embedded in the sequence of wider bands derived from the ligand (quite often oxygen 2*p* bands) and the metal 4*sp*-hybridized bands.

Copper-oxide based compounds belong to this class of materials showing an impressive variety of physical properties such as the high-temperature superconductivity, which still represents one of the most important unresolved problems of the present days physics. Also $CuGeO_3$ represents one of these cases, since the origin of the spin-Peierls transition in this compound is still an open question.

In copper oxide based compounds, the key properties are related to the O–Cu–O bond structure, that is often characterized by planes where the CuO_4 cluster forms edge sharing or corner sharing "plaquettes" (see Fig 2.2).

$CuGeO_3$ is based on edge sharing "plaquettes" and in the Cu-O "plane" three types of hopping are possible;

i) the hopping from a Cu ion to a neighbouring Cu ion, characterized by an energy U_{dd};

ii) the hopping frpm an O ion to a neighbouring O ion, characterized by an energy U_{pp};

iii) the hopping from an O ion to a Cu ion, characterized by an energy Δ_{pd} (see fig.2.3).

a)

b)

Fig. 2.2 *Different geometries of the CuO_4 plaquettes in Cu-based compounds. The filled dots represent Cu ions, the empty circles are the oxygens.* a) *edge-sharing plaquettes;* b) *corner-sharing plaquettes, typical of copper-based HT superconductors.*

The single Hubbard band must then be replaced by a multi-band [11,12]. Therefore, taking into account only the first and second nearest neighbour interactions, the hamiltonian can be written as:

$$\begin{aligned} H = {} & \varepsilon_d \sum_{i,s,\alpha} \left(d_{s,i}^{\alpha}\right)^{+} d_{s,i}^{\alpha} + \varepsilon_p \sum_{i,s,\alpha} \left(p_{s,i}^{\alpha}\right)^{+} p_{s,i}^{\alpha} - t^{pd,\sigma} \sum_{\langle i,j\rangle,s,\alpha} \left[\left(p_{s,j}^{\alpha}\right)^{+} d_{s,i}^{\alpha} + \left(d_{s,i}^{\alpha}\right)^{+} p_{s,j}^{\alpha}\right] + \\ & - t^{pd,\pi} \sum_{\substack{\langle i,j\rangle,s,\alpha \\ \alpha\neq\beta}} \left[\left(p_{s,j}^{\alpha}\right)^{+} d_{s,i}^{\beta} + \left(d_{s,i}^{\beta}\right)^{+} p_{s,j}^{\alpha}\right] - t^{pp} \sum_{\langle j,j'\rangle,s,\alpha} \left[\left(p_{s,j}^{\alpha}\right)^{+} p_{s,j'}^{\alpha} + \left(p_{s,j'}^{\alpha}\right)^{+} p_{s,j}^{\alpha}\right] + \\ & + U_{dd} \sum_{i,\alpha} \left(d_{s,i}^{\alpha}\right)^{+} d_{s,i}^{\alpha} \left(d_{\bar{s},i}^{\alpha}\right)^{+} d_{\bar{s},i}^{\alpha} + U_{pp} \sum_{i,\alpha} \left(p_{s,i}^{\alpha}\right)^{+} p_{s,i}^{\alpha} \left(p_{\bar{s},i}^{\alpha}\right)^{+} p_{\bar{s},i}^{\alpha} + \\ & + \Delta_{pd} \sum_{\langle i,j\rangle,s,\alpha} \left(p_{s,j}^{\alpha}\right)^{+} p_{s,j}^{\alpha} \left(d_{s,i}^{\alpha}\right)^{+} d_{s,i}^{\alpha} \end{aligned} \tag{2.2}$$

where now $d_{s,i}^{+}, d_{s,i}$ and $p_{s,j}^{+}, p_{s,j}$ are the creation and destruction operators for a hole of spin *s* in the *d*-shell of the Cu in the site *i* and in the *p*-shell of the O in the *j*-site respectively. In the Hamiltonian three types of hopping processes, described by three hopping parameters, are present, being $t^{pd,\sigma}$ the most significant, whereas t^{pp} can be neglected, since the number of oxygen sites with a hole is very small (see sub-section 4.1 for more details).

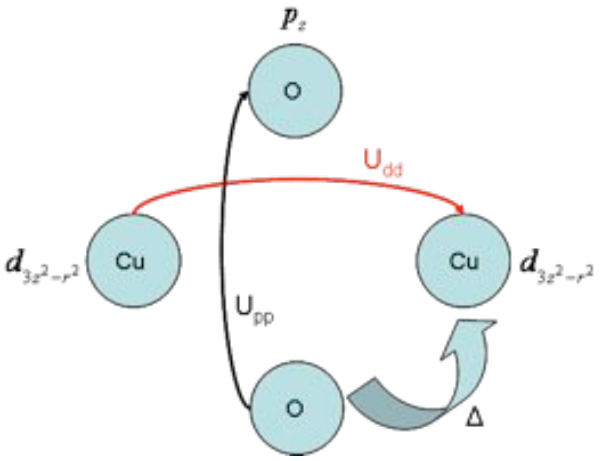


Fig. 2.3: *Electron hopping processes in Cu-O planes of $CuGeO_3$*

Fig. 2.4 a) sketches the electronic structure for a Mott Insulator (MI), where the smaller gap is between two Hubbard sub-bands, while Fig. 2.4 b) shows the case for a Charge Transfer Insulators (CTI), where the lowest excitation involves an electron transition from the 2p-band into the upper Hubbard sub-band.

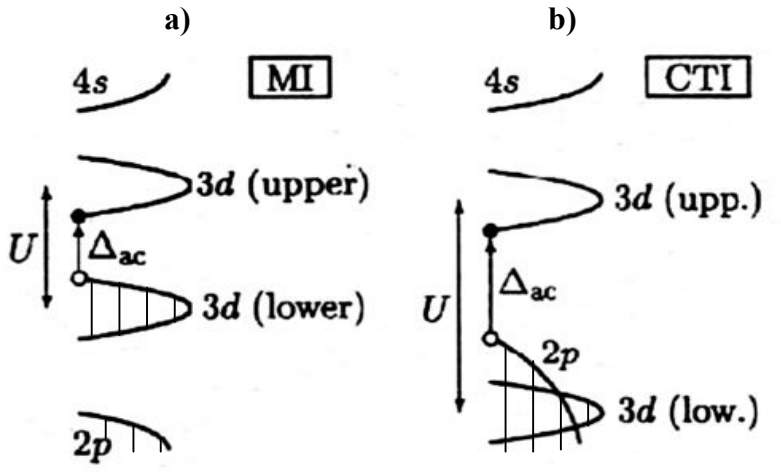


Fig. 2.4: *The character of the insulator is set by the lowest excitation energy necessary to create a charge carrier. The Mott Insulator (MI) has the smallest gap between Hubbard sub-bands, while in the Charge Transfer Insulator (CTI) the lowest excitation involves the transfer of an electron from the ligand p band to the upper Hubbard sub-band.*[1]

For transition metals based strongly correlated compounds, a useful phenomenological "phase diagram" was proposed by Zaanen, Savatzky and Allen (ZSA) [5](see fig. 2.5). The ZSA diagram reports the metal versus insulator character of the strongly correlated systems on the basis of the relative values of Δ_{pd}, U_{dd} , t and the *d*- and *p*-bands bandwidths, W_{dd} and W_{pd} respectively, where the broadening of the quasi-particle and quasi-hole levels into bands can be accounted for by

$$\Delta_{ac} = \Delta_{pd} - \frac{W_{dd} + W_{pd}}{2} \tag{2.3}$$

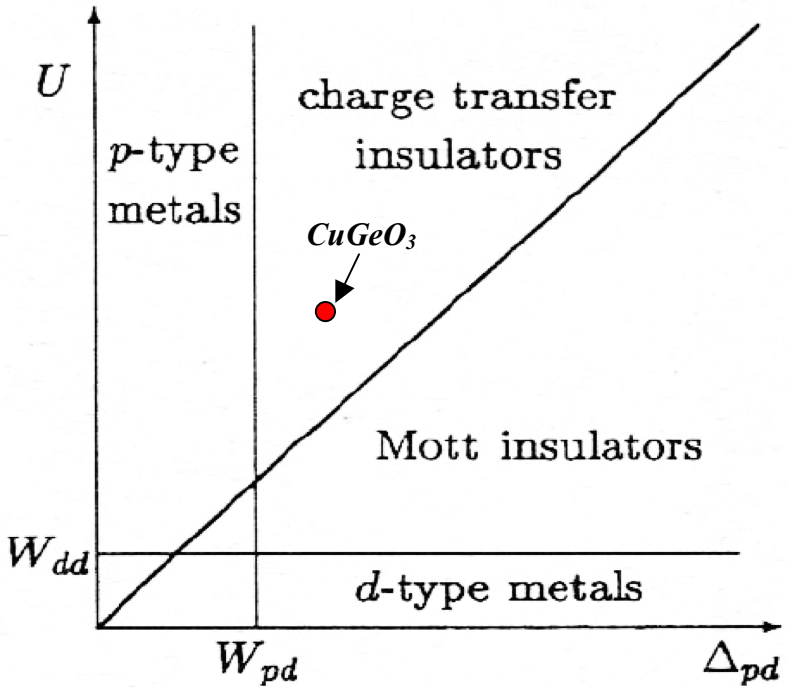


Fig. 2.5: *The Zaneen-Sawatzky-Allen diagram for the classification of strongly correlated systems. For* $U, \Delta_{pd} >> t$, *if* $U < \Delta_{pd}$ *a Mott insulator is expected, while for* $U > \Delta_{pd}$, *which is the case of* $CuGeO_3$, *the compound is a charge transfer insulator. In general, increasing the hybridization, the system go through an insulator-metal transition*. [1]

2.2 The case of the cuprates

In copper oxide based compounds transfer energy process is given by,

$$\Delta_{pd} = E_0(d^{n+1}\underline{L}) - E_0(d^n) \tag{2.4}$$

where $\underline{L}$ denotes a hole in the ligand band. Because of the electronic configuration of a copper atom, i.e. [Ar] $4s^2\ 3d^9$, copper-oxide based CT insulators represent a special case among the other CT compounds, since the *O 2p→Cu 3d* charge transfer process tends to make the *d*-shell fully symmetric ($3d^{10}\underline{L}$) even if the ground state ligand-orbital geometry is strongly distorted, i.e. far from the O_h group symmetry.

As previously reported, many copper-oxide-based compounds form "plaquettes" made of a copper ion bounds to four oxygen ions, with the sequence of the Cu ions anti-ferromagnetic ordered. In these systems the charge transfer process can induce the formation of an excitonic state, where a copper hole and an oxygen hole are coupled to form a singlet state. This state, first proposed by Zhang and Rice is known as Zhang-Rice (ZR) singlet [9] (see also section 3.3).

Remembering that in copper-oxide-based compounds the "plaquettes" can be connected by corners or by edges, different geometries of the Cu-O-Cu bonds are possible. The different symmetries of the Cu-O-Cu bonds have strong effects on the mobility of the ZR exciton. In fact, the ZR singlet can be delocalized through the lattice, without disturbing the anti-ferromagnetic spin background, with a delocalization range depending on the Cu-O-Cu angle, being maximum at 180° and minimum at 90°. This can be easily explained by noticing that for a 180° Cu-O-Cu bond-angle the copper ions in the two neighbouring "plaquettes" are connected through the same O_{2p} orbital, therefore increasing the mobility of the ZR state. On the contrary, for 90° Cu-O-Cu bond-angle the O_{2p} orbital involved in the formation of the ZR singlet is orthogonal to the O_{2p} orbital that makes the bound with the copper of the neighbouring "plaquette" and the probability of delocalizing the ZR is reduced.

In particular, the delocalization of the ZR singlet in $CuGeO_3$ has been measured recently and it has been proposed to be extended, at most, up to few CuO_4 "plaquettes" [13]. This finding is quite consistent with the fact in this compound the Cu-O-Cu bond-angle is ≈ 98°.

Bibliography

[1] P.Fazekas, *Electron Correlation and Magnetism,* World Scientific, Singapore (1999)

[2] N.F.Mott, *Metal Insulator Transitions,* Taylor and Francis, London (1990)

[3] A.Damascelli, Z.Hussain, Z-X.Shen, Reviews of Modern Physics **75**, 473 (2003)

[4] A.Damascelli, D. van der Marel, G.Dhalenne and A.Revcolevschi, Cond. Matt/9906159 v1 (1999)

[5] J.Zaneen, G.A.Sawatzky and J.W.Allen, Phys. Rev. Lett. **55**, 418 (1985)

[6] J.Kanamori, J.Phys. Chem Solids **10**, 87 (1959)

[7] P.W.Anderson, Solid State Phys. **14**, 99 (1963)

[8] H.Völlenke, A.Wittmann and H.Nowtny, Monatsh. Chem. **98**, 1352 (1967)

[9] F.C.Zhang and T.M.Rice, Phys. Rev. B **37**, 3759 (1988)

[10] M.E.Simon, A.A.Aligia and R.Gagliano, Phys. Rev. B **56**, 5637 (1997)

[11] Y.Mizuno *et al.*, Phys. Rev. B **57**, 5326 (1998)

[12] M.Imada, A.Fujimori and Y.Tokura, Rev. of Modern Phys **70,** 1039 (1998)

[13] S.Atzkern *et al.*, Phys. Rev. B **64**, 075112 (2001)

Chapter 3

Photo-excitation processes through the gap in CT insulators

This chapter is devoted to the description of the main effects induced by the photo-excitation processes through the gap of a charge transfer insulator. In particular, the photo-excitation of the ZR-singlet is presented and discussed.

3.1 Photo-excitation processes through the gap in solids

The photo-excitation of a solid by infrared (IR) and optical photons can induce different effects depending on the nature of the solid. In particular, in metals the electronic excitations can be induced by photons with arbitrarily small energy, while in insulators and semiconductors the presence of a gap requires photons with energy $\hbar\omega > \Delta E_{gap}$ in order to be absorbed through a linear process. This case will be analyzed in the followings. The photo-excitation may regard an electronic transition or it may induce lattice oscillations. It can also induce phase-transitions. The evolution of the physical properties of a solid excited by very short pulse of light

can be described by a semiclassical hamiltonian where the light is regarded as a high frequency electromagnetic field perturbing the system (this implies the intensity of the electric field significantly smaller than the atomic coulomb field), by averaging the statistical operator over the period of perturbation. When this approach is applied to electrons it is possible to intruduce the concept of photo-generation (or photo-doping) where the rate of photo-doping is proportional to the intensity of the radiation that induces the electron distribution between the ground and the excited state.

A detailed description of these processes outtakes the scope of the present thesis, while it is important to point out here that the photo-induced electronic distribution in a solid can give rise to a great variety of dynamic phenomena ranging from photo-induced phase transitions, band gap collapse, generation of coherent phonons and partially inverted electronic distribution. I am particularly interested to study some details of the generation of coherent phonons excited by photo-induced ZR excitons. For the first time it is demonstrated that coherent phonons can be excited in a solid not only by shaking the solid through a shock wave but also by a very selective electronic excitation.

In general, the electronic excitation are very fast. i.e. in the scale of few femtoseconds, while the coupling between the excited electronic stated and lattice (electron-phonon coupling) has longer timescales, i.e. in the picosecond time domain. Also the decay times are very different for the electronic and the phononic excitations. The first is quenched after tens of femtoseconds, while the excited phononic states can survive up to few nanoseconds.

This very interesting picture points to the fact that the phononic states are (in general) excited after a significant lethargy, while the decay of the excited phonon states contains very interesting parameters such as the electron-phonon coupling time and the damping factor. Of course these parameters can not be directly measured for thermally (incoherently) excited phonons. Only the excitation of coherent phonons will open gate to study by direct observation the dynamics properties of a crystal on the atomic scale.

3.2 Electronic effects

In the semi-classical perturbative approach, the operator H_I that couples the electromagnetic field and the atomic system can be written as the sum of the orbital coupling terms and the spin coupling terms for the electrons and the nuclei. In a first approximation, the nuclear part can be neglected, as well as the electronic spin magnetic coupling, that is generally about 100 times smaller than the orbital coupling. Under these assumptions, the coupling operator is

$$H_I \cong -\sum_{i=1}^{N} |q| \frac{\vec{p}_i}{m_e} \cdot \vec{A}(\vec{r}_i, t) \tag{3.1}$$

where $\vec{p}_i$ are the momenta of the N electrons of the atoms, q and m_e are the electronic charge and mass, and $\vec{A}(\vec{r}_i, t)$ is the electromagnetic vector potential, that, for a monochromatic e.m. field, can be written as

$$\vec{A}(\vec{r}_i, t) = A_0 \vec{\eta} e^{i[\vec{k}\cdot\vec{r} + \delta]} \tag{3.2}$$

where $\vec{\eta}$ is the polarization versor, A_0 the magnitude, $\vec{k}$ the wavevector and δ the relative phase. When sudden perturbation is applied for a time time t between $0 < t < T$ (for times larger than T the interaction is described by the Fermi golden rule) the transition probability between the initial state u_i and the final state u_f is given by

$$\begin{aligned} \Pi_{i\to f} &= \frac{2\pi}{\hbar} \left| \langle u_f | H_I | u_i \rangle \right|^2 \delta(E_f - E_i - \hbar\omega) \\ &= \frac{2\pi}{\hbar} A_0^2 q^2 \left| \langle u_f | \sum_{j=1}^{N} \frac{\vec{p}_j}{m_e} \cdot \vec{\eta} e^{i\vec{k}\cdot\vec{r}} e^{i\delta} | u_i \rangle \right|^2 \delta(E_f - E_i - \hbar\omega) \end{aligned} \tag{3.3}$$

When λ is significantly larger than the orbital dimensions, i.e. the "*electric dipole approximation*" can be applied, the term can be set $e^{i\vec{k}\cdot\vec{r}} \approx 1$. In this case, since the electric dipole is an odd operator, the only allowed transitions are those between states with opposite parity. From 3.3, the only permitted transitions are those for which $h\nu = E_f - E_i$. However, because of the finite life-time of the orbitals and bands, the $\delta(E_f - E_i - \hbar\omega)$ in eq. 3.3 should be replaced by a Lorentzian distribution that reflects the shape of the former. Of course, in strongly correlated system a proper Lorentzian distribution is complicated by the fact that the band structure can

not be predicted by the independent-electron model. Nonetheless, in both cases the allowed transitions in solids, within the dipole approximation, are prevalently resonant transitions between states of opposite parity.

In the present context a particular case of photo-excitation in condensed matter is represented by the band-gap collapse in semiconductors and the following semiconductor-metal transition induced by intense and ultra-short laser pulses [23-26]. This mechanism has been explained as the result of the excitation in the valence band of electrons involved in covalent bonds. As a consequence, the covalent bonding is destabilized, while the ionic potential of the nuclei is screened by the free-carriers many-body effects. The net result is a modification and a broadening of the electronic bands, reflected by the fact that the transition resonant frequency decreases, while the band-gap tends to close.

A similar mechanism seems to be present, but for completely different reasons, also in some strongly correlated systems [22]. In fact, in the latter the reason for the insulating character resides in the strong Coulomb repulsion of electrons sharing the same shell, that makes the hopping of an electron from a site to the neighbouring one unfavourable and creates the Hubbard subbands. For example, in the case of $CuGeO_3$, the insulator character is due to the Coulomb repulsion between the neighbouring holes of the cations (CT insulator). If the photo-excitation induces the full occupation of the *d*-shell on a Cu ion, the Coulomb repulsion is quenched, and consequently, under a strong enough photo-doping, the beginning of the gap collapse should be observed. Of course, if this photo-excitation is too intense, the entire crystal structure can collapse. For example, the threshold limit for reversible effects in $CuGeO_3$ is set at about 4% of photo-doping for CT photo-excitations with pulses of 3.14 eV [1].

3.2 Photo-excitation of the Zhang-Rice singlet

Among the electronic excitations, the Zhang-Rice singlet, that occurs in $CuGeO_3$, as well as in other copper oxide based compounds, is particularly important. This excitation is characterized by a charge transfer process from the Cu 3*d* to the O 2*p* orbitals of the Cu-O plaquettes characteristic of these compounds.

The Zhang-Rice singlet [9] is a state formed when an antiferromagnetic coupling is established between a 3*d* hole of Cu and another hole, localized between the O_{2p} orbitals of the four oxygen atoms belonging to the same CuO_4 plaquette. In particular, at the second order in perturbation theory, it can be shown [9] that the antisymmetric combination of the four O_{2p} orbitals is antibonding, while the two possible symmetric combinations (a singlet and a triplet) are bonding, and the lower energy state is a singlet. The extra hole can be introduced by hole-doping, but in the case under investigation it is induced by the photoinduced charge-transfer process. In this case, an electron transfer from one $O_{2p}(\sigma)$ orbital to the Cu ion creates a hole on the O ion, and this hole is coupled to the Cu 3*d* hole of the neighbouring plaquette (see fig.3.1) to form a spin singlet. Due to these effects, the elementary charge transfer process in the Cu-O plane is a bound exciton consisting of an electron on a Cu ion and a spin singlet of Cu-O holes on the neighbouring plaquette. In cuprates the ZR singlet has been mainly observed and studied by valence band one–electron removal spectroscopy (photoelectron emission) [Ref.], while only recently other spectroscopic techniques such as RIXS (Resonant Inelastic X-ray Scattering) has been used to study the ZR singlet [Ref.].

The presence of the Zhang-Rice singlet in $CuGeO_3$ was for many years a vexed question, because there is no evidence in the photoemission spectrum of any structure related to the ZR singlet. However, absorption spectroscopy in the 1 – 4 eV photon energy range has shown, for linearly polarized light parallel to the c-axis, a feature at about 3.2 eV that has been ascribed to the formation of the ZR exciton [13,14]. Rather interesting is the fact that the intensity of this structure is strongly dependent on the polarization of the incident light. It is maximum for E//*c*, and it is completely quenched for E//*b*. This is due to the fact that only the charge transfer from a O ion in the CuO_4 plane can induce the ZR exciton, which in turn reflects the fundamental role played by the in-plane oxygen, bond to two Cu^{2+} ions [2,4,5]. Moreover, this feature shows a marked enhancement by lowering the temperature, with a small energy blue-shift, as reported in fig. 2.6. Pagliara *et al.* [4] demonstrated that this effect can't be explained with the thermal expansion, and therefore it must be due to the renormalization effects, and in particular to electron-phonon interactions and to spin ordering effects.

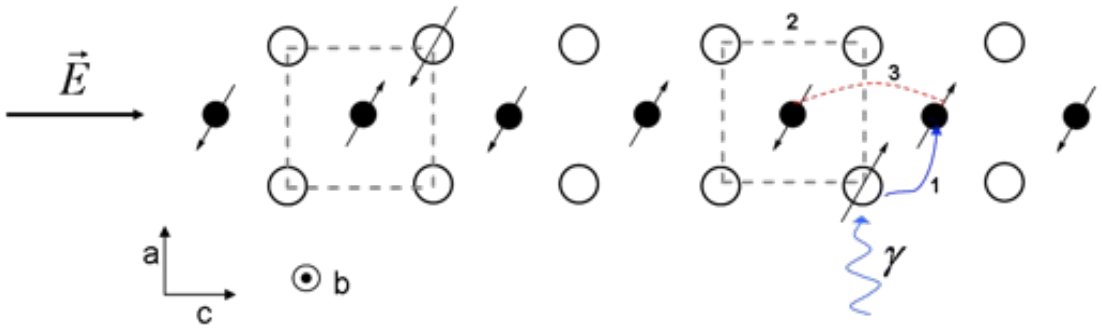


Fig. 3.1: *Zhang-Rice exciton formation in the Cu-O plane:* **1)** *the transfer of an electron from an oxygen 2p to a Cu 3d orbital with an absorption of a photon;* **2)** *thanks to the antiferromagnetic ordering of the Cu ions, the hole on the oxygen can couple to the hole on the neighbour Cu ion to form a bound singlet state (ZR singlet);* **3)** *the Coulomb attraction binds the Zhang-Rice singlet formed in 2) with the electron on the Cu ion of the neighbour plaquette.*

. Finally, it has been shown [4] that the Si substitution of Ge has the double effect to increase slightly the energy of the ZR structure and to strongly enhanced its intensity. Phenomenologically this effect can be explained by observing that the Si ions are smaller than the ones of Ge, so there is a reduction in the hybridization between the O2p_y orbital with the Si, which causes an increase in the degree of in-plane hybridization with an enhancement of the ZR singlet intensity.

3.3 Lattice effects

The electronic photo-excitation of a solid can give rise to two main lattice behaviours: *i*) a phase transition, or *ii*) oscillation of the ions around their equilibrium position (phonons). Here we are interested to study the phonon generated by the CT photo-excitation process.

There are mainly five mechanisms in which the phonons of a crystal lattice can be excited: *i*) the heating up of the system, *ii*) IR or THz resonant absorption, *iii*) photon scattering (Raman or Brillouin), *iv*) phonon-phonon coupling with another excited mode, and *v*) the relaxation of an electronic transition through the electron-phonon coupling. In general, when a non-coherent light source illuminates a crystal, all these processes can give rise to the excitation of lattice phonons, but these vibrations do not have long-range phase correlation. Instead a coherent pulse can excite the modes coherently, i.e. in phase. The lattice oscillations induce rigid oscillations of the electronic states. A local oscillating dielectric function results, and the phase coherence on the long range provides an effect that does not vanish as for non- coherent oscillations. The coherently induced perturbation of the complex dielectric function modifies both transmittivity and reflectivity. Therefore, the oscillation of these quantities can be directly related to the coherent excitation of the respective phonons.

The mechanism of coherent phonons excitation in solids with femtosecond light pulses has been largely studied in the last 20 years. At the present, the theory of Displacive Excitation of Coherent Phonons (DECP) has been recognize as a particular case of Impulsive Stimulated Raman Scattering (ISRS), whose driving force contains both an impulsive scattering component and a displacive component that takes into account the sudden shift in the equilibrium position of the lattice ions due to coupling with the photoexcited carries created by the optical pulse [17,18,26]. In addition, also coherent acoustic modes have been observed recently.

Finally, also the electron-phonon coupling can be involved in the formation of such coherent phonons [27]. The equation of motion for the average atomic displacement operator of wave vector $\vec{q}$, $\left\langle \hat{Q}_{\vec{q}} \right\rangle(t)$, can be written in the form

$$\left\langle \hat{Q}_{\vec{q}} \right\rangle(t) = F_{\vec{q}}(t) + \frac{1}{i\hbar}\left\langle \left[\hat{P}_{\vec{q}}, \hat{H}_{ph,ph}\right] \right\rangle(t) \tag{3.6}$$

where the commutator between the momentum operator $\hat{P}_q$ and the Hamiltonian of phonon-phonon interaction, $\left[\hat{P}_q, \hat{H}_{ph,ph}\right]$, represents the relaxation contribution due to phonon-phonon interaction and $F_{\vec{q}}(t)$ is the driving force caused by electron-phonon interaction:

$$F_{\vec{q}}(t) = \frac{1}{i\hbar}\left\langle\left[\hat{P}_{\vec{q}}, \hat{H}_{e,ph}\right]\right\rangle(t) \tag{3.7}$$

with

$\hat{H}_{e,ph} =$ (vorrei avere le formule che usano nel libro[27], eq 19.2 e 6.31) (3.8)

$\hat{H}_{ph,ph} =$ (3.9)

Called $C_{\vec{q}}^{(c)}$ the coupling constant between the $\vec{q}$ lattice mode and the excited electrons, and $C_{\vec{q}}^{(v)}$ the one between the $\vec{q}$ lattice mode and the holes in the valence band, $F_{\vec{q}}(t)$ results to be proportional to the difference $C_{\vec{q}}^{(c)} - C_{\vec{q}}^{(v)}$ and to the Fourier component of the photo-excited electron density. Even if the total generated charge is zero[1], the built-in microscopic electric field acting on electrons and holes is different. Therefore, opposite charges drift in opposite directions, and the resulting electric field acts on the ionic lattice.

$F_{\vec{q}}(t)$ can excite only phonons with $\vec{q}$ much smaller than the Brillouin zone. Neglecting the phonon-phonon term, the solution of 3.6 with initial condition $\left\langle\hat{Q}_{\vec{q}}\right\rangle(t \to \infty) = 0$ is

$$\left\langle\hat{Q}_{\vec{q}}\right\rangle(t) = \int_{-\infty}^{t} dt' \frac{\sin\left[\omega_q (t - t')\right]}{\omega_q} F_{\vec{q}}(t) . \tag{3.10}$$

Because of the oscillating nature of the integral expression, the coherent phonon oscillation can be induced only by ultrafast pump pulses, for which the characteristic time scale of $F_{\vec{q}}(t)$ is smaller than ω_q^{-1} [27].

Returning to 3.6, there are mainly two mechanisms to take into account the damping of coherent oscillations: the pure dephasing, due to elastic scattering between phonons and excited electrons, and the population decay, due to phonon-phonon interactions caused by the anharmonicity of the crystal potential. For each material, the dominating term at the origin of the phenomenon can be recognized analyzing the temperature and fluence dependence of the decay rate [28] or

[1] Because the number of excited electrons equals the number of the holes created in the valence band

comparing the decay times and frequencies for the same phonon, coherently and incoherently excited [29].

While the pure dephasing is directly proportional to the density of photo-excited electrons, the population decay process depends strongly only from lattice temperature. The increasing decay rate upon increasing temperature is well explained by the anharmonic decay model. The lowest order anharmonic term in the crystal potential is the third order one, and for weak interactions, anharmonicity leads to a Lorentzian broadening of the phonon lines [30]. While the excitation of acoustic phonons can be described with the equation of motion for the classical oscillator damped by a friction force, to describe damping of coherent oscillation of optical phonons it is necessary to develop a microscopic model. As a result, at the first order two processes turn out to be responsible for the phonon relaxation. The first is the decay of the coherent phonon ω_0, with wave vector k~0, into two lower energy phonons ω_1 and ω_2, with opposite wave vectors. The second is an up-conversion process, where the initial phonon is scattered by a thermal phonon into a new phonon of higher energy. At higher orders, also three-phonon processes may be relevant. Such lattice anharmonicities are also responsible, with the thermal expansion, of the redshift of the phonon peak frequency as the temperature increases. When third order anharmonic terms dominate, at high temperatures there is a linear variation of the relaxation rate with the temperature, while higher order mechanisms result in a non-linear temperature dependence of the relaxation rate [30].

Bibliography:

[1] D.Nardi, Thesis, università degli studi di Brescia, 2005/2006

[2] S.Pagliara, Ph.D. Thesis, università degli studi di Brescia, 1999

[3] V.Corradini, A.Goldoni, F.Parmigiani *et al*, Surface Science **420**, 142 (1999)

[4] S.Pagliara, F.Parmigiani, P.Galinetto, A.Recolevschi and G.Samoggia, Phys. Rev.B **66**, 024518 (2002)

[5] F.Bondino, M.Zangrando, M.Zacchigna, G.Dhalenne, A.Recolevschi and F.Parmigiani, Phys. Rev.B **75**, 195106 (2007)

[6] M.Bassi, P.Camagni, R.Rolli, G.Samoggia, F.Parmigiani, G.Dhalenne and A.Recolevschi, Phys. Rev.B **54**, 11030 (1996)

[7] P.W.Anderson, Solid State Phys. **14**, 99 (1963)

[8] H.Völlenke, A.Wittmann and H.Nowtny, Monatsh. Chem. **98**, 1352 (1967)

[9] F.C.Zhang and T.M.Rice, Phys. Rev. B **37**, 3759 (1988)

[10] C.de Graaf, R.Broer, Phys. Rev.B **62**, 702 (2000)

[11] H.Eskes, L.H.Tjeng and G.A.Sawatzky, Phys. Rev.B **41**, 288 (1990)

[12] K.Okada and A.Kotani, Phys. Rev.B **63**, 045103 (2001)

[13] K.Okada and A.Kotani, Phys. Rev.B **65**, 144530 (2002)

[14] Y.Mizuno, T.Tohyama, S.Maekawa, T.Osafune, N.Motoyama, H.Eisaki, S.Uchida, Phys. Rev.B **57**, 5326 (1998)

[15] F.Parmigiani and L.Sangaletti, J. Of Electron Spectroscopy **107**, 49 (2000)

[16] I.Bozovic, M.Schneider *et al.*, Phys. Rev.B **69**, 132503 (2004)

[17] H.Zeiger, J.Vidal, T.K.Cheng, E.P.Ippen, G. and M.S. Dresselhaus, Phys. Rev. B **45,** 768 (1992)

[18] G.A.Garrett, T.F.Albrecht, J.F.Whitaker and R.Merlin, Phys. Rev. Lett. **77**, 3661 (1996)

[19] A.I.Lobad and A.J.Taylor, Phys. Rev. B **64,** 180301 (2001)

[20] B.K.Agarwal, *X-Ray Spectroscopy,* II ed, Springer-Verlag, 1994.

[21] B.H.Bransden and C.J.Joachian, *Physics of atoms and molecules,* Longman Scientific & Technical editions, 1995.

[22] L.Perfetti *et al.*, Phys. Rev. Lett. **97,** 067402 (2006)

[23] L.Huang, J.P.Callan, E.N.Glezer and E.Mazur, Phys. Rev. Lett. **80,** 185 (1998)

[24] Y.Siegal, E.N.Glezer and E.Mazur, Phys. Rev. B **49,** 16403 (1994)

[25] E.N.Glezer, Y.Siegal, L.Huang and E.Mazur, Phys. Rev. B **51,** 6959 (1995)

[26] T.E.Stevens, J.Kuhl and R.Merlin, Phys. Rev. B **65,** 144304 (2002)

[27] F.T.Vasko and O.E.Raicnev, *Quantum Kinetic Theory and Applications-Electron, Photons, Phonons*, Springer (2005)

[28] M.Hase, K.Ishioka, J.Demsar, K.Ushida and M.Kitajima, Phys. Rev. B **71,** 184301 (2005)

[29] M.Hase, K.Mizoguchi, H.Harima, S.Nakashima and K.Sakai, Phys. Rev. B **58,** 5448 (1998)

[30] F.Vallée, Phys. Rev. B **49,** 2460 (1994)

Chapter 4

The $CuGeO_3$ and its properties

$CuGeO_3$ is an inorganic compound classified as a charge transfer insulator, with a spin-Peierls (SP) transition at 14. This discovery has lead to an intensive experimental investigation on pure and Mg, Zn and Si substituted $CuGeO_3$ crystals. Nonetheless a detailed understanding of the origin of the SP transition in this system is still missed. In this chapter a description of such compound is given, with particular attention to its electronic properties and optical absorption features. In the last section an overview of the phononic spectrum of this compound is reported.

4.1 Crystal structure of $CuGeO_3$

At room temperature, the crystal structure usually proposed for $CuGeO_3$ is orthorhombic with lattice parameters a=4.81Å, b=8.47Å, c=2.94Å [2]. The space group is *Pbmm* (x//a, y//b, z//c) or, in standard setting, *Pmma* (x//b, y//c, z//a). The building blocks of the crystal structure are edge-sharing CuO_6 distorted octahedra, where the Cu^{2+} ions are placed in chains running along the c axis, at the centre of a

square of four O^{2-} ions, and corner-sharing GeO_4 tetrahedra stacked along the *c* direction (see fig. 4.1) [10-15]. The unit cell contains two edge-sharing CuO_6 octahedra, strongly deformed, with two different Cu-O bonds. One with the apical oxygen, Cu-O(1), has a distance of 2.76 Å, significantly larger than the 1.94 Å Cu-O(2) distance of the CuO_4 plaquettes. The distortion causes also the Cu-O(1) bonds to be not perpendicular to the basal plane. The GeO_4 bonds form regular tetrahedra.

The relevant structural units are planar plaquettes of a Cu ion coordinated with four O(2) oxygen ions. The Cu ions form anti-ferromagnetic (AF) almost linear chains along the *c* direction, in which they are connected through O(2) pair bridges,

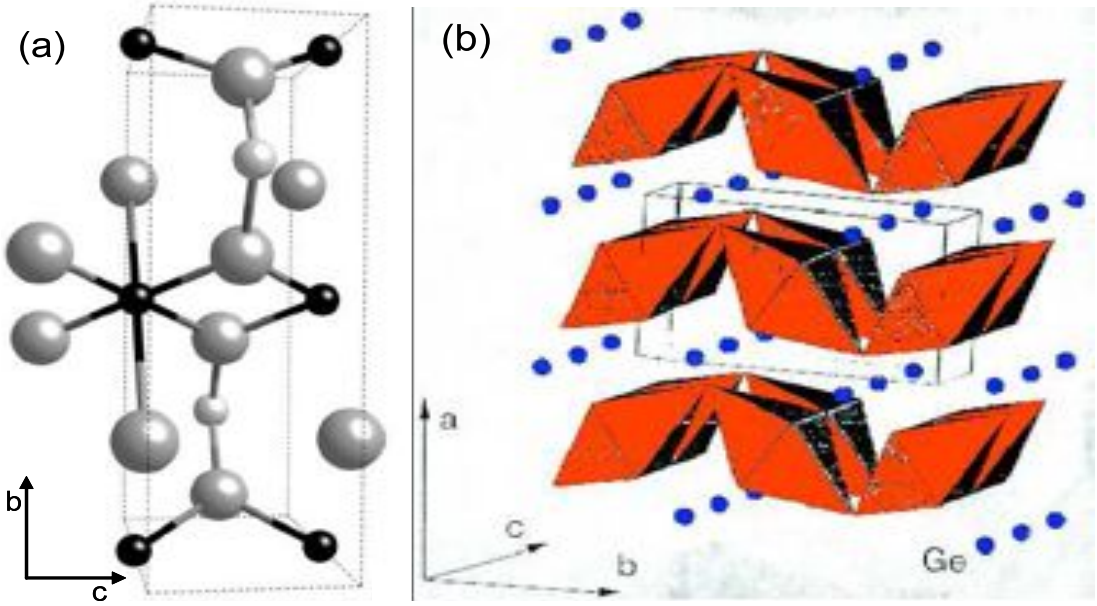


Fig. 4.1: *Crystal structure of $CuGeO_3$.* (a) *Unit cell: the dark spheres are the copper ions, large light spheres represent oxygen atoms, while the small light ones Ge ions. For one of the Cu the sixfold coordination is shown* [15]. (b) *Edge sharing CuO_6 octahedra stacked along the c direction* [10,11].

with a measured Cu-O-Cu angle of 98°. Although the measured angle is closer to 90° than to 180°, the compound results to be anti-ferromagnetic, in disagreement with the

Goodenough-Kanamori-Anderson (GKA) rule [5,6]. An explanation has been given from Damascelli and al. by considering the AF interaction as a consequence of the side-group effects [4].

This material has been largely studied after 1993, in search of the origin of the unusual spin-Peierls (SP) transition at 14K[23,24]. Even if so far the origin of this magnetic transition has not been clarified yet, many other interesting properties have been found in this compound.

$CuGeO_3$ is classified as a CTI with an $O_{2p} \rightarrow Cu_{3d}$ CT energy $\Delta \approx 3.5$ eV. This energy is smaller than the Coulomb repulsion $U_{dd} \approx$ 8-9eV. The presence of the Zhang-Rice singlet in $CuGeO_3$ has been, for many years, a vexed question and only in the last years it has been fully demonstrated [14]. Moreover, being the Cu-O-Cu angle only 98°, the ZR exciton is found to be quite localized in this compound, and $CuGeO_3$ remains insulator under photo-doping. Due to the charge transfer process, the ground state of such a compound can be represented as a linear combination

$$\psi = a\left|3d^9\right\rangle + b\left|3d^{10}\underline{L}\right\rangle \tag{4.1}$$

with $a >> b$.

Rather interesting is also to note that $CuGeO_3$ presents quite large empty cavities, related to the presence of spontaneous giant strains along all the three orthorhombic directions.

The samples studied for this experiment are blue single crystals of $CuGeO_3$, cleaved along the b-c plane in very thin pieces.

4.2 Group analysis

To analyze the electronic structure of $CuGeO_3$ it is necessary to recall some aspects about the ligand field and the group theories, in order to properly describe bonding structure starting from the symmetry properties.

The ligand field method describes complex systems in the approximation of purely ionic molecules. The central ion is surrounded by a charge distribution, originating from neighbouring ions, which produces an electrostatic “crystal” field

that interacts with the bonding, non-bonding and anti-bonding orbitals. The Hamiltonian of such a system can be limited to two terms, representing respectively the free ion term H_F and the perturbation $V(\vec{r})$ term, due to the surroundings charges' field:

$$H = H_F + V(\vec{r}) \tag{4.2}$$

In general, $V(\vec{r})$ lowers the site symmetry, since $V(\vec{r})$ is invariant under fewer symmetry transformations respect to H_F. By lowering the symmetry, a partial or complete lift of the otherwise degenerate molecular orbitals is achieved.

For $CuGeO_3$ the "weak field approximation" is generally adopted. In this case the effect of the perturbation is evaluated after the Coulomb interaction but before the spin-orbit term, and considering only the Cu *d*-orbitals. In a first approximation, the CuO_6 octahedra are assumed not distorted, with a D_{4h} symmetry. The simpler treatment for this problem consists in writing the crystal field potential $V(\vec{r})$ as the sum of a cubic and an axial field [1]. Since the Cu ion has nine *d*-electrons, it is possible to treat this case as the case of a single *d*-hole. Within these approximations and disregarding the spin, the cubic field (O_h) splits the original fivefold degenerate *d*-orbitals into a double degenerate E_g orbital ($d_{x^2-y^2}$, d_{z^2}) and a threefold degenerate one, T_{2g} (d_{xy}, d_{xz}, d_{yz}). Since the E_g orbitals extend toward the vertices of the octahedron, while the T_{2g} ones point toward the corners of the cube, the energy of the electronic E_g-state is higher than that of the T_{2g}-state [1]. However, because of the lower symmetry of the CuO_6 cluster, due to the different length of the Cu-O(1) and Cu-O(2) bonds, the E_g and T_{2g} orbitals are furtherly splitted into B_{1g} and A_{1g} the first and B_{2g} and E_{2g} double degenerate the second, as shown in fig. 4.3. Table 4.1 reports the bases wavefunctions of the irreducible representations. This model well reproduces the 3*d*-orbital energy splitting observed in the experiments [13,15].

The degeneracy of the E_{2g} orbitals is further removed by introducing the spin-orbit interaction.

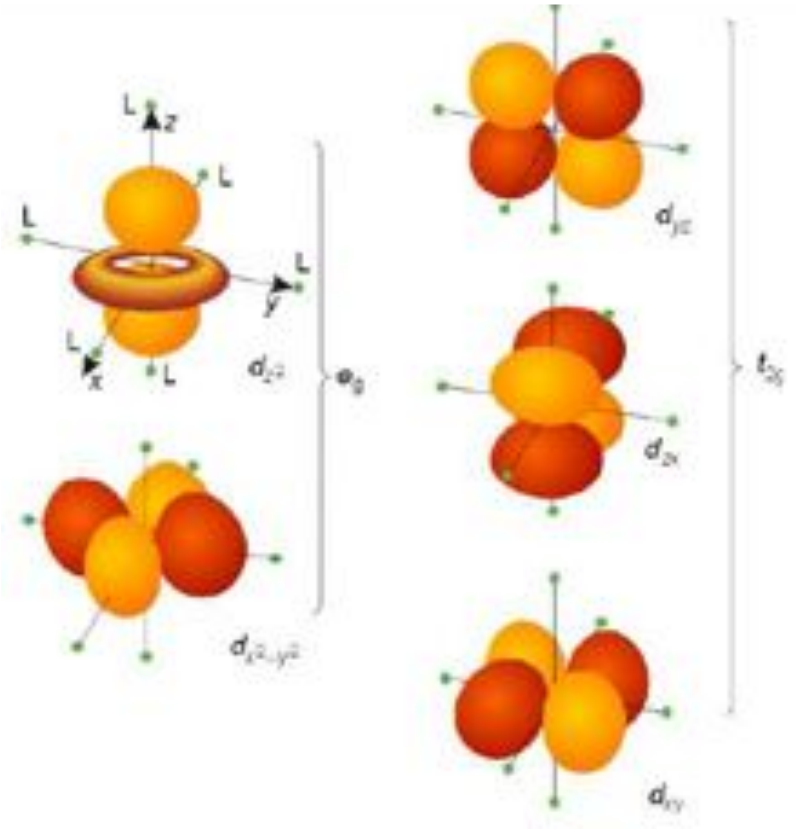


Fig. 4.2: *double degenerate E_g and threefold degenerate T_{2g} orbitals*

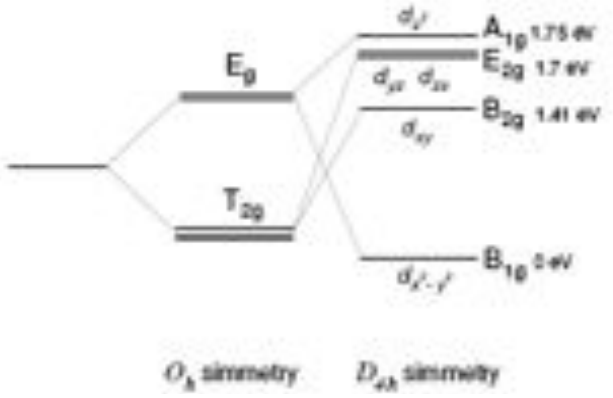


Fig. 4.3: *crystal field splitting of a d-electron orbital in cubic (O_h) and tetragonal(D_{4h}) symmetries* [10].

Irreducible representation	Orbital name	Atomic states	Cartesian notation
$A_{1g}\left(\Gamma^1\right)$	$d_{3z^2-r^2}$	$\lvert 2,0\rangle$	$\frac{3z^2-r^2}{2}$
$B_{1g}\left(\Gamma^3\right)$	$d_{x^2-y^2}$	$\frac{1}{\sqrt{2}}\left(\lvert 2,2\rangle+\lvert 2,-2\rangle\right)$	$\frac{\sqrt{3}}{2}\left(x^2-y^2\right)$
$B_{2g}\left(\Gamma^4\right)$	d_{xy}	$\frac{1}{i\sqrt{2}}\left(\lvert 2,2\rangle-\lvert 2,-2\rangle\right)$	$\sqrt{3}(xy)$
$E_{2g}\left(\Gamma^5\right)$	d_{xz} d_{yz}	$\frac{1}{i\sqrt{2}}\left(\lvert 2,1\rangle-\lvert 2,-1\rangle\right)$ $\frac{1}{i\sqrt{2}}\left(\lvert 2,1\rangle+\lvert 2,-1\rangle\right)$	$\sqrt{3}(xz)$ $\sqrt{3}(yz)$

Table 4.1: 3*d real base's functions of the irreducible representation of* D_{4h} *group.*

4.3 Optical absorption spectrum of $CuGeO_3$

Recent experiments has provided the optical absorption data versus temperature for $CuGeO_3$ oriented single crystals, with pump polarization along the *b* and *c* crystalline axes (see fig. 4.4, 4.5), and an explanation for the main features observed [16,11,13].

Rather interesting are the spectral regions A and B, shaded in fig. 4.4. In the spectral region A, the feature centred at 1.7eV is ascribed to the *d-d* transitions, forbidden in the dipole approximation but partially allowed by the lattice distortion and the electron-phonon interactions, as reported in experimental studies [11,12,13,14,16], and described by ab-initio methods [15]. The attribution of this band to not allowed dipole transitions is consistent with the relatively small value of the absorption coefficient μ (in the region between 1.4 and 2.3eV μ is everywhere lower than $1000cm^{-1}$) and by the phonon assisted character of these transitions, which is evidenced by the response of the optical absorption versus temperature [16]. In fact,

at low temperature the absorption structure consists of three main gaussian-like components[11]. On the basis of the crystal field method, it is argued that the three gaussians correspond to transitions from the ground state $3d_{x^2-y^2}$ to the first (d_{xy}), the second (d_{yz}, d_{zx}) and the third (d_{z^2}) excited states (see fig.4.3). The shape of the *d-d* band changes with light polarization (see fig.4.5). This is a consequence of the loose of the O_h symmetry, because of the different Cu-O bonds length along the *b* and *c* directions.

Rather interesting are also the absorption behaviours of region B. In fact, the absorption spectra show a clear dependence on the polarization but not on the temperature. This is a fingerprint of the fact that these features have an electronic origin. In fact, for both light polarizations, the absorption spectra show a strong

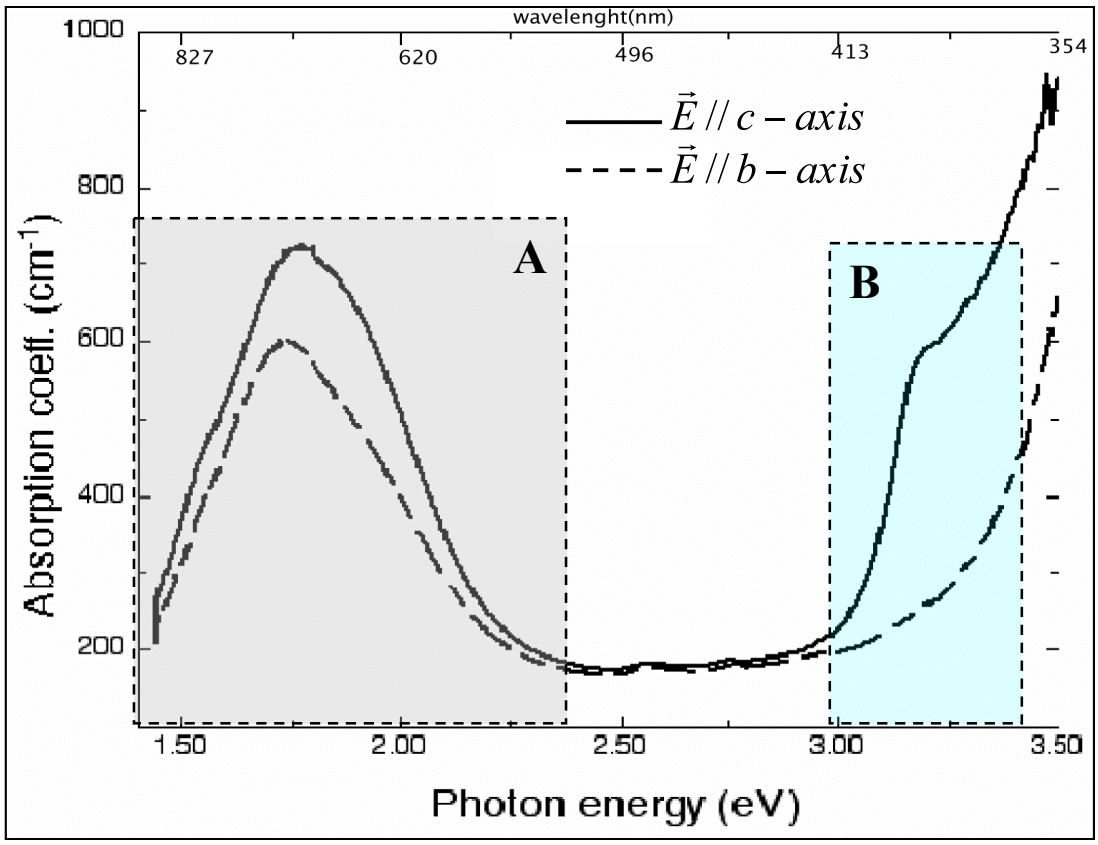


Fig. 4.4: *Absorption spectra of $CuGeO_3$ at room temperature, for both the light polarization indicated* [11]

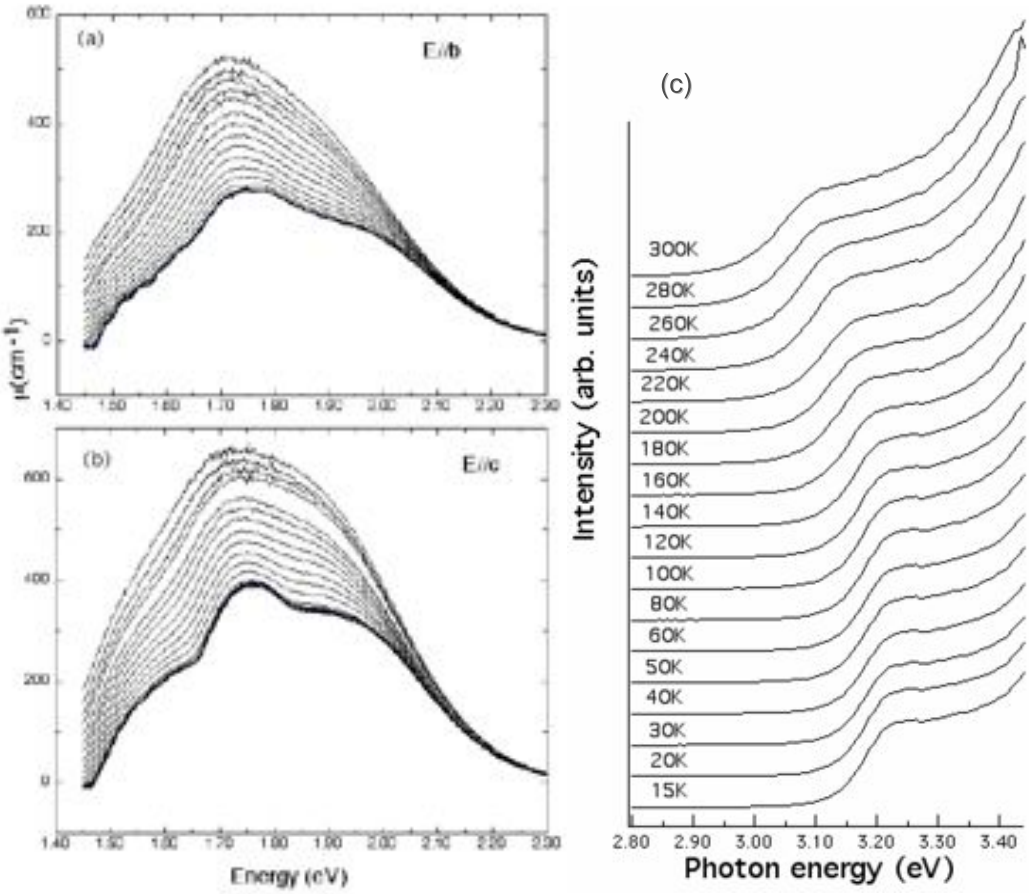


Fig. 4.5: (a,b) *Temperature dependence of d-d transitions in $CuGeO_3$, from T=15K (bottom curve) to room temperature (top curve).* (a) *Light polarization parallel to the b crystalline axis;* (b) *Light polarization parallel to the c-axis.* (c) *Temperature dependence of Z-R exciton for* $\vec{E} // c$ [11].

absorption at $h\nu \gtrsim 3$ eV. However, a clear shoulder at ~3.2 eV is observed for the E//*c* polarization. This absorption edge was attributed by Pagliara and co-workers [13] to the formation of a Z-R singlet in the Cu-O_4 plaquettes. The presence of a Z-R singlet at ~3.2eV has been recently confirmed by Resonant Inelastic X-ray Scattering (RIXS) experiments by Bondino and co-authors [14]. This finding is particularly important for the present experiment since it allows us to selectively pump two different light-induced charge transfer processes. The first, more conventional, applying the electric field along the *b* crystal axis, and therefore inducing a CT from the apical oxygen O(1) to the in-plane copper. The second, from an in-plane O(2) to

the copper ions, therefore allowing the formation of Z-R excitons. As we will see later, this will have significant consequences for the excitation processes.

4.4 Phonons in $CuGeO_3$

The discovery of the spin-Peierls transition at $T_{SP} = 14K$ in $CuGeO_3$ has led to numerous studies of the physical properties of this material. This transition is probably induced by the softening of a phonon, but experiments have not revealed its presence yet [18-21].

Various experiments has been performed to investigate the vibrational modes of the lattice, both with Raman and infrared (IR) techniques, and to compare them with the group-theoretical models. In particular, above T_{SP} 13 infrared and 12 Raman active modes are expected.

Mode	ω_{TO} (cm^{-1})	γ_{TO} (cm^{-1})	ω_{LO} (cm^{-1})	γ_{LO} (cm^{-1})	ε_0	ε_∞
B_{1u}	131	2	134	2		
	328	15	372	17		
	478	25	489	30	5.8	3.5
	615	10	640	17		
	843	15	880	25		
B_{2u}	165	1.5	168	2.5		
	530	15	600	30	5.0	3.0
	720	9	803	40		
B_{3u}	48	3	49	4		
	211	6	231	8		
	285	9	308	10	8.2	3.8
	377	12	414	17		
	772	15	857	25		
A_g	187	B_{1g}	388	B_{2g}	116	B_{3g}	110
	332				224		411
	594				427		712
	859				879		

Table 4.2: *Experimentally measured phonons in $CuGeO_3$. Above, room temperature frequencies (cm^{-1}) of transversal (ω_{TO}) and longitudinal (ω_{LO}) IR active modes, with the damping γ (cm^{-1}). Below, the frequencies of Raman active modes* [18].

In the complete picture of all the vibrational modes of a lattice, IR and Raman techniques permit to observe all the optical phonons. In fact, since the dipole and scattering operator have opposite symmetries, they can detect respectively all the odd and even modes of the lattice. They are reported in table 4.2 with the relative symmetries.

To complete the picture, the Brillouin scattering is needed, in way to detect the acoustic modes.

Bibliography:

[1] S.Sugano, Y.Tanabe and H.Kamimura, *Multiplets of Transition-Metal Ions in Crystal,* Academic Press, New York and London, 1970

[2] H.Völlenke, A.Wittmann and H.Nowtny, Monatsh. Chem. **98**, 1352 (1967)

[3] A.Damascelli, Z.Hussain, Z-X.Shen, Reviews of Modern Physics **75**, 473 (2003)

[4] A.Damascelli, D.van der Marel, G.Dhalenne and A.Revcolevschi, Cond. Matt/9906159 v1 (1999)

[5] J.Kanamori, J.Phys. Chem Solids **10**, 87 (1959)

[6] P.W.Anderson, Solid State Phys. **14**, 99 (1963)

[7] K.Okada and A.Kotani, Phys. Rev. B **63**, 045103 (2001)

[8] K.Okada and A.Kotani, Phys. Rev. B **65**, 144530 (2002)

[9] Y.Mizuno, T.Tohyama, S.Maekawa, T.Osafune, N.Motoyama, H.Eisaki, S.Uchida, Phys. Rev. B **57**, 5326 (1998)

[10] D.Nardi, Thesis, università degli studi di Brescia, 2005/2006

[11] S.Pagliara, Ph.D. Thesis, università degli studi di Brescia, 1999

[12] V.Corradini, A.Goldoni, F.Parmigiani *et al*, Surface Science **420**, 142 (1999)

[13] S.Pagliara, F.Parmigiani, P.Galinetto, A.Recolevschi and G.Samoggia, Phys. Rev. B **66**, 024518 (2002)

[14] F.Bondino, M.Zangrando, M.Zacchigna, G.Dhalenne, A.Recolevschi and F.Parmigiani, Phys. Rev. B **75**, 195106 (2007)

[15] C.de Graaf, R.Broer, Phys. Rev. B **62**, 702 (2000)

[16] M.Bassi, P.Camagni, R.Rolli, G.Samoggia, F.Parmigiani, G.Dhalenne and A.Recolevschi, Phys. Rev. B **54**, 11030 (1996)

[17] H.Eskes, L.H.Tjeng and G.A.Sawatzky, Phys. Rev.B **41**, 288 (1990)

[18] Z.V.Popovic, S.Devic, V.N.Popov, G.Dahlenne and A.Revcoleschi, Phys. Rev. B **52**, 4185 (1995)

[19] S.Devic, M.Kostantinovic, Z.V.Popovic, G.Dahlenne and A.Revcoleschi, Cond. Matt. **6**, 745 (1994)

[20] A.Damascelli, D.van der Marel, G.Dahlenne and A.Revcoleschi, Phys. Rev. B **61**, 12063 (2000)

[21] S.Jandl, M.Poirier, M.Castonguay, P.Fronzes, J.L.Musfeldt, G.Dahlenne and A.Revcoleschi, Phys. Rev. B **54**, 7318 (1996)

[22] F.Parmigiani and L.Sangaletti, J. Of Electron Spectroscopy **107**, 49 (2000)

[23] M.Hase, I.Terasaki and K.Uchinokura, Phys. Rev. Lett. **70**, 3651 (1993)

[24] M.Hase, I.Terasaki and K.Uchinokura, Phys. Rev. B **48**, 9616 (1993)

Chapter 5

Experimental

Tthis chapter reports the description of the experimental set-up developed for the time-resolved optical measurements on copper germanate. Moreover, the mechanism for the white light's generation and the principles of its characterization are explained. Finally, the set-up characterization and the data acquisition procedure is presented and explained.

5.1 Charge transfer photo-excitation in $CuGeO_3$

As reported before (see chapter 4), two kinds of charge transfer processes are possible in $CuGeO_3$. However, only the CT in the Cu-O plane is related to the formation of the ZR singlet, while the charge transfer along the *b* axis does not create any bound state. From picture 4.4 [13], it is possible to deduce that the resonant energy, for these two processes, is quite different. Rather interesting is to note that the ZR excitation energy at ≈ 3.2eV, is quite close to the second harmonic of the fundamental of the Ti:Sapphire oscillator ($\hbar\omega \approx 3.2$eV). Moreover, being the *d-d* bands in the region of the visible light (≈ 1.7eV), they can be simply observed with

broad band white light pulses (i.e. with the supercontinuum). The set of these parameters and behaviours brings a scenario where $CuGeO_3$ is an ideal candidate to study, by pump-probe experiments, the dynamics of the electronic structure and the effects on the lattice dynamics induced by selective photo-excitations such as the CT photo-induced processes.

In addition, the CT process can be selected to be in the CuO_4 plane or along the apical direction of the CuO_6 distorted octahedron, by varying the polarization direction of the light (E//*c* or E//*b*). In fact it is quite intuitive that ZR states are a consequence of the CT process in the CuO_4 plane, and they cannot be excited when the incident electric field is oscillating along directions orthogonal to this plane, as pointed out by Pagliara *et al.* [13] (see fig. 5.1). Otherwise, a light polarized along the *c* axis does not induce any significant CT out of the CuO_4 plane.

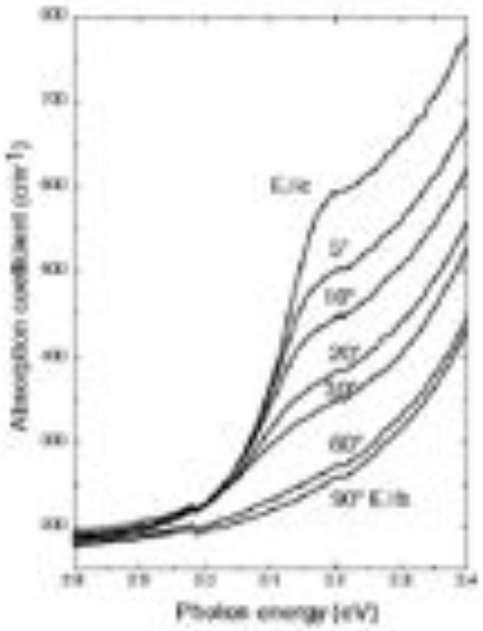


Fig 5.1: *Dependence of ZR formation from the light polarization in $CuGeO_3$* [13].

5.2 Pump-Probe Technique

The dynamics of the photo-excitation of the ZR singlet in copper germanate and its influences on the *d-d* forbidden transitions can be studied by the pump-probe optical spectroscopy. This technique consists in the splitting of a single ultra-short laser pulse into two distinct optical paths that will recombine on the sample. The first beam, the 'pump', is used to excite the sample and it is usually more intense than the other one. The second beam, the 'probe', is used to monitor the optical properties of the sample and their evolution at different delay times between the pump and the probe. The characteristic of this technique consists in the possibility of controlling, with an accuracy that no other experimental technique can reach[1], the delay between the pump and the probe, by means of sub-micrometer step motors.

The novelty of the experiment reported here consists in using the pump-probe setup with a supercontinuum (SC) probe pulse.[6] *This allows to observe all the frequencies in a selected spectral range at the same time, detecting the evolution of the system on a long time scale (up to the ns range) with a time resolution of few tens of fs.*

5.3 Laser System

The electromagnetic source for the experiment is a commercial laser system with a Ti:Sa oscillator and a regenerative amplifier. The oscillator is pumped by a Neodymium Vanadate ($Nd:YVO_4$) laser. The mode-locking of the modes allows the generation of femtosecond pulses with a band-width between 35 and 55 nm. These pulses are sent to a grating stretcher and amplified. The central wavelength can be tuned between ≈ 780 and ≈ 840 nm by adjusting a birifrangent filter (BRF) in the oscillator cavity.

[1] Nowadays the typical time response of the fastest acquisition electronic devices are of the order of 10^{-10} s, that is four or five orders of magnitude slower than the pump-probe resolution times.

Before entering into the regenerative cavity of the amplifier, the pulses are stretched to some tens of picoseconds, in order to avoid damages to the amplifier's crystal. The permanence time of the light pulses inside the cavity is controlled by two Pokel-cells in order to have the optimum number of round-trips inside the amplifier. Pulses are then compressed to ≈50-60 fs.

The delivered light pulses have the central wavelength at 795 nm, 1 kHz repetition rate, horizontal polarization, time width of ≈ 54 fs and average output power after the amplification of ≈ 2.4 W.

5.4 Pump-probe setup

In order to measure the shape and the temporal structure of the pulses, a few percents of the delivered laser power is sent into an autocorrelator. The rest of the beam is used for the experiment and it is split, by a beam splitter (BS), into a 10% intensity probe beam and the rest is left for the pump beam. The optical path is shown in picture 5.2.

The "pump" optical path consists of a telescope made up of a concave and a convex mirrors with radii r_1=601.2 mm and r_2=255.9 mm respectively. Then, the beam is sent through a second harmonic generation (SHG) crystal, a type-I BBO (Beta-BaB_2O_4) crystal, 0.05 mm thick and cut with an angle of ≈ 29°, that generates the second harmonic of the fundamental laser light with ≈ 5% efficiency, so that the excitation beam has a central wavelength of ≈ 400 nm. A 3 mm thick blue-band pass filter is used to quench out the fundamental frequency, while a half-wave plate and a polarizer are used to control the beam polarization. The pump beam is then focalized on the sample by a 25 mm focal length spherical mirror. This mirror is Al-coated to reflect and focalize both the pump and the supercontinuum probe beam. A delay time Δt between the pump and the probe beams is introduced using a delay stage based on a retro-reflector automatically controlled. Controlling the optical paths difference with a precision of ≈0.03 μm a time resolution of ≈ 0.1 fs can be achieved. The supercontinuum is generated focalizing the laser pulse on a 1 mm thick CaF_2 crystal. The crystal is oscillating at a frequency of 1.0 Hz to avoid laser damages.

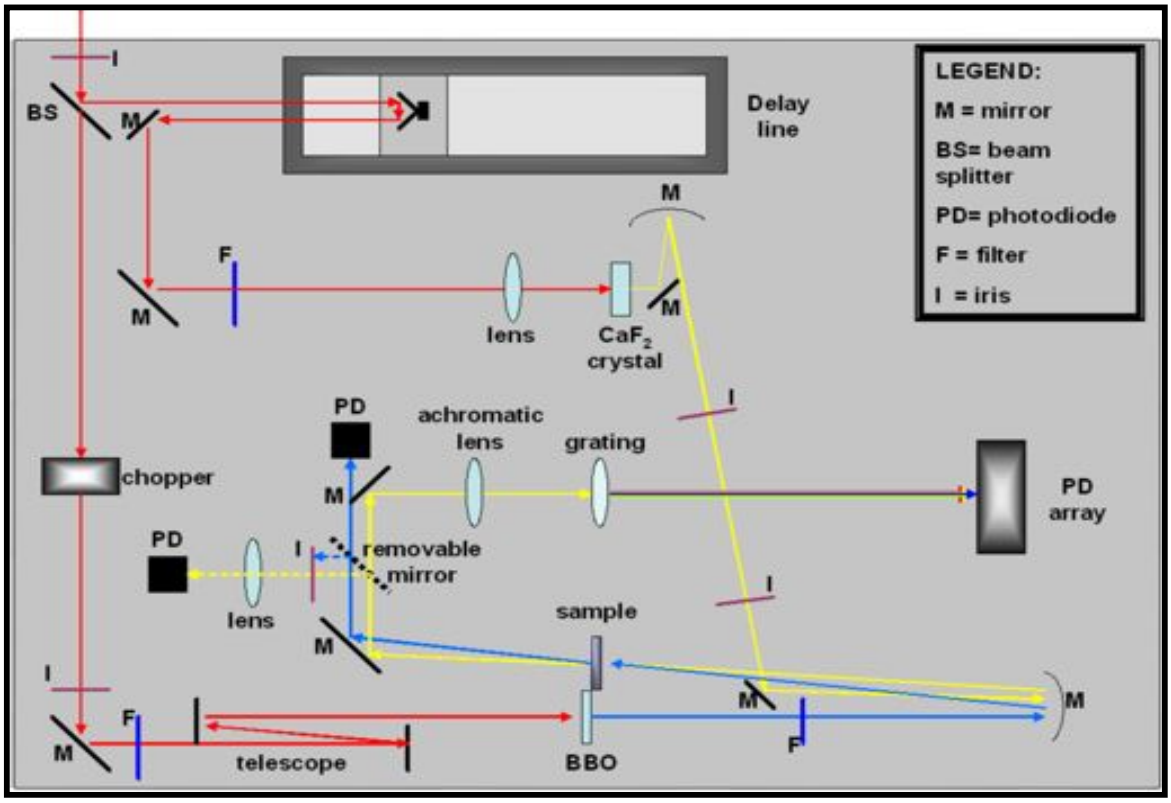


Fig 5.2: *Schematic representation of the experimental set-up.*

After the supercontinuum generation, a spherical mirror re-collimates the beam, which is then re-focalized on the sample by the same spherical mirror that focalizes also the pump beam. A flip-mirror is placed after the sample. When the mirror is "up", it reflects the probe beam towards a photodiode, connected to a lock-in amplifier. This configuration is used to perform two-colors pump-probe measurements. On the other hand, when the mirror is "down", the probe beam is sent through an achromatic lens and focalized on a photodiode array (DDA). Before reaching the diode array, the beam passes through a transmission grating, to disperse the light, while a reflection of the pump beam is detected by a single photodiode, to determine the parity of the pulse (i.e. if the signal received from the DDA is pumped or not).

5.5 Supercontinuum generation

When an intense ultra-short pulse is focused into a transparent medium, a white-light output pulse, ranging from infrared to ultraviolet is generated. This non-linear process, reported first by Alfano and Saphiro [3], is known as supercontinuum (SC) generation. The polarization of the SC is the same of the incident beam. The prominent mechanism leading to the spectral broadening is the self-phase modulation (SPM), and is a consequence of the intensity-dependent refractive index *n*, which, for the lowest order, can be written as

$$n = n_0 + n_2 I(t), \tag{5.1}$$

where n_0 is the time-independent part, while n_2 is the non-linear component of the refractive index, describing the strength of the coupling between the atoms and the electromagnetic wave. In the simple SPM theory, the pulse intensity does not vary with the propagation distance *z*, so the instantaneous frequency is Stokes shifted (i.e. redshifted) at the front of the pulse and Anti-Stokes shifted at the back of the pulse. The rigorous theory of SPM, developed in Ref. 12, yields to an asymmetrical spectral broadening of the pulse, that is larger for the Anti-Stokes component. However, recently Brodeur and Chin [11] have shown that the SC generation is intimately connected to the self-focusing mechanism, because the threshold powers of the two phenomena coincides, and the approximation of a strictly Kerr nonlinearity does not hold anymore. There exist a band-gap threshold for continuum generation, and the SC spectral width increases by increasing the material band-gap (i.e. by decreasing the Kerr nonlinear index n_2), in contrast with the theory of SPM in neutral mediums. The description of the process involves the generation of free electrons during the self-focusing. This limits the self-focusing since the presence of free electrons induces a negative change in the refraction index. There are two different processes for the generation of free-electron by a laser in condensed matter;

i) the avalanche ionization, where a seed electron is accelerated by the laser field until it has sufficient energy to excite into the conduction band another electron by collision;

ii) the multiphoton excitation (MPE).

However, for pulses of the order of 150 *fs* or less, only the second mechanism is relevant, since the first needs much more time to develop a significant electron density. While the front of the pulse travels in an almost neutral medium, the back of the pulse propagates through the free electrons generated by the front part. This causes a drop in the non-linear phase, due to the appearance of free electrons, sharper respect to the much more gradual increase present at the front of the pulse. Since the spectral broadening of the pulse depends on the rate of change of the nonlinear index, the process described translates into a large anti-Stokes tail and a much smaller Stokes broadening. Moreover, by increasing the energy gap, the intensity at which the self-focusing process stops becomes larger, while simultaneously the nonlinear accumulated phase, and consequently the spectral broadening, increase.

The simple mechanism illustrated above does not take into account the group velocity dispersion (GVD). The GVD can be understood observing that in every material the index of refraction depends non-linearly on the frequency of the incident pulse. For a wave travelling in a medium with refraction index $n(\omega)$, the phase variation between the different frequencies that travel in the medium for a length L can be developed as:

$$\Phi(\omega) = n(\omega)kL = k(\omega)L =$$

$$= k(\omega_0)L + \left.\frac{dk(\omega)}{d\omega}\right|_{\omega_0}(\omega-\omega_0)L + \frac{1}{2}\left.\frac{d^2k(\omega)}{d\omega^2}\right|_{\omega_0}(\omega-\omega_0)^2L + \ldots \qquad (5.2)$$

Remembering that the group velocity is defined as:

$$v_g \equiv \left(dk/d\omega\right)^{-1} \qquad (5.3)$$

the second term in (5.3) is bound to the group velocity in the material, while the third term contains

$$\left(\frac{d^2k(\omega)}{d\omega^2}\right)_{\omega_0} = \frac{d}{d\omega}\left(\frac{1}{v_g}\right) \qquad (5.4)$$

which can be recognized as the group velocity dispersion. It means that different frequencies of the pulse travel in the medium with different group velocities, resulting in a chirped pulse.

In conclusion, the supercontinuum generation is naturally accompanied by the chirping of the pulse, due to the interplay between the chirping effects of the SPM

and the GVD. This implies the necessity of measuring the resulting chirp of the SC, to correct the delay time for every frequency.

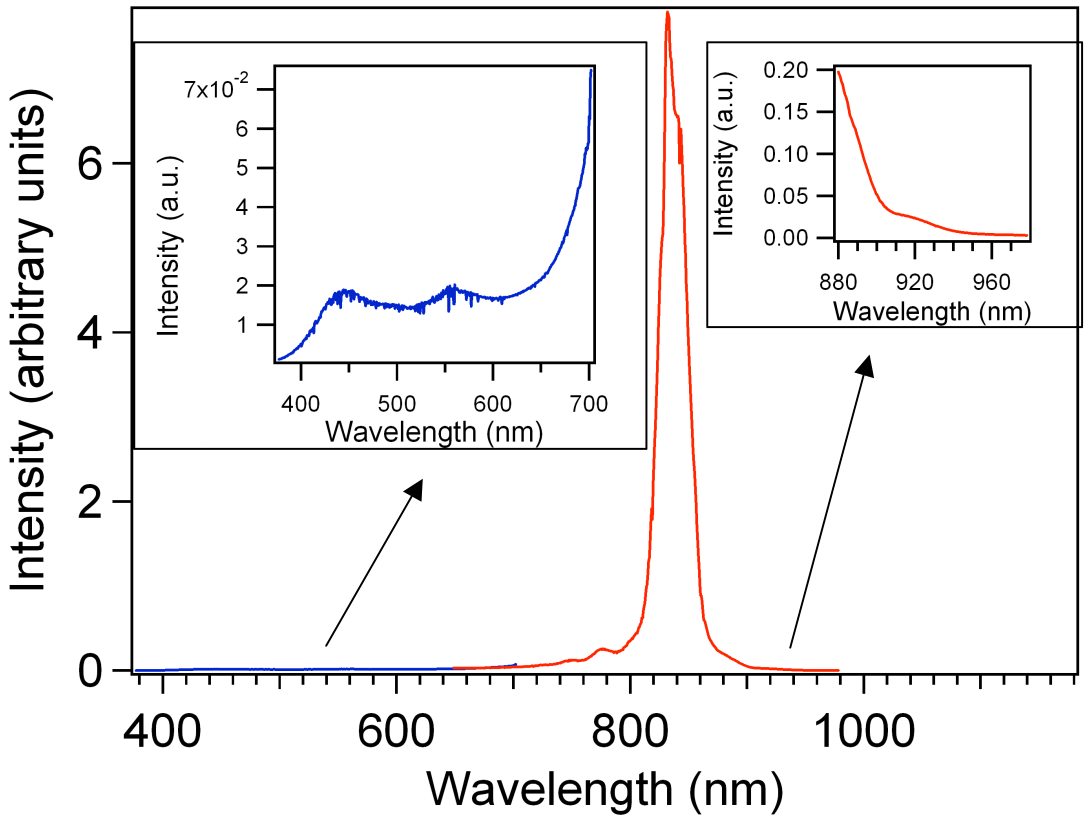


Fig 5.3: *Spectrum of the supercontinuum made with the CaF_2 crystal.*

5.6 Pump power

To investigate the effects of Zhang-Rice excitons it is necessary to impulsively illuminate the sample with a photon density enough to perturb significantly the dielectric function of the material and to probe a volume smaller or equal to the excited volume. Therefore, the dimension of the beams must be monitored by a beam-profiler CCD camera. The results are reported in fig. 5.4.

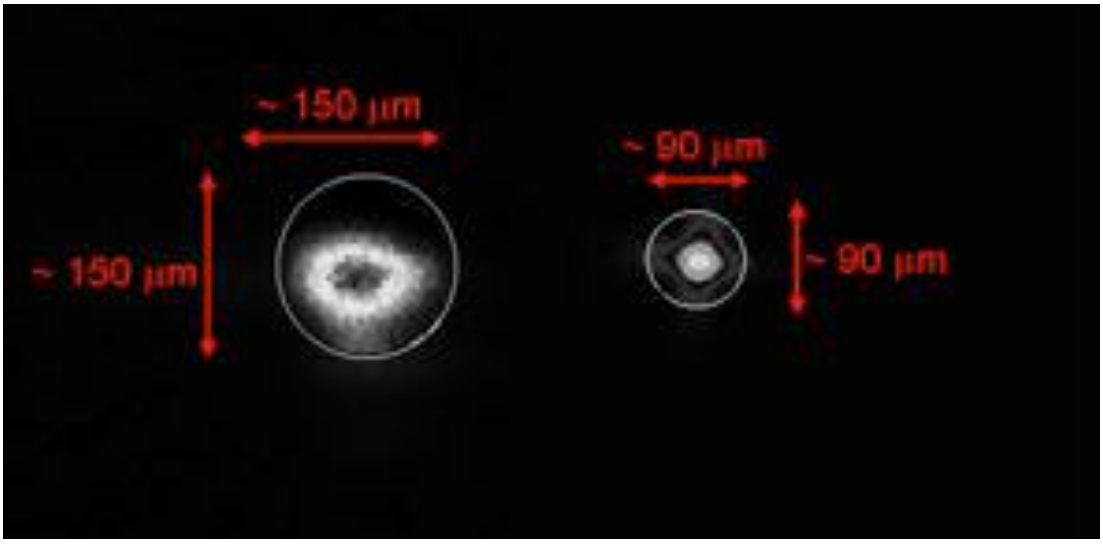


Fig 5.4: *Gaussian profiles of the pump (left) and probe (left) spots incident on the $CuGeO_3$ sample.*

Finally, some considerations about the excitation energy are needed. It has been shown by D. Nardi [10] that the copper germanate samples are fragile for fluences above $300mJ \cdot (cm^2 \cdot pulse)^{-1}$, that corresponds to a photo-doping percentage $n_{\%}$ greater than about 3.5%, as results from the following relation:

$$n_{\%} = EnergyDensity\left[\frac{J}{cm^2 \cdot pulse}\right] \cdot \frac{1}{PhotonEnergy[J]} \cdot \frac{\alpha}{n_{CuGeO_3}} \tag{5.5}$$

where n_{CuGeO_3} is the $CuGeO_3$ density, given by:

$$n_{CuGeO_3} = \frac{1[CrystalUnit]}{a \cdot b \cdot c[cm^3]} = 8.35 \cdot 10^{21}\left[\frac{CrystalUnit}{cm^3}\right] \tag{5.6}$$

This fragility manifests itself with an abrupt decrease in the transmittivity in the excited point. It has also been shown by Nardi [10] that at the energy of 1.57 *eV*, increasing the beam intensity up to the breaking limit, the absorption is linear and no other relevant features appear. This behaviour assures that during the pump-probe measurement there is no contribution due to a multiphoton absorption of the probe at the given energy. On the other hand, there is a non-linearity in the absorption of the pump above the $30mJ \cdot (cm^2 \cdot pulse)^{-1}$, as can be seen in fig. 5.5.

In the case presented in this thesis, the focus size of the pump beam has a radius of about $75\mu m$, while the integrated second harmonic power $\langle P \rangle$ after the chopper is about $4mW$. Consequently, the maximum fluence reached is:

$$Energy\,Density\left[\frac{mJ}{cm^2 \cdot pulse}\right] = \frac{\langle P \rangle [mW]}{rep.rate[s^{-1}]} \cdot \frac{1}{Area[cm^2]}$$

$$= \frac{4mW}{500Hz} \cdot \frac{1}{75^2 \cdot \pi \cdot 10^{-8} cm^2} \approx 45\left[\frac{mJ}{cm^2 \cdot pulse}\right] \qquad (5.7)$$

corresponding to a photo-doping percentage, given by (5.5)

$$n_{\%} = 0.045\left[\frac{J}{cm^2 \cdot pulse}\right] \cdot \frac{1}{3.12[eV] \cdot 1.6 \cdot 10^{-19}\left[\frac{J}{eV}\right]} \cdot \frac{500[cm^{-1}]}{8.35 \cdot 10^{21}[CU \cdot cm^{-2}]} \approx 0.55\% .$$

Even if this percentage may seem too small, it is sufficient to observe a meaningful variation in the transmission data.

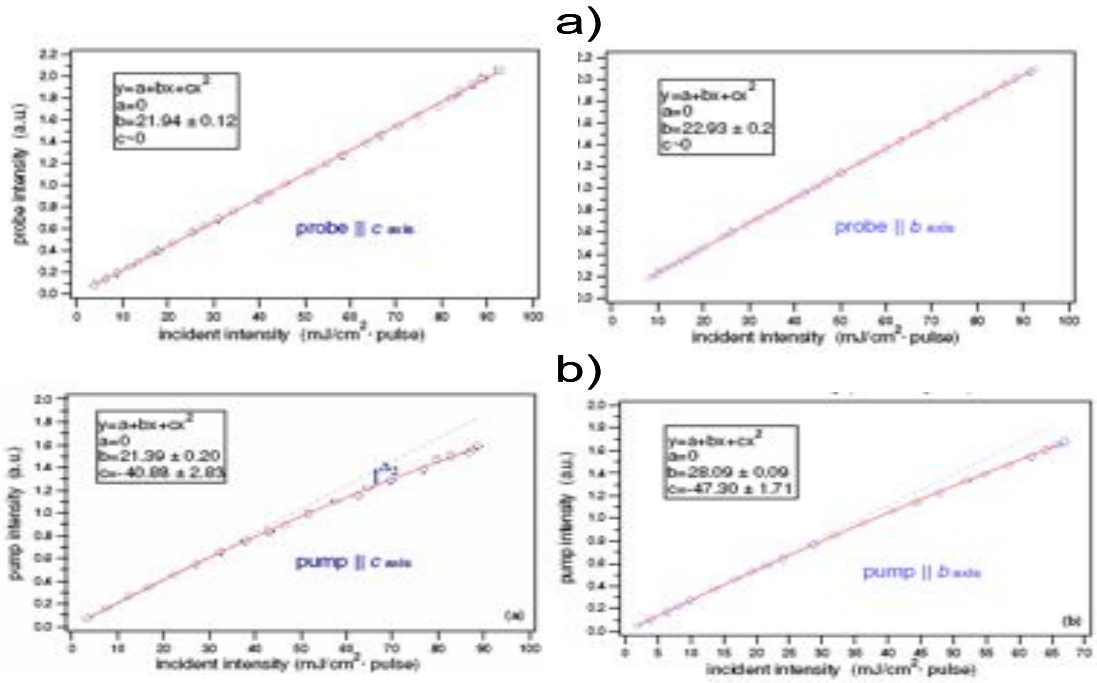


Fig 5.5: *$CuGeO_3$ absorption measurment* a) *at energy of 1.57eV (800nm) and* b) *at the pump energy of 3.14eV.*
Measures by Nardi [10]

It is important to note that the measurements are not in the ideal linear region for the pump. This suggests that a small fraction of the pump intensity is conveyed in a second order processes, and it will be necessary to discuss the influence of this non-linearity on the pump-probe measurements in the "results" section.

5.7 Data acquisition

The experiment and the data acquisition have been achieved by an ad-hoc designed software, beside the three times splitted 1 kHz trigger signal from the amplifier which delay is controlled by a different software program. The first reference signal is used as a trigger for the auto-correlator, the second one, reduced to 500 Hz, is used as the reference signal for the lock-in amplifier and the chopper, while the last one is the input signal for the data acquisition program. This program can control two photodiode arrays, a single photodiode, a linear delay motor and a lock-in amplifier and it can be used in two different modalities, according to whether a two-color pump-probe measure or a scan with the DDA is done.

For the first type of measurement, a single photodiode connected with a lock-in has been used, in order to optimize the signal-to-noise ratio. The pump beam is chopped at 500 Hz before exciting the sample, and the delay generator, triggered with the 1kHz frequency from the laser amplifier, controls that the 500 Hz square wave is maintained at a fixed delay with respect to the laser beam, so that a pulse every two is stopped. By doing so, the lock-in amplifier signal gives the intensity of the probe when the excitation has been induced (pumped signal) minus the intensity of the probe without the pump (un-pumped signal), because the modulation at 500 Hz, that it detects, is between the pumped and the un-pumped signals. Clearly this type of measurement is not absolute and requires to be divided by the total transmittivity of the un-pumped sample to obtain the percentage of the variation.

The second type of measurement is more complete, because the DDA, put after the grating and in the focus of the achromatic lens, can detect all the frequencies at the same time and it can mediate the signal over an user-selected number of laser shots. In this case, however, it is first necessary to acquire the background and the

reference signal, without the sample. Secondarily a new background is acquired, to take into account the reflections generated by the pump passing through the sample and superimposed to the white-light signal. An external photodiode detects the signal from the pump and establishes the parity, in order to distinguish the pumped signals from the un-pumped ones. At the end, the observed signal *S* is analyzed by the program and the output is the difference in transmission over the transmission un-pumped:

$$S = \frac{\Delta T}{T_{unpump}} = \frac{T_{pump} - T_{unpump}}{T_{unpump}} = \frac{I_{pump}}{I_{pump}(ref)} \cdot \frac{I_{unpump}(ref)}{I_{unpump}} - 1 \qquad (5.8)$$

In the scanning mode, the motor moves for a selectable number of steps of few femtoseconds, and between two subsequent steps the lock-in amplifier or the DDA acquires the intensity of the signal.

5.8 Data treatment and setup characterization

The main steps for the data analysis are the followings:

a. Time-zero function determination: as already seen in 5.5, one of the major problems in using the supercontinuum as a probe is its intrinsic chirp. Consequently different components of the probe spectrum enter the sample at different times for any specific setting of the optical delay between the pump and probe beams. Hence, to extract the real time evolution for every frequency, it is necessary to have a precise time-correction function. Recent studies [6-8] have demonstrated that the time-correction needed for this aim can be obtained using a material whose response to a perturbation is purely electronic. In our case, a fused silica window 1mm thick has been used, as it was done by Kovalenko *et al*.[8]. The measurement is shown in fig. 5.6.

Since the pulses recombine in a fused silica window, in principle they pass through a piece of material for a distance *d*, $0<d<1$mm. The overall effects of this passage are a rigid translation of the position of the time-zero points

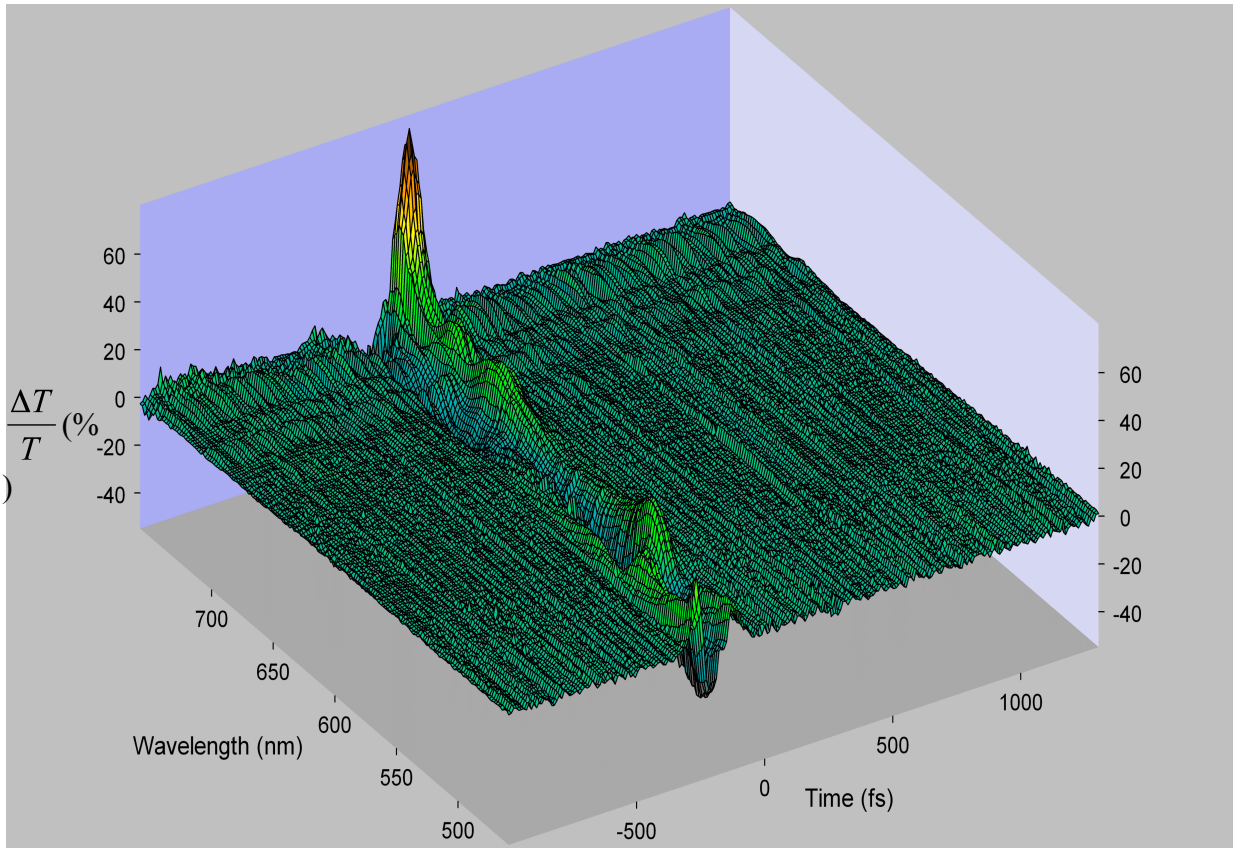


Fig.5.6: *Fused silica electronic response in the spectral range between 460 and 750 nm*

and an extra chirp induced by the medium, that can be calculated using the Sellmeier empirical relationship:

$$n^2(\lambda) = 1 + \frac{B_1\lambda^2}{\lambda^2 - C_1} + \frac{B_2\lambda^2}{\lambda^2 - C_2} + \frac{B_3\lambda^2}{\lambda^2 - C_3} \tag{5.9}$$

where the coefficients B_i and C_i are known and tabulated in literature. Since the group velocity is given by

$$v_g(\lambda) = \frac{c}{n(\lambda) - \lambda \cdot \frac{\partial n}{\partial \lambda}}, \tag{5.10}$$

to obtain the difference in the time-zero position due to the travel through fused silica is sufficient to calculate

$$\Delta t(\lambda) = \frac{d}{c - v_g(\lambda)} \tag{5.11}$$

Therefore the estimation of the distance, *d*, covered in the fused silica before the recombination of the pulses is needed. If the time zero is fixed on the maximum of the cross-correlation curve and a scan in the red part of the spectrum is taken, the difference in time at 800 nm, of about 140 fs, corresponds to the difference between a red and a blue pulse when they travel $d \approx 0.9$ mm in fused silica. In this way, the time-zero function for the SC pulse can be simply obtained by subtracting, from the function that fits the curve measured on fused silica, the function (5.11) for the calculated distance *d*.

b. Pulses time-width determination: for this purpose the cross-correlation function between the pump and the probe pulses has been measured. The laser system is provided with an auto-correlator, placed at the exit of the amplifier. However, this instrument can measure only the time duration of the pulses produced by the laser system, while for a precise characterization of the experimental set-up the exact duration of the pulses when the pump and the probe recombine in the sample is needed. Typically, there is a lengthening of the pulses, due to the optical path that they travel into mediums, as lens, beam-splitters, filters and crystals, before reaching the sample. Moreover, since the optical paths for the pump and the probe are different, it can result in different duration of the pulses. For all these reasons it is better to measure the cross-correlation function instead of the simple autocorrelation. Finally, the cross-correlation function gives important information about the degree of focalization and about the eventual aberrations introduced by the optical components.

The cross-correlation function has been measured using the third harmonic of the Ti:Sa laser, generated in a type-I BBO crystal, 0.1 mm thick, cut at an angle of 44.5°, placed in the sample position. Since the third harmonic is produced only when the second harmonic (pump) and the fundamental (probe) overlap in space and time in the non-linear crystal, a scan of this

signal, detected by a photodiode, as a function of the delay between the two beams, permits to obtain a background-free intensity cross-correlation function of the frequency-sum generation, which is exactly a measure of the temporal shape of the longer of the two pulses. A profile of the cross-correlation function obtained is shown in fig. 5.7; from the FWHM it is possible to estimate a pulse time-width of about 86 fs.

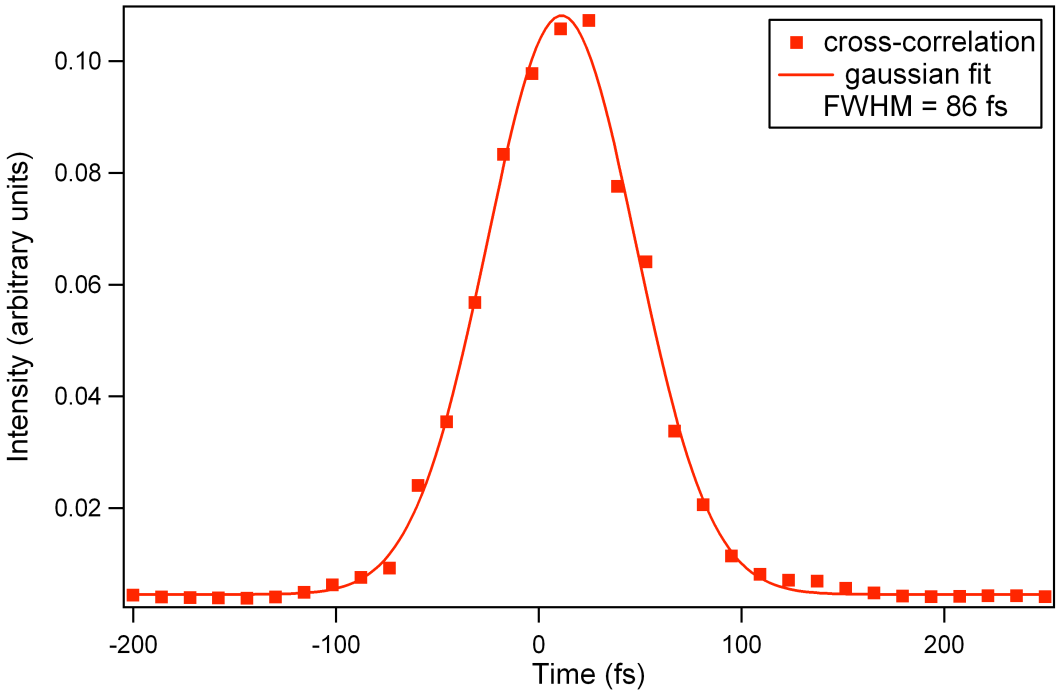


Fig 5.7: *Cross-correlation function obtained from the measurement of the third harmonic. The gaussian fit is displayed and the FWHM is of about 86 fs.*

c. Spectral response correction: generally, each photodiode has a different response to the different frequencies it can detect, that, in principle, have to be taken into account in the data analysis. However, this behaviour does not influence the data of this kind of experiment, since the measured spectrum S_{exp} is given by:

$$S_{exp}(\lambda) = R(\lambda) \cdot S_0(\lambda) \qquad (5.12)$$

where $S_0(\lambda)$ is the real spectrum and $R(\lambda)$ is the spectral response function. In this way, when the transmittivity T is calculated

$$T = \frac{S_{\exp}(with_sample)}{S_{\exp}(without_sample)} \tag{5.13}$$

the spectral response function is cancelled and it does not enter in the data analysis.

d. Spectral calibration and spectral resolution: to determine the frequencies detected by each pixel of the photodiode array, it is necessary to find a proper calibration. In particular, since the DDA is placed in the focal position on a vertical linear translator, provided of micrometric movement, the calibration equation has to contain also the height parameter, that is the number read on the micrometer. To calibrate the system, a crystal of $YAlO_3$ has been used, whose reference spectrum, taken with a continuous lamp, is known. The results are shown in fig. 5.8. In the static spectra taken with the supercontinuum pulses, the structures at 446.7 nm and 539 nm are well defined. Since the width of these features is about 3 nm, the spectral resolution of the system is better than 3 nm. The presence of two different curves is due to the fact that it is not possible to acquire all the wavelengths from 400nm to 900nm in a single spectrum keeping the same spectral resolution. It has to be noticed that the two curves superimpose perfectly.

Once the supercontinuum spectra have been taken, the main structures peaks have been used to construct the function that gives the wavelength as a function of the DDA pixel N_p and the micrometer position *h*:

$$\lambda(N_p, h) = a_1 + b_1 \cdot N_p + a_2 + b_2 \cdot h\,. \tag{5.14}$$

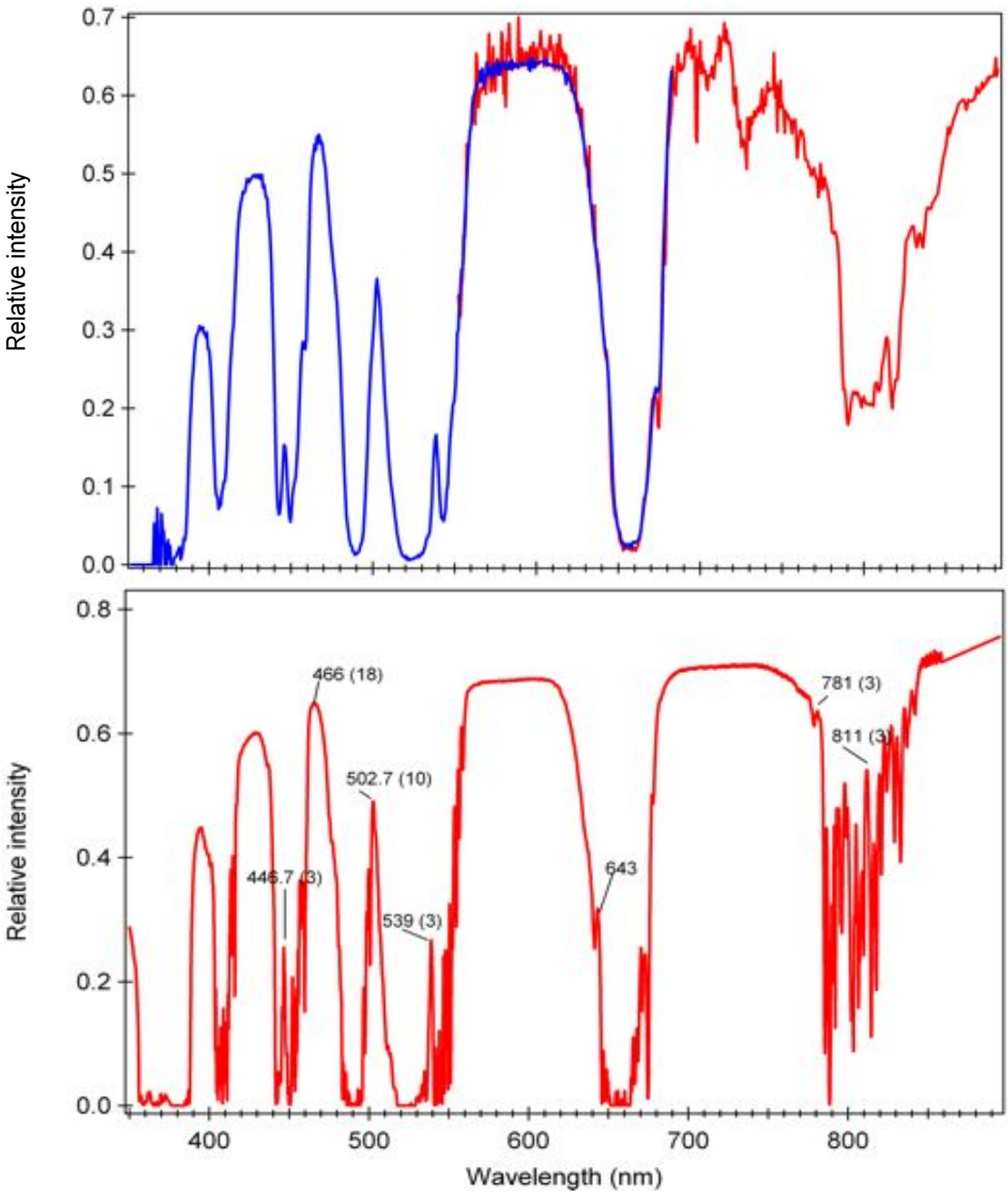


Fig 5.8: A*bove, the static spectrum taken with the supercontinuum pulses; below, the calibration spectrum of* $YAlO_3$ *taken with a lamp.*

Bibliography:

[1] Operator's manuals for VERDI and MIRA, Coherent laser division

[2] Legend user manual, Coherent laser division

[3] R.R.Alfano and S.L.Saphiro, Phys. Rev. Lett. **24**, 592 (1970)

[4] J.C.Diels and W.Rudolph, *Ultrashort Laser Pulse Phenomena,* Academic Press (2006)

[5] A.E.Siegman, *Lasers,* University Science Books, Sausalito (California) (1986)

[6] S.A.Kovalenko, N.P.Ernsting, J.Ruthmann, Chem. Phys. Lett. **258**, 445 (1996)

[7] C.Nagura, A.Suda, H.Kawano, M.Obara, K.Midorikawa, Applied Optics **41**, 3735 (2002)

[8] S.A.Kovalenko, A.L.Dobryakov, J.Ruthmann and N.P.Ernsting, Phys. Rev. A **59**, 2369 (1999)

[9] S.Pagliara, Ph.D Thesis, Università degli studi di Brescia (1999)

[10] D.Nardi, Thesis, università degli studi di Brescia, 2005/2006

[11] A.Brodeur and S.L.Chin, J. Opt. Soc. Am. B **16**, 637 (1999)

[12] G.Y.Yang and Y.R.Shen, Opt. Lett. **9**, 510 (1984)

[13] S.Pagliara, F.Parmigiani, P.Galinetto, A.Recolevschi and G.Samoggia, Phys. Rev.B **66**, 024518 (2002)

Chapter 6

Data analysis techniques

In this chapter, the techniques used to analyze the data are discussed. The first section is devoted to the explanation of the Singular Value Decomposition (SVD) and the Decay Associated Spectra (DAS) methods, while in the second part Fast Fourier Transform method is reported.

6.1 Singular Value Decomposition technique

Data taken with the photodiode array are made of matrices of intensity values, given in function of the wavelength and the delay time between the pump and the probe pulses. Since the sample is subjected to two impulsive (pump and probe) effects, it is necessary to subtract the effect of the probe pulse alone on the ground state of the system. For this reason the relative transmission

$$\frac{\Delta T}{T} \equiv \frac{T_{pumped} - T_{unpumped}}{T_{unpumped}} \tag{6.1}$$

has been considered. In practice, the measured signal is the opposite of the optical

density of the system, which is proportional do the relative transmittivity through the relation:

$$-\Delta OD = \frac{1}{\ln 10} \cdot \frac{\Delta T}{T}. \tag{6.2}$$

To treat the large quantity of data in every matrix, the Singular Value Decomposition (SVD) method has been applied. This is a very general method, since it can be applied to any $m \times n$ matrix and it is related to the eigenvalue decomposition, even if the last can only be applied to certain classes of square matrices, i.e.invertible and if and only if the algebraic and geometric multiplicities coincide for all the eigenvalues. However, in the special case that the matrix considered $\underline{\underline{\Psi}}$ is Hermitian and positive semi-definite (i.e. all its eigenvalues are real and non-negative), the singular values and singular vectors coincide with the eigenvalues and eigenvectors of $\underline{\underline{\Psi}}$.

SVD is a very powerful procedure, with some limits, represented by the preliminary assumptions that the noise is additive and the bands do not change their energy and their form in time. In this case, the matrix $\underline{\underline{\Psi}}$ of dimensions $m \times n$, where m and n are, respectively, the number of different time instants and wavelengths, can be written as:

$$\underline{\underline{\Psi}}_{t_i \lambda_j} = \sum_{l=1}^{n_{components}} c_{l t_i} \varepsilon_{l \lambda_j} + \underline{\underline{\Xi}}_{t_i \lambda_j} \tag{6.3}$$

where $c_{l t_i}$ and $\varepsilon_{l \lambda_j}$ denote respectively the population and the spectrum of the component l and the matrix $\underline{\underline{\Xi}}$ represents the noise, assumed as normally stochastic distributed. Known the population and spectral terms, is quite simple to reconstruct the matrix $\underline{\underline{\Psi}}$. However, the experimental measure of $\underline{\underline{\Psi}}$ poses the inverse problem, and it is necessary to reconstruct the kinetic properties of the spectral components present in the system, which are generally unknown.

To resolve the problem, it is necessary to find a way to determine how many and which are the components that describe the system, and then what is their dynamic behaviour.

A matrix $m \times n$ on a field K can always been factorized in a form

$$\left(\underline{\underline{\Psi}}(t,\lambda)\right)_{m\times n} = \left(\underline{\underline{S}}(t)\right)_{m\times m} \times \left(\underline{\underline{W}}\right)_{m\times n} \times \left(\underline{\underline{T}}(\lambda)\right)^{T}_{n\times n} \tag{6.4}$$

where $\underline{\underline{S}}(\lambda)$ and $\underline{\underline{T}}(t)$ are orthogonal unitary matrices, whose columns contain respectively the so called "eigen-spectra" and the "eigen-traces" associated to the matrix $\underline{\underline{\Psi}}(t,\lambda)$, while $\underline{\underline{W}}$ is a matrix which is zero except for its diagonal, that contains the singular values. It is common convention to order the values W_{ij} in non-increasing fashion. With $n_c = n_{components}$ components and noise-free data, the matrix $\underline{\underline{\Psi}}$ has exactly n_c significant singular values $s_1 \geq s_2 \geq ... \geq s_{n_c} > 0$. The presence of the noise perturbs the noise-free SVD changing the singular values and perturbing the singular vectors of the $\underline{\underline{S}}(\lambda)$ and $\underline{\underline{T}}(t)$ matrices. The perturbation is given by the largest singular value of $\underline{\underline{\Xi}}$, say $s_1^{(\Xi)}$. It has bee shown that the perturbation is negligible when $s_l - s_{l+1} >> s_1^{\Xi}$, while when $s_l - s_{l+1} \approx s_1^{\Xi}$ the noise can greatly alter the singular vectors. In practice, since in most cases the matrix $\underline{\underline{\Xi}}$ is unknown, to find out the number n_{rel} of significative components, i.e. the number of singular values significatively different from noise, one has to consider the singular values of $\underline{\underline{W}}$ in the decomposition 5.4. Since the effect of the noise is already included in this decomposition, the rule to follow requires to take into account all the singular value until they start to form an almost continue line, where the difference between s_l and s_{l+1} is very small, as stated in ref. [1].

So far, only the number of the relevant singular values has been determined. To proceed is necessary to introduce another assumption on the temporal behaviour of the relevant components. In case the population of the states can be described by linear differential equations, the solution is a sum of exponential decays; so the first step consists in fitting the only relevant "eigen-traces" with a sufficient number of exponential decays and the associated amplitudes, with the idea that each individual exponential represents a single state or process. This procedure is known as Decay Associated Spectra (DAS). It has to been noticed that, so far, nor the "eigen-traces" neither the "eigen-spectra" have any physical meaning. The global fit of the relevant "eigen-traces", multiplied by their relevant singular value, permits to find the decay times associated to the process. In this way, each trace *k* is represented as:

$$T_k(t) = \sum_{l=1}^{N} a_{lk} \cdot \exp\left(-\frac{t - t_0}{\tau_l}\right). \tag{6.5}$$

where N is the number of the time decay necessary to fit the curves and t_0 the time at which the process begins. At this point, if the product between the matrix of the relevant "eigen-spectra" and the transpose of the matrix of the coefficients a_{lk} is implemented, the result is a rotation in the space of the relevant singular vectors. The resultant matrix is made of n_{rel} spectra Σ_i, each one associated to the decay time τ_i.

In this way, the kinetic behaviour of the spectral features is pointed out: the different spectral features that compose the spectrum are more evident, because they are no more convoluted one with each other, and also the dynamics of different processes is more clear. Finally, the SVD is the ideal tool to check for structured residuals: through the analysis of the residual is possible to identify the presence of oscillations, with an initial fixed period, that corresponds to the excitation of lattice phonons.

So far the real width of the pulses has not be taken into account. However, in a pump probe experiment the true temporal behaviour of the process is not directly accessible, because what can be measured experimentally is only the convolution between the true kinetics of the process and a response function that describes the pump and probe apparatus. If the pulses would be a true delta functions, the true kinetic traces would be the product between an exponential decay and the step function $\theta(t)$, because there can't be excitation before the arrive of the pump pulse (at time $t_0 = 0$). However, the spectra obtained experimentally are the convolution between the true kinetic response of the system and the cross-correlation function of the two pulses.

The pulse shape *I*(*t*) is considered to be Gaussian:

$$I(t) = \exp\left\{-\left(\frac{t}{\sigma_G}\right)^2\right\} \tag{6.6}$$

where σ_G is related to the pulse duration τ_P, that is the FWHM of the Gaussian, by:

$$\tau_P = 2\sqrt{\ln 2} \cdot \sigma_G. \tag{6.7}$$

The cross-correlation function of two pulses is their convolution; in case of two Gaussian pulses of σ_{G1} and σ_{G2}, the cross correlation function results to be a new Gaussian, with parameter σ_{cc} given by

$$\sigma_{cc}^2 = \sigma_{G1}^2 + \sigma_{G2}^2 \tag{6.8}$$

as follows from the convolution formula:

$$C(t) = \int_{-\infty}^{+\infty} I_1(t') I_2(t'-t) dt' = \int_{-\infty}^{+\infty} \exp\left\{-\left(\frac{t'}{\sigma_{G1}}\right)^2\right\} \exp\left\{-\left(\frac{t'-t}{\sigma_{G2}}\right)^2\right\} dt'$$

$$= \sqrt{\pi\left(\frac{1}{\sigma_{G1}^2} + \frac{1}{\sigma_{G2}^2}\right)} \cdot \exp\left\{-\left(\frac{t^2}{\sigma_{G1}^2 + \sigma_{G2}^2}\right)\right\} \tag{6.9}$$

With this considerations, 6.5 becomes:

$$T_k(t) = \sum_{l=1}^{N} a_{lk} \cdot \exp\left(-\frac{t - t_0}{\tau_l}\right) \cdot \exp\left\{\frac{\tau_{cc}}{2\tau_l}\right\}^2 \cdot erfc\left\{\frac{t - t_0}{\tau_{cc}} - \frac{\tau_{cc}}{2\tau_l}\right\} \tag{6.10}$$

where τ_{cc} is the width of the cross-correlation. The algorithm used can estimate all the pre-exponential coefficient, the decay times, τ_{cc} and t_0. Especially, the estimate of τ_{cc} is of about 80 fs.

6.2 Fast Fourier Transform

To individuate the frequencies involved in oscillating processes, one has to perform the Fourier Transform (FT) of the time dependent spectra. The continuous FT is defined as:

$$f(\omega) = F_T[f(t)](\omega) = \int_{-\infty}^{+\infty} f(t) e^{-2i\pi\omega t} dt \tag{6.11}$$

However, since the experimental data are finite-domain time-discrete signals, the appropriate algorithm is the Discrete Fourier Transform (DFT): it is a generalization of 6.11 to the case of a discrete and finite input function $f(t_k)$, with k = 0, 1,..., N-1. The discrete Fourier Transform is given by

$$F_n = \sum_{k=0}^{N-1} f_k e^{-2i\pi\frac{k}{N}n} \tag{6.12}$$

Discrete Fourier transforms are extremely useful because they reveal periodicities in input data as well as the relative strengths of any periodic components.

However, in practice, computing the DFT requires N complex products and N sums for each component F_n. Since in any computer the multiplication requires a much larger time than a sum, neglecting the time spent for the sums, the calculation of the N values of the DFT requires $O(N^2)$ operations. The Fast Fourier Transform is an efficient algorithm to compute the DFT of an input discrete function reducing the number of arithmetical operations to $O(N \ln N)$.

To implement the FFT, the multidimensional prime factor decomposition algorithm of IGOR pro 5.05 has been used. This algorithm is based on prime number decomposition, which decomposes the number of points in each dimension of the wave into a product of prime numbers, and it is optimized for primes < 5. The algorithm can work only with an even number N >4. The result of the FFT operation is always a floating point number (single or double precision, depending on the input wave points' precision). The errors due to the finite-precision of the computer are typically quite small; most FFT algorithms have an upper bound on the relative error spacing from $O(\varepsilon\sqrt{\log N})$ to $O(\varepsilon\sqrt{N})$, where ε is the machine floating-point relative precision.

Bibliography:

[1] G.H.Golub, C.F. van Loan, *Matrix Computation,* Johns Hopkins University Press, Baltimore (1996)

[2] I.H.M.Van Stokkum, D.S.Larsen and R. van Grondelle, Biochim. Biophys. Acta 1657, 82-104.v (2004)

[3] J.Kauppinen, J.Partanen, *Fourier Transforms in Spectroscopy,* Wiley (2001)

[4] A.D. Poularikas, *The transforms Handbook,* CRC Press (1999)

Chapter 7

Results

In this chapter the mainfold experimental data and results are presented and analyzed.

7.1 Matrices of data

The data taken with the photodiode array are made of matrices of the relative transmission values, given in function of the wavelength and the delay time between the pump and the probe pulses. The measured signal $-\Delta OD$ is the opposite of the optical density of the system, which is proportional do the relative transmittivity through the relation (6.2).

As an example, one of the matrices is presented using a surface plot and an image plot (Fig. 7.1a) and b)). The copper germanate responds to the excitation pulse with an instantaneous rise of the absorption respect to the stationary case, i.e. it rises with a lifetime ($\tau < 50$ fs) too fast to be resolved with our 80 fs laser pulses. Around t = 0, the absorption reaches its maximum value, which is wavelength dependent. After the excitation, the system starts a very fast relaxation, of the order

of several hundred of fs, followed by a much slower decay process that extends for up to hundreds of picoseconds. In particular, it is important to point out that, after about 1.3 ps, a modulation of the transmittivity appears for $\lambda < 680$ nm, as shown in fig. 7.1b).

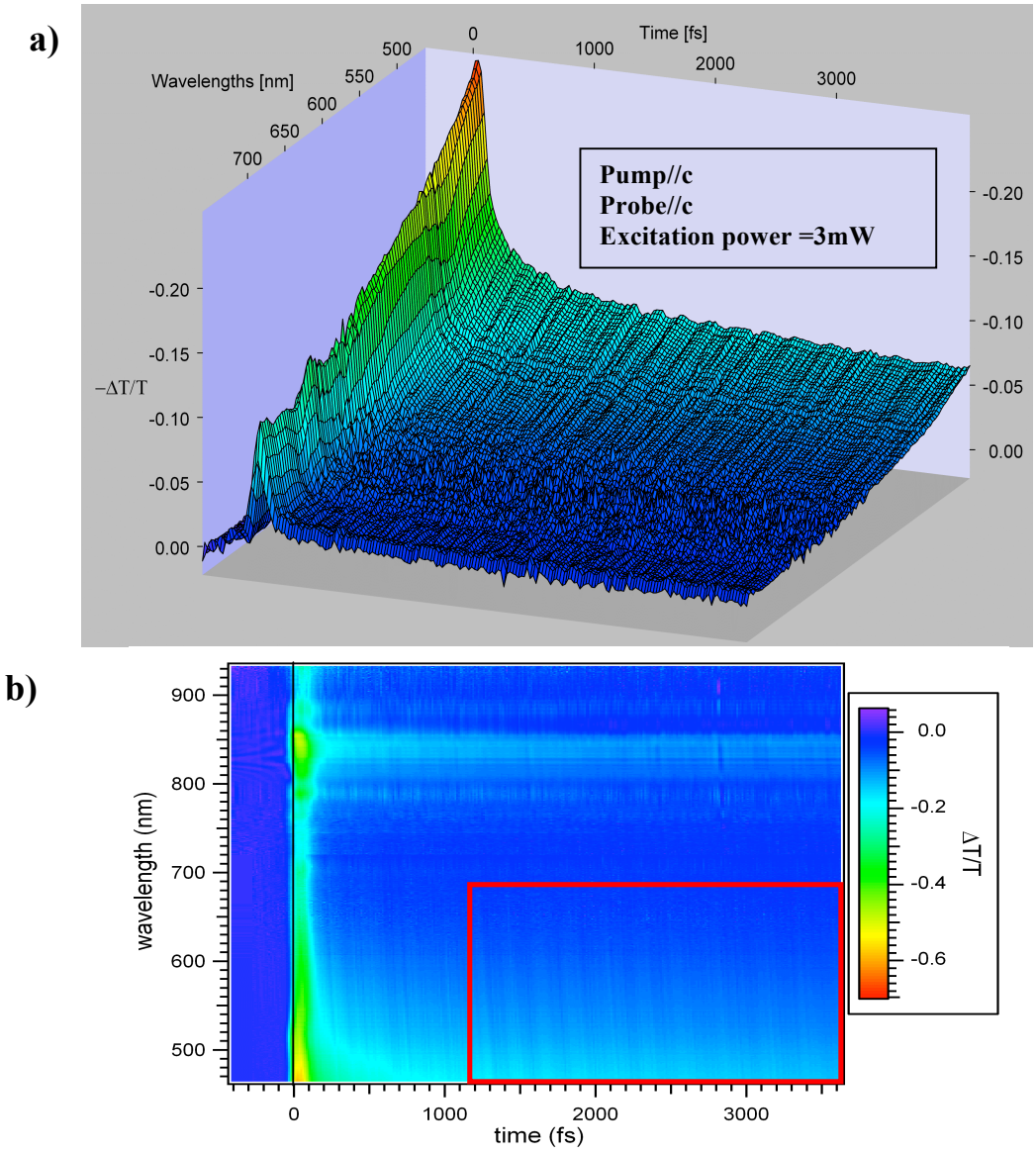


Fig. 7.1: a) *Surface plot of one matrix of data, taken with pump power of 3 mW.* b) *Image plot of two merged matrices that covers almost all the visible wavelength range. The red box marks the region where periodic modulations of the transmittivity are more evident.*

7.2 Time dynamics of the relaxation processes

The dynamics of the transmittivity relaxation can be obtained from the deconvolution of the kinetic traces, which is done by fitting a trace at a certain wavelength with a function that is a convolution between a Gaussian, a step function and a sufficient number of exponential decays. In particular, the deconvolution has been done on traces at different frequencies for a short time delay scan (until 4 ps), a longer one (until 18 ps) and a very long one (until 860 ps). In this way both the fast and slow dynamics extending in the range of hundreds of ps are well resolved. The main points that turn out from the fit are:

1. There are at least 6 relaxation time scales involved in the total dynamics. Ultrafast (τ < 100 fs), intermediate (100 fs < τ < 2 ps) and slow (τ > 2 ps) dynamics are present for all kinetic traces. The fitting procedure repetition on the SVD "eigen-traces" has allowed the separation of two ultrafast decay processes.
2. The six decay time constants obtained from the fits are:
   - ◊ τ_1 < 15 fs
   - ◊ 60 fs < τ_2 < 80 fs
   - ◊ 500 fs < τ_3 < 600 fs (450 – 650 nm) or
     1.2 ps < τ_3 < 1.3 ps (650 – 850 nm)
   - ◊ $\tau_4 \approx$ 8.3 ps
   - ◊ $\tau_5 \approx$ 60 ps
   - ◊ $\tau_6 >$ 1.9 ns

Since in order to obtain a reliable value for the time constant τ of an exponential decay a time-window greater than 3τ is needed, the value of τ_6 is only indicative for a relaxation dynamic much slower than the time-scale accessible with our experimental set-up.

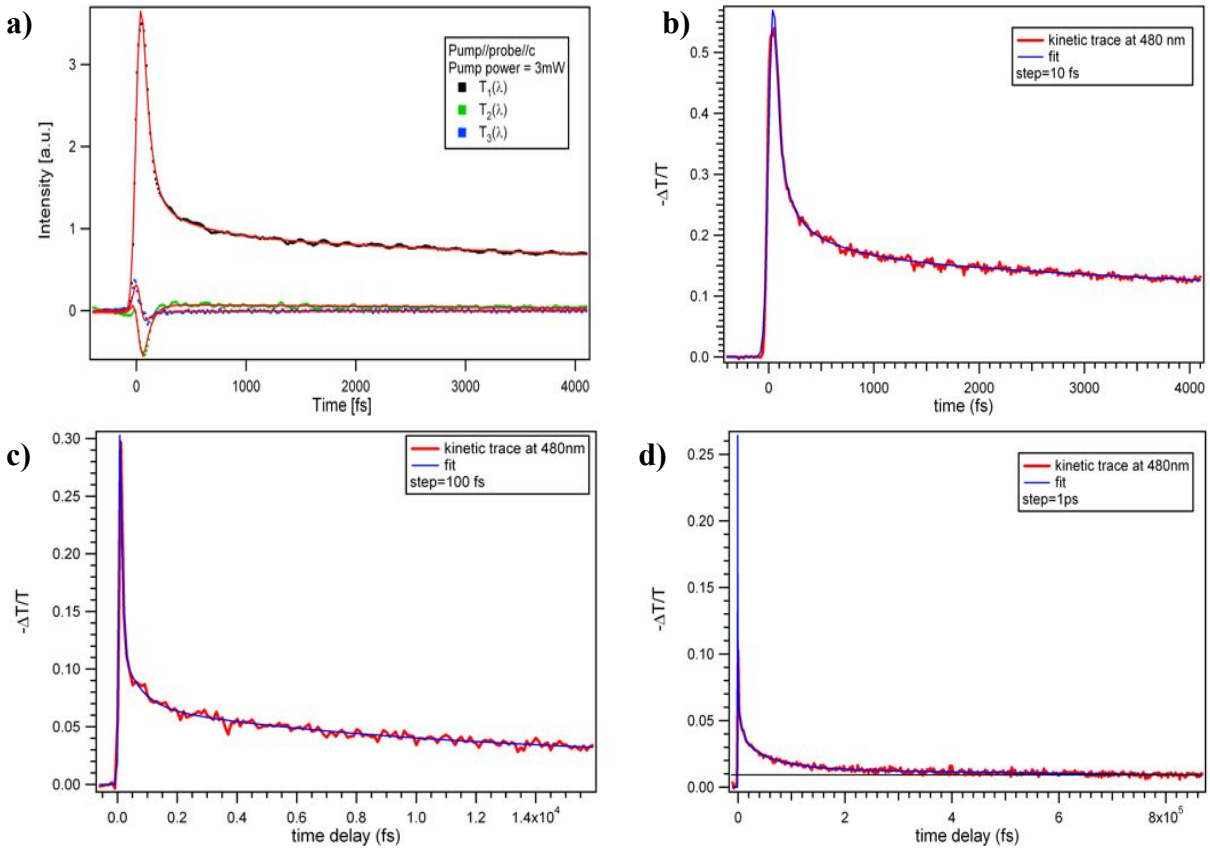


Fig. 7.2: a) *SVD "eigen-traces".* b),c) *and* d) *Kinetic traces at 480 nm, taken with pump power of ≈3 mW. Each trace is fitted with the convolution of a Gaussian with 5 exponential decays, since the time interval measured and the time step does not permit to distinguish all the 6 dynamics in the same trace. The long time constants obtained from* d) *were consequently used as fixed parameters in the fit of the traces* a), b) *and* c). *The horizontal line in* d) *demonstrates that the system does not completely relax even at t = 860 ps.*

7.3 Dependence of transmittivity on the pump fluence

For the pump//probe//*c* configuration, a series of measurements varying the pump incident power has been performed. Photon densities varies from $0.10 \cdot 10^{20}$ to $0.34 \cdot 10^{20}$ photons/(cm^3· pulse), i.e. the photo-doping varies from 0.12% to 0.41%.

First of all, the linearity of the transmittivity variation with pump fluence has been checked for various wavelengths, both for fast (t = 0), intermediate (t = 600 fs for $\lambda < 650$ and t = 1200 fs for $\lambda > 650$) and slow relaxations (t = 2.5 ps), as it is shown in fig. 7.3. The transmission increases linearly with the incident pump intensity. This proofs that non-linear absorption processes are not significant at the observed energies and the variation of the detected transmittivity is directly related to the photo-excitation density.

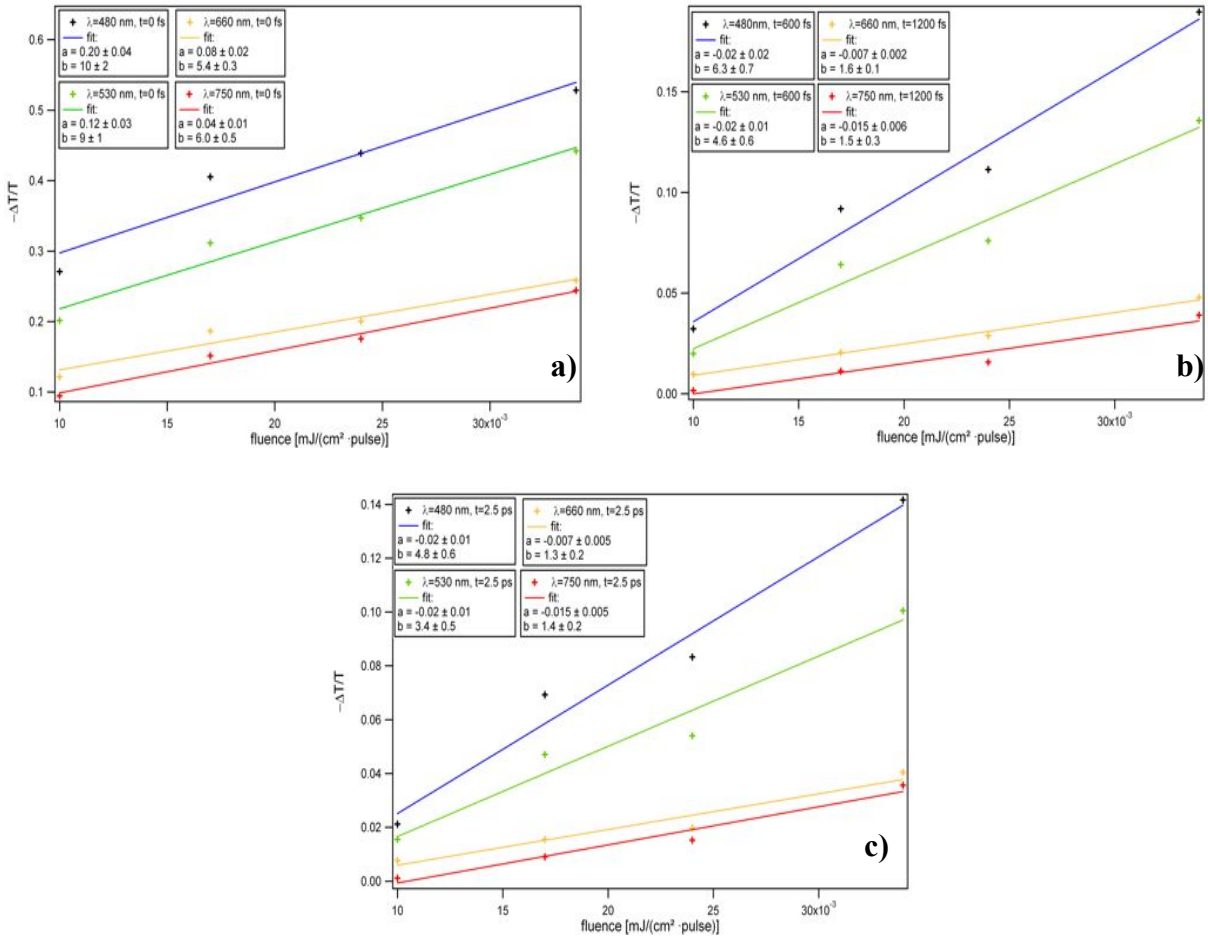


Fig. 7.3: *$CuGeO_3$ ΔT/T versus incident pump fluence at 0 fs (a), 600-1200 fs (b) and 2.5 ps (c) time delays for four different wavelengths. Data are fitted with a function f(x)=a+bx. Fit coefficients are reported in the boxes.*

7.4 Decay Associated Spectra

In this section only measurements with pump and probe pulses parallel to the *c*- axis are reported.

The greatest difficulty found in the analysis of the data arises from the presence of an ultrafast dynamic, whose time constant approaches the experimental time resolution. The deconvolution procedure permits the observation of the dynamics even three times shorter than the duration of the probe pulse. However, in this work the time resolution has not been sufficient, since the fastest process (τ_1) was found to be extremely short. A simple computational simulation of the kinetic trace at 570 nm has shown that τ_1 can not be longer than 15 fs. If it would be larger, for some wavelengths there should be an initial positive $\Delta T/T$ spike, but the data show that the latter quantity is always negative, i.e. only increase of absorption is observed. The point, however, is not only the impossibility to determine the exact τ_1, but above all, the consequent instability of the global fit of the "eigen-traces". There are many very different values of the coefficients a_{1k} (see eq. 6.5) that give equally good fits for the "eigen-traces", but the final Decay Associated Spectra are strongly dependent on the parametric set $\{a_{1k}\}$. The result is that the DAS obtained have

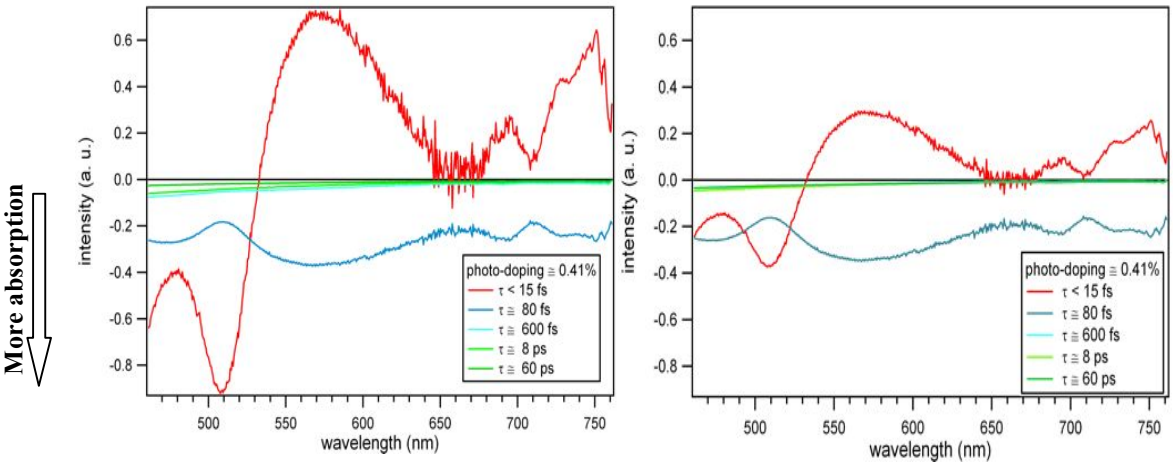


Fig. 7.4: *Two different DAS obtained with equally good fit coefficients. The shape of the bands is the same, as is the sign, but the values of the* $\tau < 15$ *fs associated spectrum are very different!*

generally the right sign and correctly reproduce the structure of the bands, but nothing can be said about the absolute value of the coefficients relative to the first dynamics. The coefficients associated to the other time decays are fortunately little affected by this uncertainty. In fig. 7.4 are reported two different DAS, obtained from two fits having comparable χ^2 values.

Another experimental difficulty is probing the entire visible spectrum with equal resolution. In fact the SC light contains a strong peak at ≈ 800 nm, that corresponds to the wavelength of the beam used for the SC generation (fundamental wavelength). Moreover, SC tends to be particularly unstable in a region between ≈ 730 and ≈ 870 nm. On the other hand, it was not possible to observe the region below ≈460 nm because of unstable scattering of the pump pulse in the $CuGeO_3$ crystal. For these reasons only the CT, ZR and *d-d* bands spectral region between ≈ 460 nm and ≈ 760 nm is presented. The data taken in the red part of the e.m. spectrum are quite noisy and it has not been possible to obtain clear results for fluences below

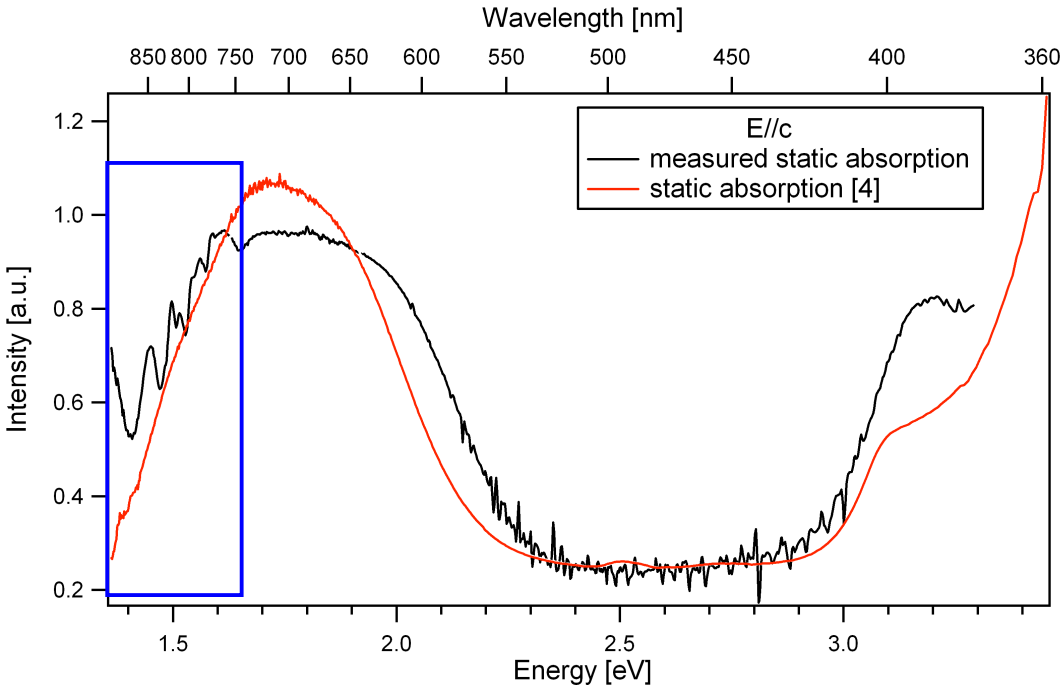


Fig. 7.5: *Comparison between the static spectra taken with our experimental set-up and the data present in literature* [3,4]. *The blue box evidences the region where our spectra are not reliable.*

34 mJ/(cm^2·pulse), corresponding to a power of 3 mW. As shown in fig. 7.5, the static spectra of $CuGeO_3$, compared with the one of Pagliara *et al.* [4], show the zone where the acquired data are not reliable, since unreal features appear.

Hereinafter, the DAS corresponding to different pump power are reported (Fig. 7.6). We stress the meaning of the DAS spectra: each spectrum is associated to a characteristic decay constant and its intensity at a certain wavelength is the value of the pre-exponential coefficient in the fit of the trace at the same wavelength. Therefore, when the coefficients are negative, an increase in the absorption occurs, while when they are positive there is an increase in the transmission (see also fig 7.4).

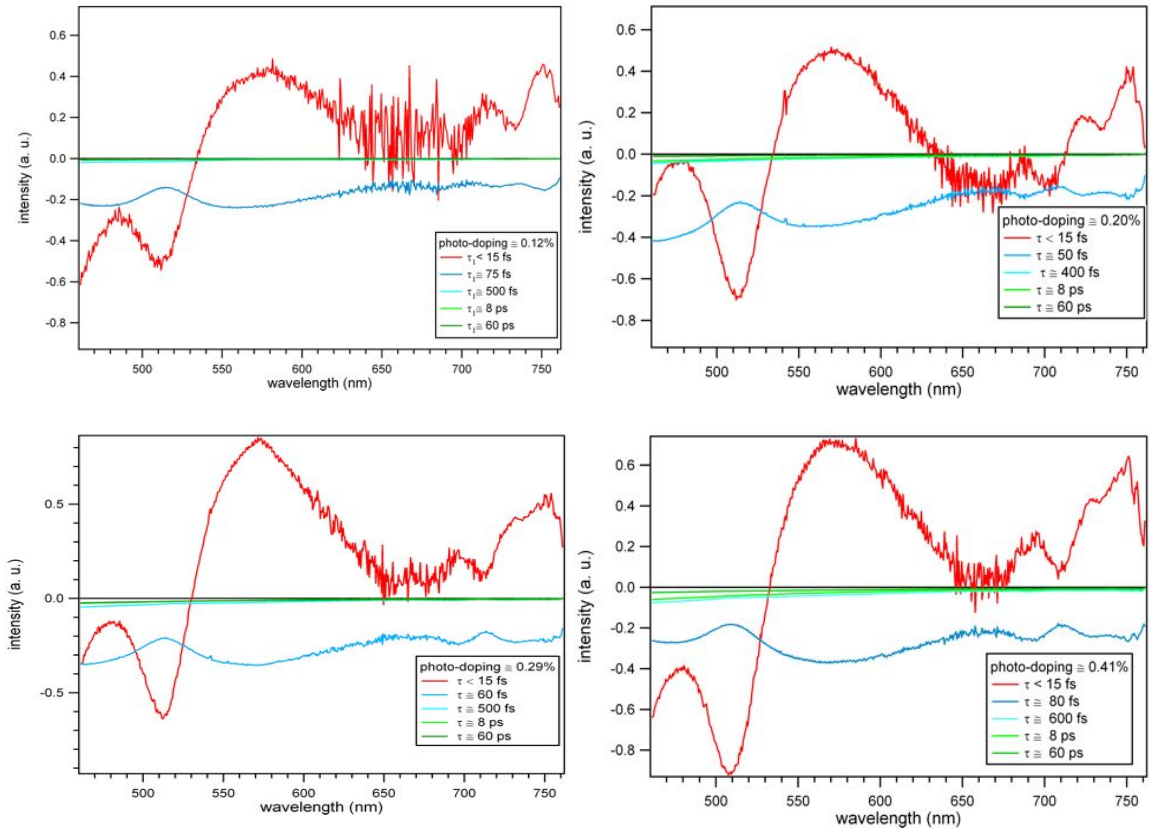


Fig. 7.6: *Decay Associated Spectra relative to different pump powers, in the spectral region between ≈ 460 nm and ≈ 760 nm and for the pump//probe//c polarization configuration.*

7.5 Periodic modulations of transmittivity

Another very interesting point that comes out from the residuals that remains after the multi-exponential fitting, regards the observation of transmittivity modulations, as previously reported in section 7.1. In the measurements presented in fig. 7.8 two oscillations are evident: the first one appears with the arrival of the pump pulse, while the second one appears about 1.25 ps later. Moreover, the first modulation seems to be present for all wavelengths, while the second one is not visible in the entire spectral region covered by the experiment. It is most prominent around 480-510 nm, remains visible until about 670 nm and disappears in the red region of the spectrum (rectangle of fig 7.1 b)).

The best way to analyze these modulations is to consider the residuals of the fit of the DAS "eigen-traces", since the DAS procedure cleans up the data from noise. The residuals have been fitted with a damped cosine function of the form:

$$f(t) = y_0 + A\cos\left(\omega\cdot\left(t - t_0\right) + \varphi\right)\cdot\exp\left(-\frac{t - t_0}{\tau}\right) \tag{7.1}$$

where the parameters A, ω, τ and φ are fit parameters, while t_0 is the time-zero point when pump and probe completely overlap. The value of t_0 has been taken at the maximum of the transmittivity variation, since this point corresponds to the maximum of the cross-correlation curve with an error of $\pm$ 5 fs, as shown in fig. 7.7. From the value of ω, it is possible to recover the period T of the oscillation with the usual relation

$$T = \frac{2\pi}{\omega}. \tag{7.2}$$

To confirm the value of periods obtained with these fits, the FFT algorithm has been applied to the same residuals. Even if the results are quite noisy, some interesting features have been detected. Note that in the FFT the peaks at frequencies higher than 12.5 THz have no significance, because a laser pulse can not excite coherent oscillations with a period shorter than the pulse duration. Similarly, peaks at very low frequencies require some attention: in principle, oscillations of frequency lower than 0.5 THz are not detectable, since their period is longer than a half of the time region

observed. However, this is a lower limit that is true only for oscillations that start at t = 0.

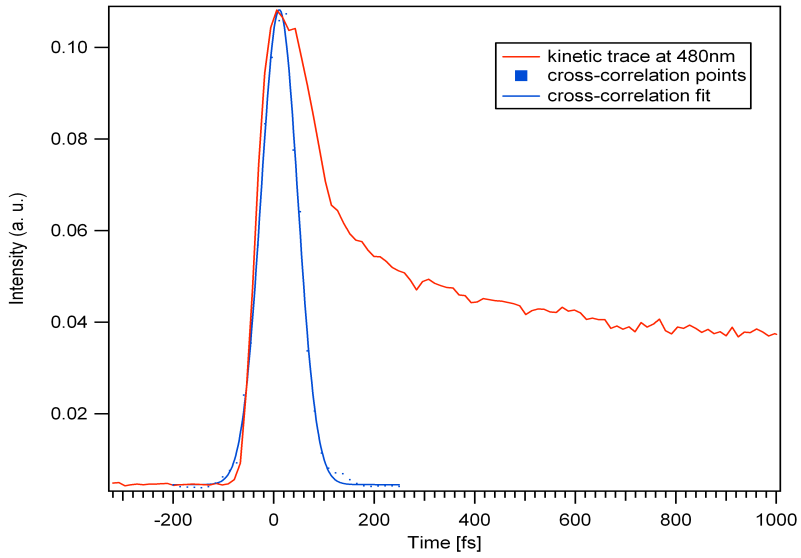


Fig. 7.7: *Comparison between the rise-time of the transmittivity signal and the cross-correlation data. Since the lifetime τ_2 is comparable with the FWHM of the cross-correlation, the time-zero point can be estimated as the maximum of the pump-probe signal.*

- **Pump // probe // c-axis, excitation energy $h\nu$ = 3.14 eV**

This configuration is supposed to be the most interesting, because of the formation of the Zhang-Rice singlet. Measurements at different pump power have been performed and for all powers two different oscillations have been detected: the first starting with the arrival of the pump pulse, while the second starts after more than 1 ps (fig.7.9a)). The first oscillation has a period of about 100 fs, also confirmed also by the FFT analysis (fig.7.9b)), and a dephasing time between 125 and 145 fs. The phase φ of the oscillation deviates from a pure cosine behaviour at most for 28°. This oscillation is present at all the wavelengths, as is shown in fig. 7.11. These measurements confirm a dephasing time of around 135 fs on average.

The second modulation appears ≈ 1240 fs after the time-zero point and exhibits a dephasing time of about 1010 ± 160 fs for a photo-doping of ≈ 0.41%. Data at the other pump fluences, although permitting to detect the presence of a modulation,

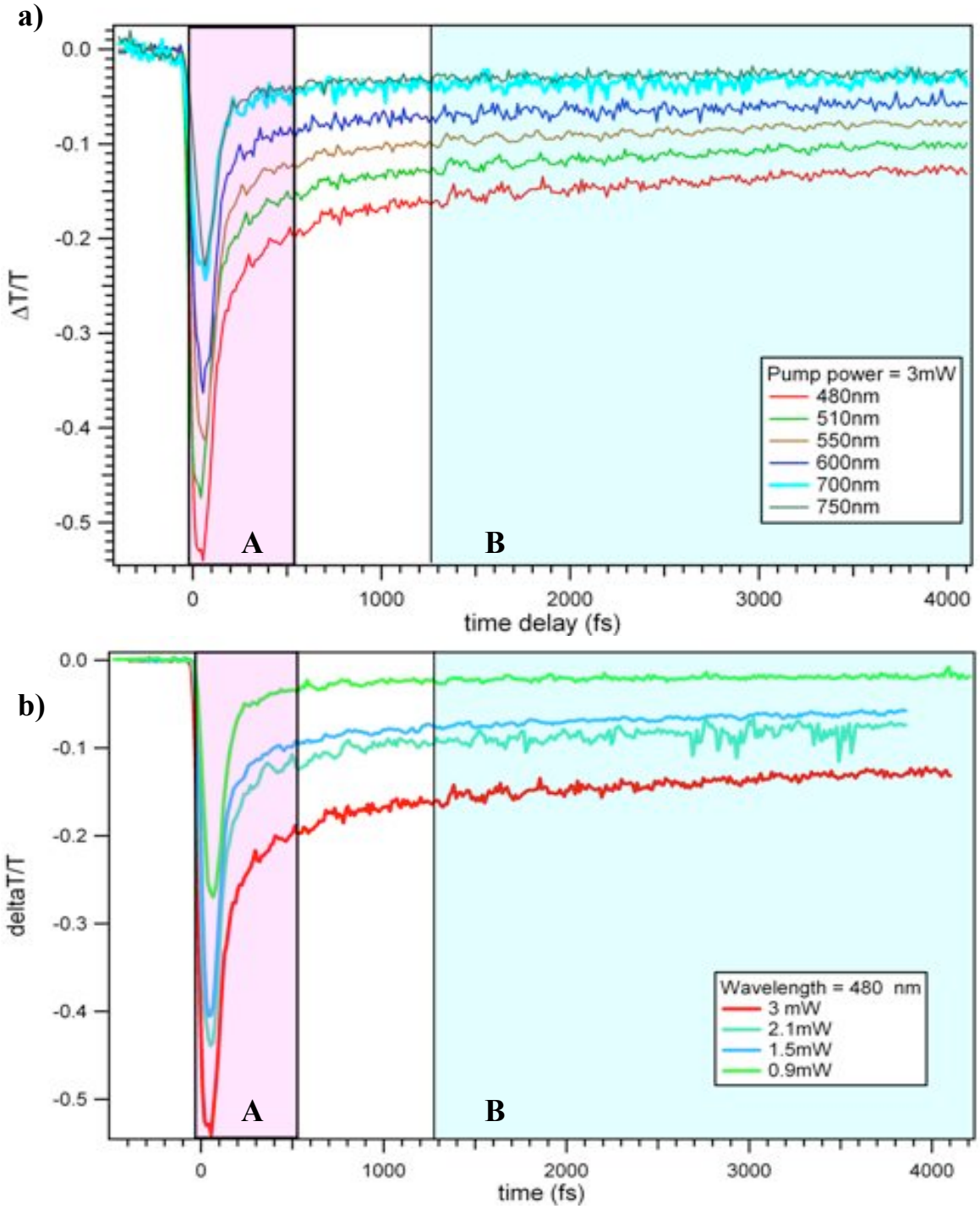
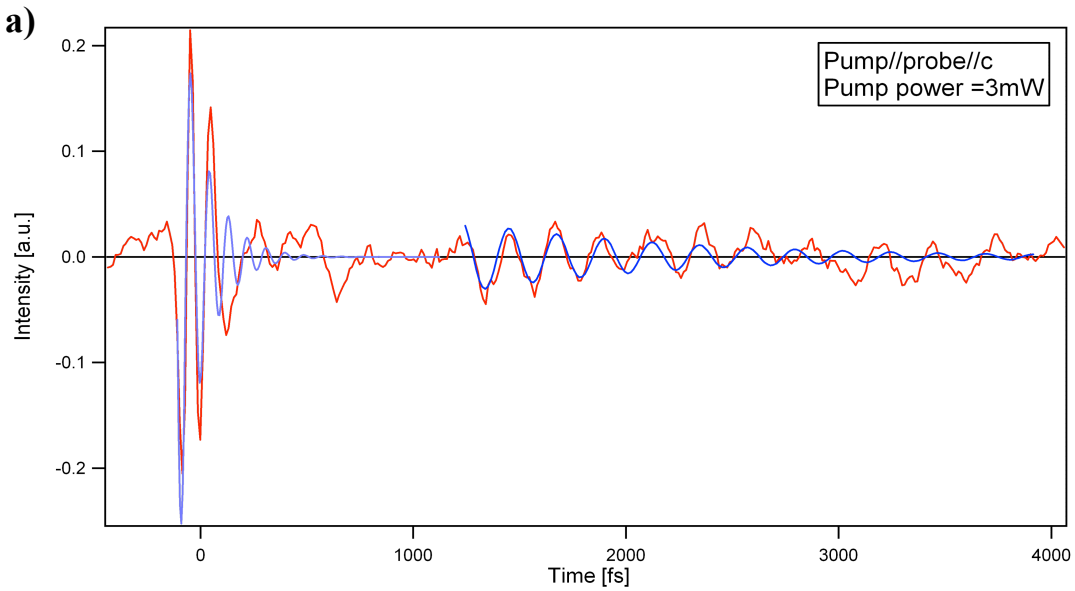


Fig. 7.8: *Kinetic traces for the configuration pump//probe//c. In both graphs are evidenced the regions A (pink) and B (light blue), corresponding to the presence of the two different modulations.* a) D*ifferent wavelengths at pump power of about 3mW. The second modulation become less evident at larger wavelengths and disappear at 700 nm.* b) *Different pump powers at 480 nm.*



	Amplitude (a.u.)	Period (fs)	φ (rad)	φ (degrees)	τ (fs)
A	0.12 ± 0.01	91 ± 2	-0.17 ± 0.08	-10 ± 3	122 ± 15
B	0.034 ± 0.004	233 ± 9	0.3 ± 0.1	17 ± 6	1011 ± 164

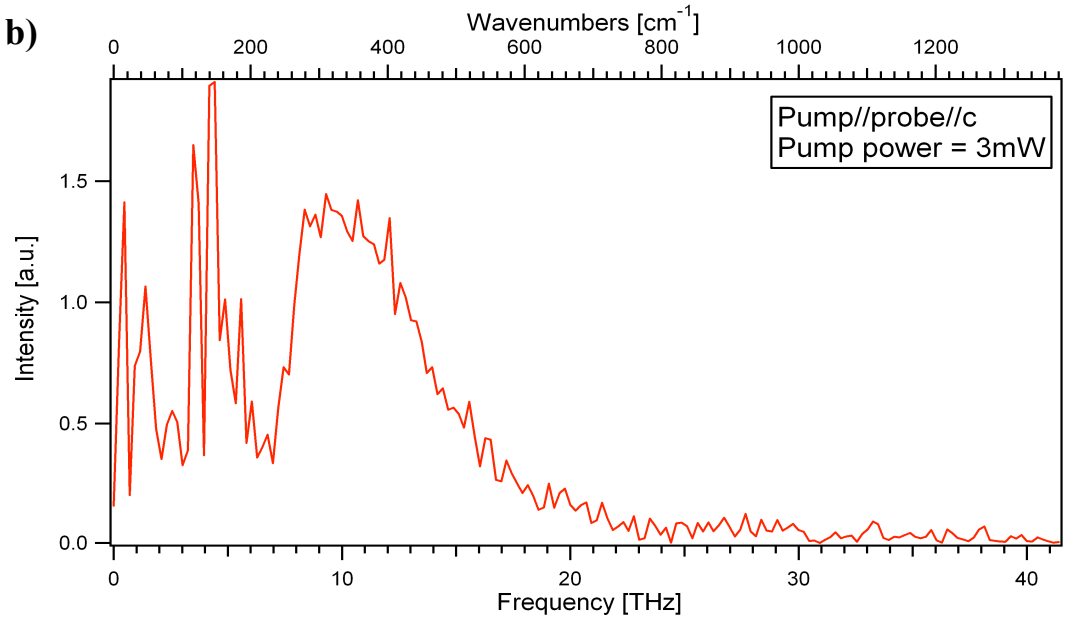
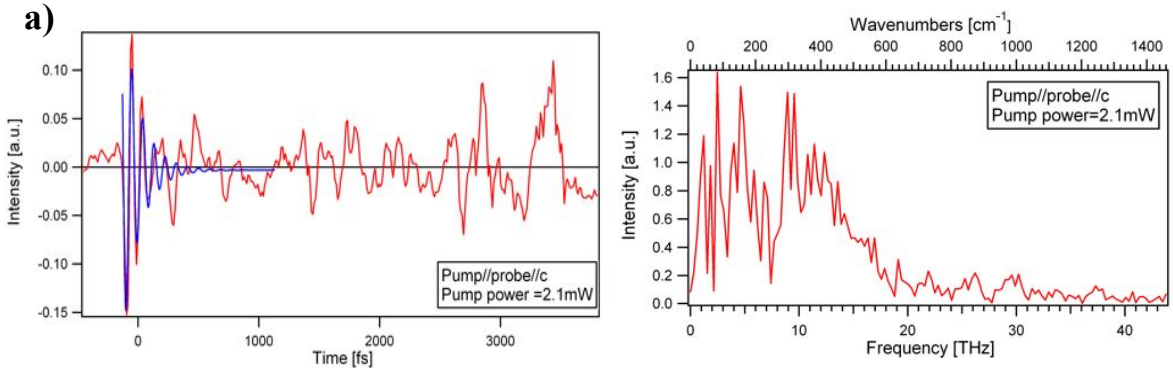


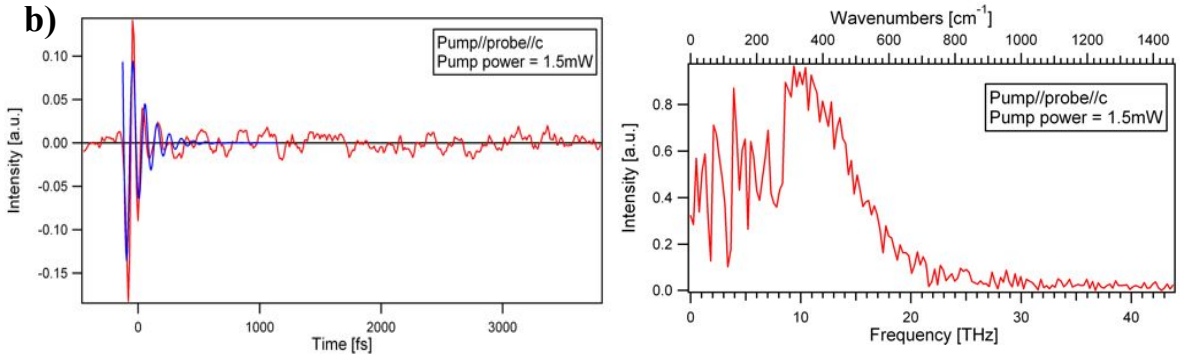
Fig. 7.9: a) *Residual at 3mW (0.41% of photo-doping). The fit for the two oscillations (respectively A and B) are superimposed. The fitting parameters are reported in the table below.* b) *FFT of the residual in* a). *The two main structures at ≈ 130 cm^{-1} (4 THz) and ≈ 330 cm^{-1} (10 THz) correspond to the two modulations detected in* a) *and well reproduce the frequencies obtained from the fits above.*

a)



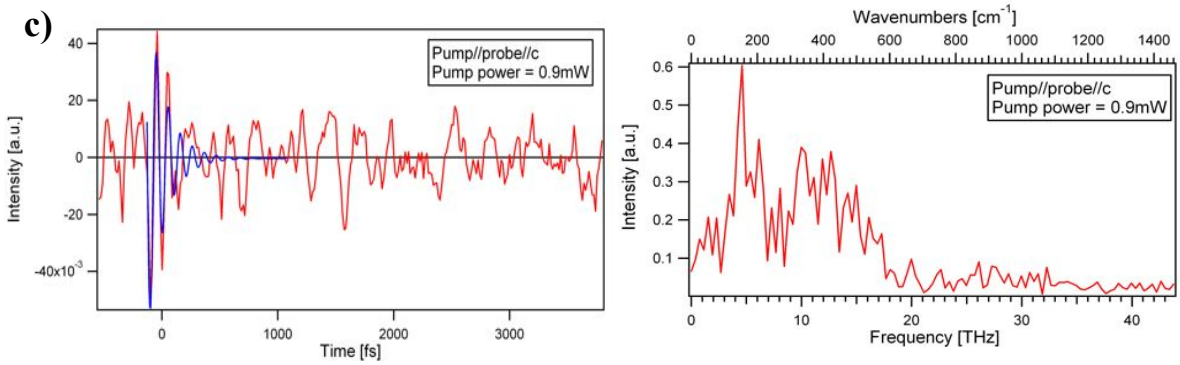
	Amplitude (a.u.)	Period (fs)	φ (rad)	φ (degrees)	τ (fs)
A	-0.071 ± 0.008	92 ± 1	0.4 ± 0.1	23 ± 6	139 ± 23

b)



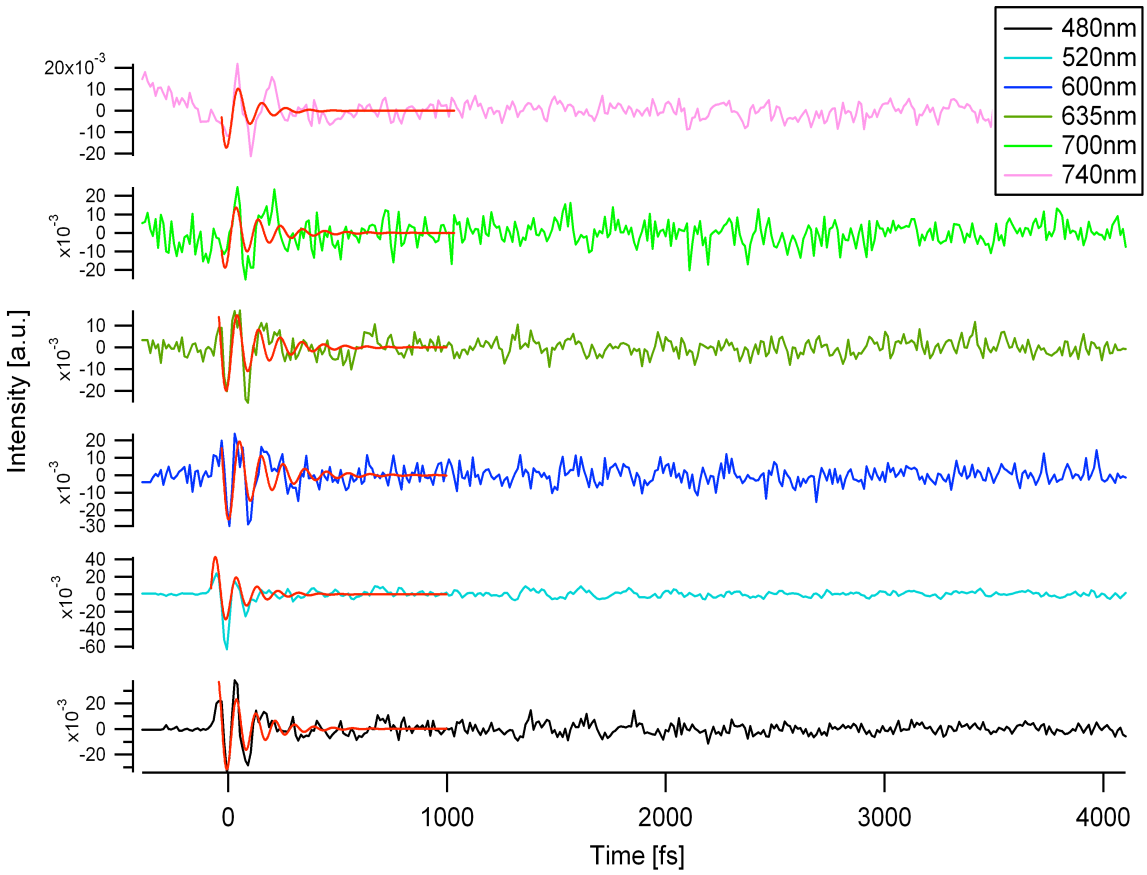
	Amplitude (a.u.)	Period (fs)	φ (rad)	φ (degrees)	τ (fs)
A	-0.069 ± 0.007	100.0 ± 0.2	-0.5 ± 0.1	-29 ± 6	137 ± 21

c)



	Amplitude (a.u.)	Period (fs)	φ (rad)	φ (degrees)	τ (fs)
A	-0.027 ± 0.003	103.6 ± 0.2	-0.3 ± 0.1	17 ± 6	146 ± 28

Fig. 7.10: *Residuals (left) and corresponding FFT graphs (right) for different pump powers.* a) *2.1 mW (0.29% of photo-doping);* b) 1.5 *mW (0.20% of photo-doping);* c) 0.9 *mW (0.12% of photo-doping). The fit of the first oscillation is superimposed to each residual, while the fitting parameters are reported in the tables. In all the FFT graphs appear two main structures at 4.1 THz and 10 THz, that correspond to these oscillations.*



λ (nm)	Period (fs)	φ (rad)	φ (degrees)	τ (fs)
480	90 ± 1	0.2 ± 0.1	11 ± 6	136 ± 28
520	95 ± 1	0.3 ± 0.1	17 ± 6	120 ± 24
600	100 ± 1	-0.6 ± 0.1	-34 ± 6	180 ± 42
635	100 ± 1	0.1 ± 0.1	6 ± 6	166 ± 42
700	101 ± 3	0.3 ± 0.2	17 ± 11	159 ± 67
740	108 ± 2	0.3 ± 0.2	17 ± 11	104 ± 35

Fig. 7.11: *Residuals of kinetic traces at different wavelengths for the configuration pump//probe//c, and pump power = 3mW. The parameters of each fit are reported in the table below.*

are too noisy to permit a reasonable fit. However, they seem to evidence, instead, an increase of the oscillation amplitude with the pump fluence (see fig. 7.8b)). The period of the oscillation has been estimated, from the fit and from the FFT, to be comprise between 227 and 260 fs, corresponding to a wavenumber between 128 and 147 cm^{-1}.

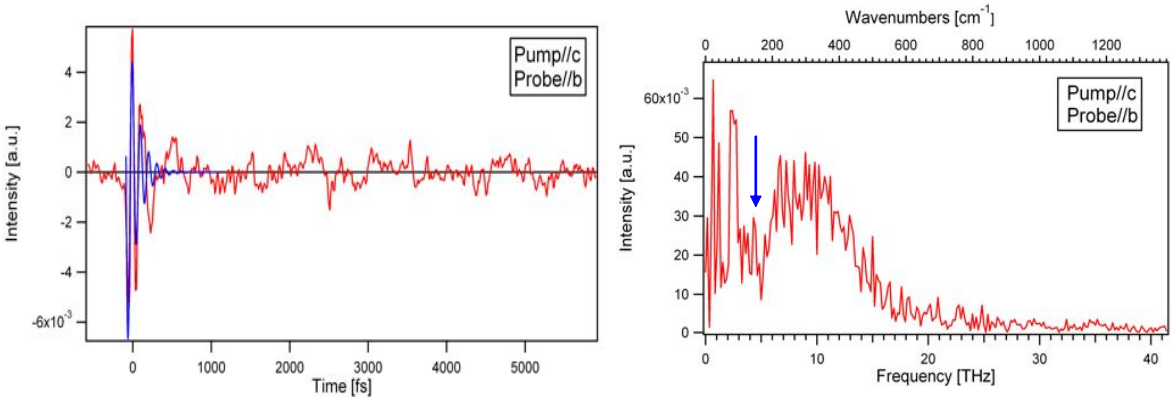
In all the FFT graphs, even if there is a lot of noise, two main structures are evident. Their frequencies are always centred at ≈ 4.1 THz and ≈ 10 THz, corresponding to periods of ≈ 250 fs and ≈ 100 fs respectively.

Note also that the frequencies of the other peaks appearing in the FFT spectra have been calculated but they don't correspond to any lattice mode, being probably noise artefacts.

- **Other polarization configurations**

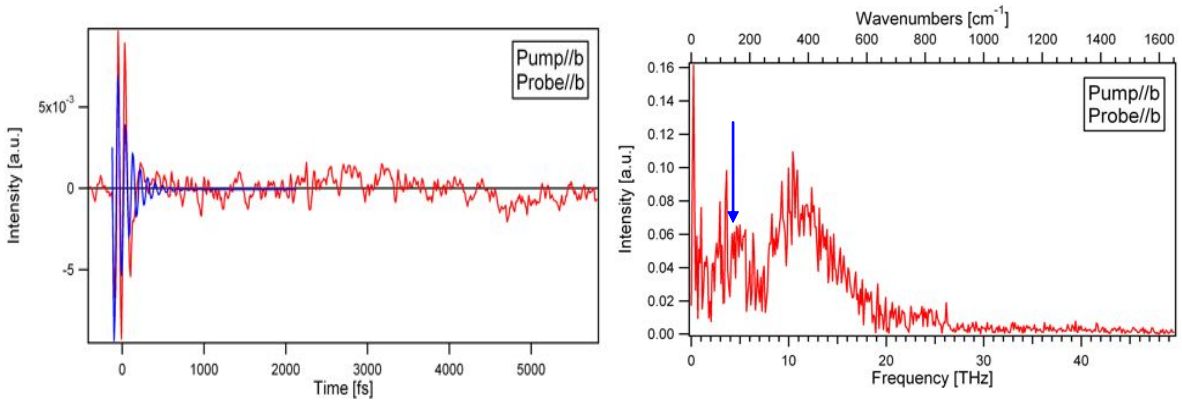
The other configurations for the pump and probe polarization have been studied. In all cases the first oscillation has been detected. The period and the dephasing time are comparable with the results of the preceding section, and the phase differs from cosine at most for 34 degrees.

Looking at the kinetic "eigen-traces", there are no evidences of the presence of the second modulation. Looking at the FFT analysis, however, it may be present in the measurements with pump//c and probe//b, even if there is too much noise to be certain that this oscillation is really present.



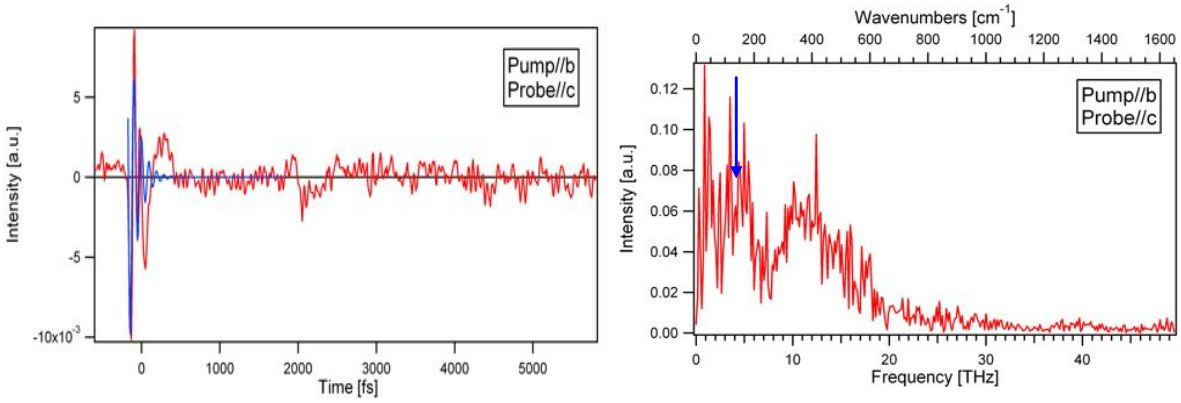
	Amplitude (a.u.)	Period (fs)	φ (rad)	φ (degrees)	τ (fs)
A	-0.0041 ± 0.0004	105 ± 2	-0.35 ± 0.09	-20 ± 5	125 ± 22

Fig. 7.11: *Residuals (left) and corresponding FFT (right) for pump//c-axis and probe//b-axis. The fit of the first oscillation is superimposed to the residual, while the fitting parameters are reported in the table below The blue arrow in the FFT graph indicates where the peak of the T ≈ 250 fs oscillation should appear.*



	Amplitude (a.u.)	Period (fs)	φ (rad)	φ (degrees)	τ (fs)
A	-0.0052 ± 0.0003	91 ± 2	0.31 ± 0.06	18 ± 3	162 ± 19

Fig. 7.12: *Residuals (left) and corresponding FFT (right) for pump//probe//b-axis. The fit of the first oscillation is superimposed to the residual, while the fitting parameters are reported in the table below. The blue arrow in the FFT graph indicates where the peak of the T ≈ 250 fs oscillation should appear.*



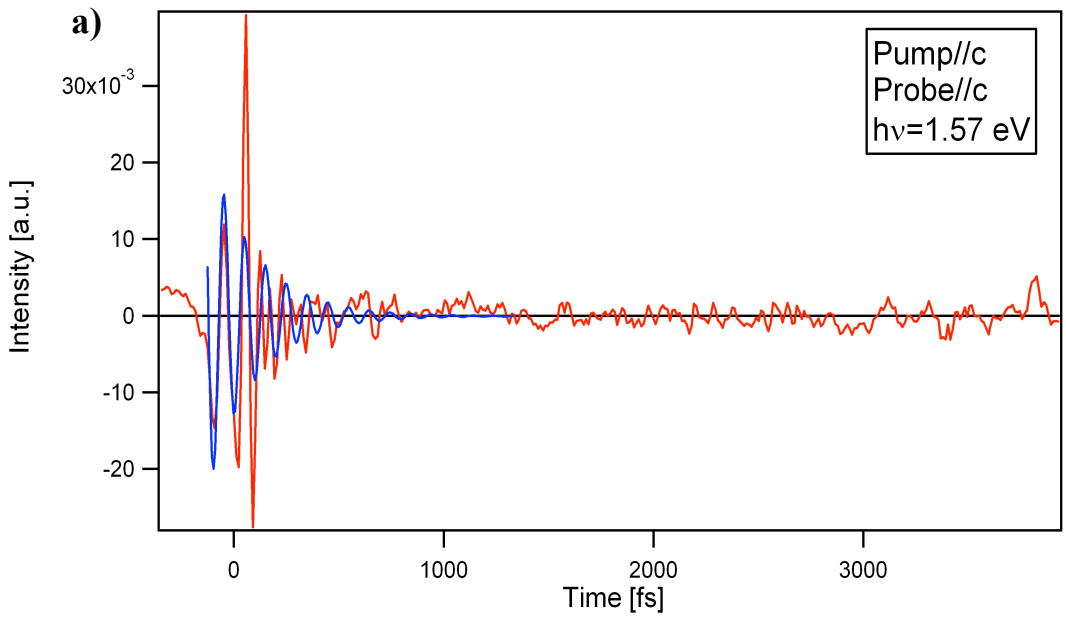
	Amplitude (a.u.)	Period (fs)	φ (rad)	φ (degrees)	τ (fs)
A	0.0025 ± 0.0005	95 ± 2	-0.1 ± 0.2	-6 ± 11	103 ± 15

Fig. 7.13: *Residuals (left) and corresponding FFT (right) for pump//b-axis and probe//c-axis. The fit of the first oscillation is superimposed to the residual, while the fitting parameters are reported in the table below. The blue arrow in the FFT graph indicates where the peak of the T ≈ 250 fs oscillation should appear.*

For the pump//probe//b configuration, the first oscillation is clearly present, while the second one seems to be absent, as shown in fig. 7.13, but bad signal-to-noise ratio again does not allow a certain statement.
Finally, the second modulation seems also to be absent in the pump//b, probe//c configuration, as reported in fig. 7.14.

- **Pump // probe // c-axis, excitation energy $h\nu$ = 1.57 eV**

Finally, the eventual presence of the same oscillations has been checked, in the pump//probe//*c* configuration, with a different excitation energy. The system has been pumped with about 4.5 mW at the energy of the fundamental of the Ti:Sa (≈ 1.57 eV). A modulation starting from the time-zero point with a period of about 97 fs has been found as in the preceding cases, while no other oscillations have been detected. The phase of the modulation has been estimated as ≈13° ± 6°, and the frequency of the oscillation has been checked with the FFT. The results are presented in fig. 7.15a) and b).



Amplitude (a.u.)	Period (fs)	φ (rad)	φ (degrees)	τ (fs)
-0.013 ± 0.001	99 ± 1	-0.2 ± 0.1	-11 ± 6	226 ± 49

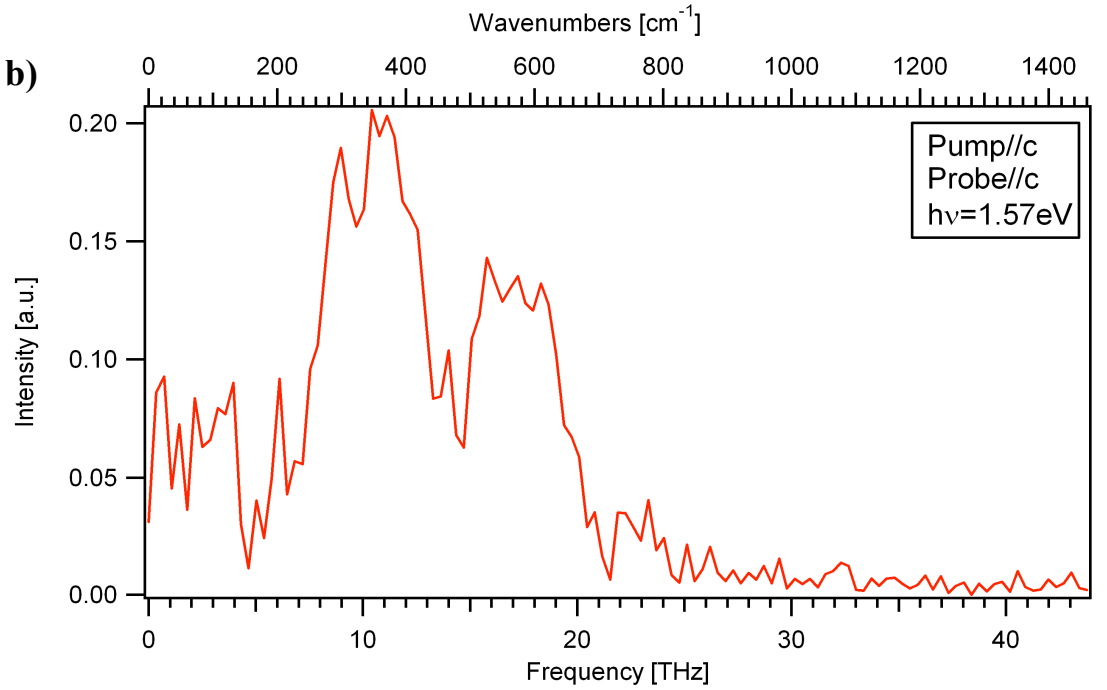


Fig. 7.15: a) *Fit of the 1.57eV measurement's residual for pump power of ≈ 4.5 mW with a cosine damped function. Fitting results for φ and τ are reported in the box.* b) *FFT of the residual reveals the presence of an oscillation corresponding to a period of ≈ 100 fs*

Bibliography:

[1] G.H.Golub, C.F. van Loan, *Matrix Computation,* Johns Hopkins University Press, Baltimore (1996)

[2] I.H.M.Van Stokkum, D.S.Larsen and R. van Grondelle, Biochim. Biophys. Acta 1657, 82-104.v (2004)

[3] Z.V.Popovic, S.Devic, V.N.Popov, G.Dahlenne and A.Revcoleschi, Phys. Rev.B **52**, 4185 (1995)

[4] S.Pagliara, F.Parmigiani, P.Galinetto, A.Recolevschi and G.Samoggia, Phys. Rev. B **66**, 024518 (2002)

Chapter 8

Discussion

In this chapter a detailed discussion and interpretation of the experimental results is given. In particular, the finding of two coherent phonons, originating from two different mechanisms of excitation, is reported in the first section. In the second section, the results of the DAS analysis are interpreted and related to different relaxation processes of the copper germanate system.

8.1 Observation of coherent phonons

One of the most interesting results presented in chapter 7 is the observation of modulations in the differential transmittivity spectra, that show up as two oscillations with different periodicities (≈ 100 fs and ≈ 250 fs). When a thermal excitation occurs, the phases of the lattice oscillations are randomly distributed. Instead, if a coherent light source excites a solid at a frequency higher than the phonon frequencies, coherent lattice oscillations can be observed. The interplay between the excited electron cloud and the lattice coherent displacements originates macroscopic

	Modes	Energy (meV)	Energy (cm^{-1})	Period (fs)
Raman active modes	A_g	22.1 41.3 73.8 106	187 332 594 859	178 100 56 39
	B_{1g}	48	388	86
	B_{2g}	14.4 27.7 53 109	116 224 427 879	287 149 78 38
	B_{3g}	13.6 51 88.3	110 411 712	303 81 46.8
Infrared active modes	B_{1u}	16.3-16.6 40.5-46.1 59.3-60.6 76.2-79.5 105-109	131-134 328-372 478-489 615-640 843-880	253-249 102-89.6 69.7-68.2 54.2-52 39.5-38
	B_{2u}	20.5-20.9 65.6-74.3 89.2-99.6	165-168 530-600 720-803	202-198 63-55.6 46.3-41.5
	B_{3u}	59.5-60.8 26.2-28.7 35.3-38.3 46.7-51.3 95.7-106	48-49 211-231 285-308 377-414 772-857	694-680 158-144 117-108 88.4-80.5 43.2-39

Table 8.1: *Table of all measured phonons of $CuGeO_3$ with respective periods* [7]. *For each IR active phonon two values are given, that refer to the transversal optical (TO) and longitudinal optical (LO) modes respectively.*

oscillations of the dielectric function. The resultant effect is a periodic variation of the complex refractive index at the same coherent phonon frequency. In the measurements presented in section 7.5, two of such modulations have been detected. Since they have different periods, respectively of ≈ 100 fs and ≈ 250 fs, they are related to two different coherent phonons. Comparing the frequencies of these

oscillations with the infrared and Raman spectra reported in literature (see table 8.1), the first oscillation has been assigned to the A_g mode (≈ 332 cm^{-1}), while the second has been assigned to the B_{1u} phonon at ≈ 131 cm^{-1}. These two phonons are different, both in symmetry and in activation time. The A_g phonon is a totally symmetric even mode, that starts to oscillate at the arrival of the pump pulse, while the B_{1u} phonon is an infrared (IR) active odd mode that exhibits an activation time of ≈1240 fs. Moreover, the A_g mode is present at all the wavelengths observed and for every pump and probe polarization configuration, and it remains present also when the photon excitation energy is changed from 3.14 eV to 1.57 eV. On the other hand, the B_{1u} phonon has been detected only for the pump//probe//*c* configuration, with excitation energy of 3.14 eV, i.e. when the ZR singlet is excited. All these observations suggest that two different mechanisms may be involved for these coherent phonon excitations.

- **A_g phonon**

As previously discussed in chapter 3.4, the main mechanism of coherent phonon generation in non metallic solids has been identified in the Impulsive Stimulated Raman Scattering (ISRS), of which the Displacive Excitation of Coherent Phonons (DECP) model represents only a particular case [1,2,3]. Stimulated Raman scattering can be described by two tensors, one of which accounts for the phonon-induced modulation of the susceptibility and the other one for the dependence of the coherent mode amplitude on the light intensity [6]. These tensors differ only in the imaginary parts. When the imaginary part dominates, an absorption occurs, the excitation can be described with a step-like driving force and the DEPC mechanism results [2,6]. The photo-excited electrons create instantaneously a non-equilibrium charge distribution, and, as a result, the crystal lattice starts to oscillate around the new equilibrium position, with phonon oscillations that show a cosine dependence. At the first order, only the A_g totally symmetric modes are coherently excited by the DECP mechanism [5], and this is probably the case of the A_g coherent phonon observed in the present experiment. On the other hand, when the real component of the two tensor dominates, the driving force is impulsive-like and ISRS occurs. This is

the case of below-gap excitations, when no absorption occurs, and the excited phonons exhibit a sine dependence [2,6].

To verify the DECP origin of the A_g coherent oscillation, it has been checked if this phonon starts to oscillate at the arrival of the pump pulse (t = 0) with a cosine behaviour. For this scope, the fit of the residuals, with a cosine damped function of the form

$$f(t) = y_0 + A\cos\left(\omega\cdot\left(t - t_0\right) + \varphi\right)\cdot\exp\left(-\frac{t - t_0}{\tau}\right), \tag{8.1}$$

has been considered. As reported in the tables of fig. 7.8-7.14, the phase φ turned out to differ from 0 at most 34°, but generally less than 20°, confirming the cosine behaviour of this oscillation. Moreover, the amplitude of coherent oscillations increases monotonically with the pump fluence, and it is known that for DECP mechanism this trend is linear [1]. Considering the amplitude dependence on the pump fluence, a monotonic increasing trend is evident from the experimental data (see fig. 8.1), but unfortunately it has not been possible to determine with certainty if the relationship is linear, because too few points are obtained from our measurements.

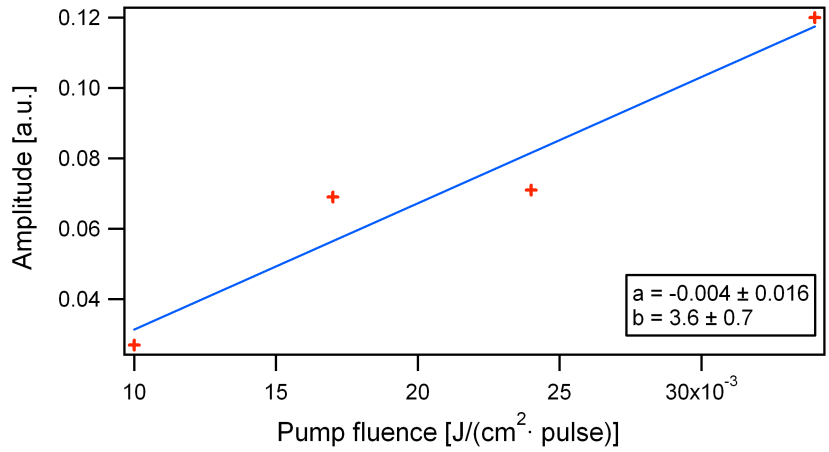


Fig. 9.1: *Amplitude of the coherent A_g oscillation versus the incident pump fluence. The data are fitted with a linear function f(x)=a+bx and the fitting parameters are reported in the box.*

The dephasing time τ for the A_g phonon results, on the average, ≈ 140 fs. It does not show any detectable dependence on pump fluence or polarization configurations. A slight increase of τ has been detected (from ≈ 140 to ≈ 230 fs) when the photon energy is diminished from 3.14 eV to 1.57 eV. On the basis of what has been said in chapter 3.3 about the main dephasing mechanisms, the fact that the frequency and damping of the coherent A_g phonon does not change with the pump fluence supports the conclusion that this dephasing process is dominated by anharmonic phonon-phonon coupling (which is determined by the lattice temperature) rather than via scattering with excited electrons. However, it would be interesting to study the temperature dependence of the amplitude and dephasing time for this mode by repeating the measurements at lower temperatures. Finally, by varying excitation energy, it would be possible to check if the observed increase of the dephasing time when photon energy goes down is a part of a general trend or just an experimental uncertainty.

- **B_{1u} phonon**

As already mentioned, the B_{1u} phonon at ≈ 131 cm^{-1} is an IR active odd mode. In a centrosymmetric compound, such as the $CuGeO_3$ (D_{2h}^5) [8], only Raman (even) modes can be excited by ISRS or DECP mechanisms. This is because the operators of the electric dipole moment and of the polarizability, that control respectively the absorption and the Raman scattering processes of a photon by a phonon, have opposite parity: the first one is odd under inversion, while the second one is even. In a centrosymmetric crystal, the vibrational modes have either even or odd parity under inversion. As a consequence, the odd parity modes are IR active, while the even parity modes are Raman active (Rule of Mutual Exclusion). Only in crystals that do not posses inversion symmetry, some modes may be simultaneously IR and Raman active [9-11].

The above observation and the fact that both ISRS and DECP mechanisms are directly induced by the photons of the laser pulses, producing phonons that start to oscillate with the arrival of the light pulse, allow us to conclude that these processes are not responsible for the excitation of the B_{1u} phonon. The mechanism involved in coherent excitation of the latter may be the electron-phonon coupling,

largely discussed in section 3.4. The hypothesis is supported by the observation that this oscillation appears only after ≈ 1250 fs. This retarded activation may be consistent with the fact that the electron-phonon coupling process needs some time to become efficient. In metals, the non-equilibrium condition is treated with the two-temperature model (TTM) [4,5,12]. Since the electron-electron thermalization is much faster than the electron-phonon thermalization, excited electrons fast thermalize at a temperature T_e, that is higher than the lattice temperature T_l. Only later, the electron-phonon thermalization occurs. In metals, electrons thermalize in tens of fs and the electron-phonon thermalization occurs in a ≈ 100 fs -1 ps range [5], so that 1 ps after the absorption, the electrons have already cooled down and only the nuclear motion persists. In strongly correlated insulators, however, excited electrons are localized and the system can be no more described by a "gas" of hot electrons surrounding a cold ionic lattice, and the TTM is no more adequate. Actually, to find the times after which a certain electron-phonon interaction becomes efficient requires the knowledge of the time-dependent scattering function between the two states, i.e. the matrix element of the time-dependent electron-phonon interaction between the final and the initial wave-functions. However, it is not possible to obtain a reliable estimation of this parameter without high level numerical simulations, because of the extremely complex nature of the wave functions, which contain nuclear and electronic components that cannot be simply factorized. Alternatively, the detected B_{1u} coherent oscillation may be the result of a phonon-phonon coupling with another mode previously coherently excited. Such a phonon has not been detected in the present measurement, maybe because its period is much shorter than duration of our probe pulse, so that eventual fast modulations are smoothed out. Thus, with the current time resolution, both electron-phonon and phonon-phonon coupling mechanisms may be responsible for the formation of the B_{1u} coherent phonon.

B_{1u} phonon exhibits a dephasing time much longer than the lifetime of the A_g mode: it is ≈ 1010 ± 160 fs for a photo-doping of ≈ 0.41%. As previously said in section 7.5, although the data at other pump fluences permit the detection of the B_{1u} phonon, the signal-to-noise ratio forbids a reasonable fit. Neverthless, a clear increase of the oscillation amplitude with the pump fluence is observed, as reported

in fig. 7.8. This oscillation is detectable only in a limited spectral region in the transmittivity measurements (470-680 nm), and it is clearly evidenced only for a single polarization configuration (pump//probe//*c*).

To explain the above observation, the dielectric function of $CuGeO_3$ needs to be considered. A coherent oscillation can be detected in a time-resolved transmittivity variation measurement because the coherent lattice motion induces a coherent oscillation of the electronic distribution, and an oscillating dielectric function results. Thus the fact that, while the A_g phonon is detected at all the wavelengths, the B_{1u} phonon is present only for $\lambda<680$ nm, with an intensity that decreases in going to the red, is a signature that the non-equilibrium dielectric function is stronger perturbed in the vicinity of the pump excitation energy.

The B_{1u} phonon has been detected only with pump pulse//probe//*c*-axis and excitation energy of 3.14 eV. Maintaining the same polarization configuration but changing the excitation energy to 1.57 eV causes the disappearance of such oscillation. This may be a signature that the generation mechanism of the coherent B_{1u} phonon excitation is strongly correlated to the excitation of the Zhang-Rice singlet, since the latter is excited only when pump polarization is parallel to the *c*-axis. However, B_{1u} phonon has not been clearly detected in the pump//*c*, probe//*b* configuration. A possible explanation of its absence in this case is related to the symmetry properties of B_{1u} phonon. As pictured out in fig. 9.2 b), the ionic displacements related to the B_{1u} mode are very complex and they occur along all 3D directions. However, in standard IR absorption measurements, it is a mode that can be detected only with the electric field polarization along the *c*-axis. Therefore, a reasonable guess is that the preferential oscillation is along the *c*-axis, while in the other directions it is very weak. If it is the case, the oscillation of the dielectric function shows a strong anisotropy: being strongly perturbed only in *c* direction, an orthogonal probe field can only detect a small out-of-axis component of the oscillation. In the pump//*c* probe//*b* configuration a small peak in the FFT corresponding exactly to a 131 cm^{-1} oscillation is present, but it is too small to permit us to say that it is a real oscillation and not a noise artefact, moreover since a clear oscillation is not directly visible in the residual trace. At present, we can only say that

the component of the B_{1u} induced oscillation of the dielectric function along the *b*-axis is smaller than our experimental sensibility.

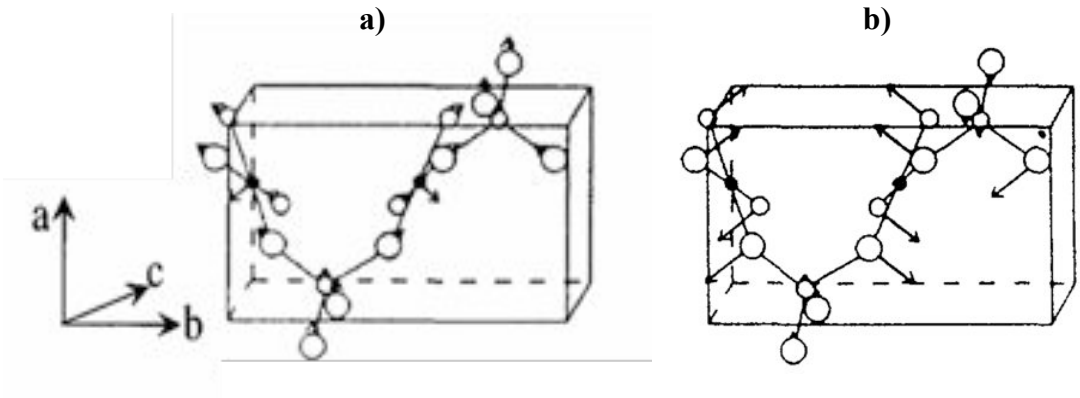


Fig. 9.2: a) *Atoms displacements relative to the 131-134 cm^{-1} B_{1u} mode of $CuGeO_3$* [7]. a) *Atoms displacements relative to the 332 cm^{-1} A_g mode of $CuGeO_3$* [7].
In both the pictures black spheres are Cu ions, small white spheres are Ge ions while big white ones are the Oxygens.

In conclusion, the origin of the two coherent phonons detected is different: the A_g phonon is generated through a DECP mechanism, and therefore is directly induced by the pump pulse. B_{1u} oscillation, instead, is induced by a completely different mechanism, because it starts to oscillate about 1.2 ps after the arrival of the pump pulse. Two processes have been individuated, that can be at the origin of the coherent B_{1u} phonon excitation: the electron-phonon coupling or the population decay process of other coherent phonons. Even if no other coherent oscillations immediately preceding the B_{1u} one have been detected in the experimental data, the phonon-phonon coupling origin can not be excluded, because there may be a preceding coherent phonon with a period much shorter than the probe pulse duration and so not detectable with our experimental setup. However, the electron-phonon mechanism is retained as the more plausible, since the excitation of this mode seems to be strongly correlated with the Zhang-Rice singlet formation.

8.2 Electron distribution relaxation dynamics

From the time-resolved measurements and the DAS analysis, at least six different relaxation dynamics can be evidenced.

The most interesting results regard the presence of at least two ultrafast electronic processes with different lifetimes. The first one, whose lifetime is shorter than 15 fs, is very likely the ZR singlet. Unfortunately, no lifetime measurements for this kind of exciton are present in literature. However, it is possible to obtain an order of magnitude for this lifetime from the line-width γ of the absorption peak corresponding to the exciton energy, by using the absorption spectra of $CuGeO_3$ reported in fig. 4.5(c) [3] and the relation

$$\tau = \frac{\hbar}{\gamma} = \frac{658(meV \cdot fs)}{\gamma(meV)}. \tag{8.2}$$

A proper evaluation of γ requires to avoid the inhomogeneous broadening contribution to the absorption peak, due to the coupling of the ZR exciton with phonons. For this reason the calculation has been performed at the lowest accessible temperature (T=15 K), giving an estimation for the exciton lifetime of $\tau \cong 13$ fs. Moreover, the τ_1 Decay Associated Spectrum exhibits a drop in the absorption for a large spectral range around the *d-d* energy (see fig. 7.6). This behaviour could be ascribed to the CT effect on the *d-d* transitions: immediately after the ZR formation, some *d*-shell have been filled with an electron coming from the oxygen 2*p* shell. The number of sites where an almost forbidden *d-d* transitions can occur diminishes and, consequently, also the absorption goes down respect to the unperturbed case. Both these results support the hypothesis that the first dynamics observed is related to the relaxation of the ZR singlet.

A detailed interpretation of the interplay between the relaxation processes and the photo-induced modifications of the $CuGeO_3$ band structure requires computational simulations and overtakes the scope of the present thesis. However, it can be noticed that the wavelength dependence of the relaxation time τ_3 supports the hypothesis that this process is related to an electron-phonon interaction mechanism. Instead, the processes slower than 8 ps are ascribed to the lattice relaxation and

thermal cooling into the environment, since up to now all electronic relaxations reported in litterature are faster than 4 ps [4,13].

An extremely interesting point regards, instead, the long relaxation mechanisms. In fact the present measurements show that even a photo-doping of less than 0.5% destabilizes the system so much that even after 860 ps it has not recovered the initial state.

Bibliography:

[1] H.Zeiger, J.Vidal, T.K.Cheng, E.P.Ippen, G. and M.S. Dresselhaus, Phys. Rev. B **45,** 768 (1992)

[2] G.A.Garrett, T.F.Albrecht, J.F.Whitaker and R.Merlin, Phys. Rev. Lett. **77,** 3661 (1996)

[3] A.I.Lobad and A.J.Taylor, Phys. Rev. B **64,** 180301 (2001)

[4] L.Perfetti *et al.*, Phys. Rev. Lett. **97,** 067402 (2006)

[5] M.Hase, K.Ishioka, J.Demsar, K.Ushida and M.Kitajima, Phys. Rev. B **71,** 184301 (2005)

[6] T.E.Stevens, J.Kuhl and R.Merlin, Phys. Rev. B **65,** 144304 (2002)

[7] Z.V.Popovic, S.Devic, V.N.Popov, G.Dahlenne and A.Revcoleschi, Phys. Rev. B **52**, 4185 (1995)

[8] Theo Hahn, *International Tables for Crystallography vol.A*, Kluwer Academic Publishers (1996)

[9] M.Fox, *Optical Properties of Solids*, Oxford University Press (2001)

[10] P.Atkins, R.Friedman, *Molecular Quantum Mechanics*, Oxford University Press (1996)

[11] D.A.Long, *The Raman Effect*, John Wiley & Sons (2002)

[12] R.H.M.Groeneveld, R.Sprik and A.Lagendijk, Phys. Rev. B **51,** 11433 (1995)

[13] P.Ruello *et al.*, Physica B **363**, 43 (2005)

Chapter 9

Conclusions

In this thesis, the electronic and lattice non-equilibrium dynamics in the photo-excited $CuGeO_3$ samples have been explored with time-resolved pump-probe transmittivity measurements.

In particular, some parameter of the dynamics of the Cu *d-d* transitions induced by photo-induced O2*p*→Cu3*d* charge transfer has been observed and measured. The main results being a time shorter than 15 fs for the excitation of the ZR singlet and a very long relaxation time, i.e. higher than 800 ps, of the *d-d* electronic configuration has been observed. The impressive amount of data collected in the time and energy domains are such that their analysis will require a study that overtakes the scope of the present work. In this respect, the present experiment will open a new interesting and important perspective in the understanding of the dynamics of strongly electron-correlated materials.

To obtain the experimental results presented here, a novel experimental setup, that allows broad-band detection (using super-continuum probe pulse) of differences in transmittivity in pump-probe experiments in the femtosecond time domain, has

been designed and constructed. The advantage of super-continuum probing over traditional one-wavelength pump-probe setup is that it greatly facilitates the separation of different relaxation processes and their spectral features in the excited state. The broad band probing also makes possible the detection of the transmittivity modulations, induced by coherent phonons, whose amplitude can be less than 4% of the total signal.

Multi-exponential modelling of the differential transmittivity has revealed the presence of at least six different relaxation processes in the 400 nm − 800 nm spectral range. Very likely, the ZR singlet disexcitation is the fastest one. In fact, it has a characteristic time shorter than 15 fs, in accordance with the ≈ 13 fs lifetime evaluated from the line-width of the ZR absorption peak. However, for all the relaxation processes with a lifetime shorter than 100 fs, the observed spectral features can not be interpreted without a detailed knowledge of the complete $CuGeO_3$ band structure and high-level numerical calculations. A process whose relaxation time is wavelength dependent (500 fs - 1.2 ps), is ascribed to electron-phonon coupling mechanisms. Dynamics slower than 8 ps are ascribed to lattice relaxation and thermal cooling into the environment. Interestingly, a <0.5% photo-doping of the sample with Zhang-Rice singlets generates a relaxation process longer than 1.9 ns, showing that even such small excitations strongly destabilize the system.

Two coherent phonons have been detected in the transmittivity variation spectra. The origin of these oscillations is different, since they differ in symmetry and activation time. The first one is a totally symmetric Raman A_g mode of period ≈ 100 fs. The oscillation starts at the arrival of the pump pulse with a cosine behaviour, supporting the conclusion that the excitation mechanism is the Displacive Excitation of Coherent Phonons (DECP), i.e. it is directly induced by the pump pulse.

For the first time an IR phonon, coherently excited by the ZR singlet excitation, has been detected. This phonon, whose period is ≈ 250 fs, activates only after 1.25 ps. Its generation mechanism can be ascribed either to the coupling with

the electronic system or with other coherently excited phonons. With the current time resolution both models are plausible and further investigation is needed.

For both phonons the dephasing time has been measured, and their polarization-dependent excitation has been studied. The A_g mode turns out to be excited for pump polarizations along the *c* and *b*-axis, and it is present also when the energy of excitation is decreased to 1.57 eV. On the contrary, the B_{1u} phonon appears only when both the pump and the probe pulses are polarized along the *c*-axis, and the excitation energy is set at 3.14 eV, corresponding to the resonant energy for the formation of the ZR exciton. This is a signature that the mechanism of the coherent B_{1u} phonon excitation is strongly entangled with the excitation of the Zhang-Rice singlet. The apparent absence of the B_{1u} phonon in the pump//*c*, probe//*b* configuration has been explained as a consequence of the anisotropy of the lattice oscillation, being preferential along the *c*-axis and much weaker in the orthogonal directions. Therefore for a probe pulse parallel to the *b*-axis, the sensitivity of our experimental setup may be not sufficient to detect this oscillation.

Contents

Contents 1

Riassunto 3

Chapter 1: Introduction 6

Chapter 2: Charge transfer processes and the Zhang-Rice singlet in cuprates 10
2.1 Strongly correlated systems 10
2.2 The case of the cuprates 15
Bibliography 17

Chapter 3: Photo-excitation processes through the correlation-gap in CT insulators 18
3.1 Photo-excitation processes through the gap in solids 18
3.2 Electronic effects 19
3.3 Photo-excitation of the Zhang-Rice singlet 21
3.4 Lattice effects 22
Bibliography 26

Chapter 4: The $CuGeO_3$ and its properties 28
4.1 $CuGeO_3$ crystal structure and its main properties 28
4.2 Ligand-field description of the bonds structure 30
4.3 Optical absorption spectra and the Zhang-Rice signature in $CuGeO_3$ 33
4.4 Phonons in $CuGeO_3$ 36
Bibliography 38

Chapter 5: Experimental 40
5.1 Charge transfer photo-excitation in $CuGeO_3$ 40
5.2 Pump-probe technique 42
5.3 Laser system 42
5.4 Pump-probe setup 43
5.5 Supercontinuum generation 45
5.6 Pump power 47
5.7 Data acquisition 50
5.8 Data treatment and setup characterization 51
Bibliography 57

Chapter 6: Data analysis techniques 58
6.1 Singular Value Decomposition technique 58

6.2 Fast Fourier Transform 62
Bibliography 63

Chapter 7: Results 64
7.1 Matrices of data 64
7.2 Time dynamics of the relaxation processes 66
7.3 Dependence of transmittivity on the pump fluence 67
7.4 Decay Associated Spectra 69
7.5 Periodic modulations of transmittivity 72
Bibliography 82

Chapter 8: Discussion 83
8.1 Observation of coherent phonons 83
8.2 Electron distribution relaxation dynamics 91
Bibliography 92

Chapter 9: Conclusions 93

Ringraziamenti 96

Contents

Contents 1

Riassunto 3

Chapter 1: Introduction 6

Chapter 2: Charge transfer processes and the Zhang-Rice singlet in cuprates 10
2.1 Strongly correlated systems 10
2.2 The case of the cuprates 15
Bibliography 17

Chapter 3: Photo-excitation processes through the correlation-gap in CT insulators 18
3.1 Photo-excitation processes through the gap in solids 18
3.2 Electronic effects 19
3.3 Photo-excitation of the Zhang-Rice singlet 21
3.4 Lattice effects 22
Bibliography 26

Chapter 4: The $CuGeO_3$ and its properties 28
4.1 $CuGeO_3$ crystal structure and its main properties 28
4.2 Ligand-field description of the bonds structure 30
4.3 Optical absorption spectra and the Zhang-Rice signature in $CuGeO_3$ 33
4.4 Phonons in $CuGeO_3$ 36
Bibliography 38

Chapter 5: Experimental 40
5.1 Charge transfer photo-excitation in $CuGeO_3$ 40
5.2 Pump-probe technique 42
5.3 Laser system 42
5.4 Pump-probe setup 43
5.5 Supercontinuum generation 45
5.6 Pump power 47
5.7 Data acquisition 50
5.8 Data treatment and setup characterization 51
Bibliography 57

Chapter 6: Data analysis techniques 58
6.1 Singular Value Decomposition technique 58

6.2 Fast Fourier Transform 62
Bibliography 63

Chapter 7: Results 64
7.1 Matrices of data 64
7.2 Time dynamics of the relaxation processes 66
7.3 Dependence of transmittivity on the pump fluence 67
7.4 Decay Associated Spectra 69
7.5 Periodic modulations of transmittivity 72
Bibliography 82

Chapter 8: Discussion 83
8.1 Observation of coherent phonons 83
8.2 Electron distribution relaxation dynamics 91
Bibliography 92

Chapter 9: Conclusions 93

Ringraziamenti 96